

STRUCTURE PROPERTY STUDIES IN FERRO-MAGNETIC SHAPE MEMORY Ni-Mn-Ga-X ALLOYS

A THESIS

*Submitted in partial fulfilment of the
requirements for the award of the degree*

of

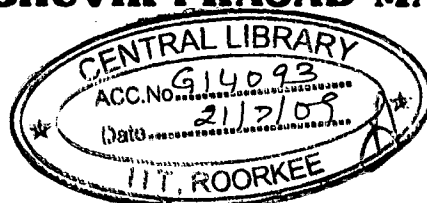
DOCTOR OF PHILOSOPHY

in

METALLURGICAL AND MATERIALS ENGINEERING

by

RAGHUVIR PRASAD MATHUR



DEPARTMENT OF METALLURGICAL AND MATERIALS ENGINEERING

INDIAN INSTITUTE OF TECHNOLOGY ROORKEE

ROORKEE - 247 667 (INDIA)

JULY, 2008

**© INDIAN INSTITUTE OF TECHNOLOGY ROORKEE, ROORKEE, 2008
ALL RIGHTS RESERVED**



INDIAN INSTITUTE OF TECHNOLOGY ROORKEE ROORKEE


CANDIDATE'S DECLARATION


I hereby certify that the work which is being presented in the thesis entitled "**STRUCTURE PROPERTY STUDIES IN FERRO-MAGNETIC SHAPE MEMORY Ni-Mn-Ga-X ALLOYS**" in partial fulfilment of the requirements for the award of the Degree of Doctor of Philosophy and submitted in the Department of Metallurgical and Materials Engineering of the Indian Institute of Technology Roorkee, Roorkee is an authentic record of my own work carried out during a period from July, 2002 to July, 2008 under the supervision of Dr. Subrata Ray, Professor, Department of Metallurgical and Materials Engineering, Indian Institute of Technology Roorkee, Roorkee and Dr. V Chandrasekaran., Scientist & Head, Advanced Magnetics Group, Defence Metallurgical Research Laboratory, Hyderabad.

The matter presented in the thesis has not been submitted by me for the award of any other degree of this or any other Institute.


28/7/08
(RAGHUVIR PRASAD MATHUR)


This is to certify that the above statement made by the candidate is correct to the best of our knowledge.


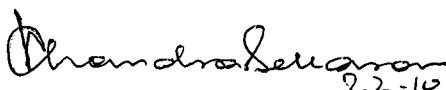

(Dr. V Chandrasekaran)
Supervisor


(Dr. Subrata Ray)
Supervisor

Date: 28/07/08

The Ph.D. Viva-Voce Examination of **Mr. Raghuvir Prasad Mathur**, Research Scholar has been held on 22-X-2008.....


Signature of Supervisors



22-10-08.
Signature of External Examiner

ABSTRACT

Shape Memory alloys based on Fe, Ni, Cu and Ti systems are finding an ever-increasing application in devices due to a large recoverable strain caused by conversion of variants in the martensite phase. Martensitic transformations are typically first order transitions without atom diffusion. Such transformations are influenced by external physical parameters such as temperature; applied uniaxial stress and hydrostatic pressure. In ferromagnetic systems, strains under magnetic fields or *the magnetostriction* due to realignments of magnetic domains is a common phenomenon with small strains usually of the order of $\sim 10^{-6}$. In contrast, magnetic field induced large reversible strain results in recoverable shape changes in some martensite alloys known as Ferro Magnetic Shape Memory (FMSM) alloys. Off-stoichiometric Ni_2MnGa has shown the Magnetic Field Induced Strains (MFIS or λ) going an order of magnitude higher than that observed commonly in magnetostrictive materials. The FMSM alloys have an additional advantage of displaying the phenomenon without contact and with a faster response time over the heating methods applicable to the conventional shape memory alloys.

A range of applications envisaged for the FMSM alloys emerges from their ability to deliver a large MFIS (optimized λ) including those in sensors and actuators in smart devices, force delivery (optimized $E.\lambda$) in retractable missile wings and energy packet (optimized $E.\lambda^2$) for SONAR transducers. These materials may find a place in some of the applications where conventional magnetostrictive materials (e.g. in low frequency higher surveillance range sonar transducers in place of Terfenol-D) or a conventional shape memory alloys (faster response actuators and transducers like retractable wings in place of Nitinol) are employed. Presently the FMSM elements are available commercially and a few demonstration devices have already been made (www.adaptamat.com).

Functional properties of Ferro-Magnetic Shape Memory (FMSM) alloys i.e., a large reversible change in dimensions under a magnetic field, emanates from the reorientation of martensite variants under an external field. Reorientation of the variants requires suitable

ferromagnetic martensite variants with low de-twinning energies to enable movement of boundaries with the forces generated by the magnetic field. Large magnetization, adequate anisotropy and martensite variants with a low de-twinning energy are preliminary requirements for FMSM alloys. In addition, these alloys should possess other engineering properties such as ease of fabrication, ductility, environmental stability etc. While a range of alloys show the FMSM phenomenon, alloys based on Ni₂MnGa compositions have been investigated in literature extensively as Ni-Mn-Ga alloys show large FMSM strains around room temperatures (Ullakko et al, 1996; Kakeshita and Ullakko, 2002). The mechanical properties of the Ni-Mn-Ga alloys is however poor. Improvements in the mechanical properties are attempted through both alloy modification as well as improved processing. The alternate Heusler alloys such as Co-Ni-Al, Ni-Fe-Ga are also being investigated to overcome the limitations of the Ni-Mn-Ga alloys (Wuttig et al, 2000; Oikawa et al, 2001). The process improvements result in microstructural refinements accommodative of stresses generated during the FMSM phenomenon (Li et al, 2004). The alloy development includes modifications within the Heusler phase or generation of beneficial secondary phases, thereby necessitating multi-component alloy systems with different components providing one or more beneficial aspects to the basic alloy system.

The X₂YZ type Heusler alloys consists of the transition element X and Y, and also, trivalent element Z with majority of atomic magnetization concentrated at Y atom positions and a very little contribution reported from other atoms. The present study aims at modification of Heusler alloys by addition of quaternary element-M by preparing Ni-Mn-Ga-M alloys and investigating their structural and magnetic behaviour. Existing reports indicate that Ni₅₀Mn₃₀Ga₂₀ is the optimal composition of the Heusler alloy maximizing the ferromagnetic martensite transformation temperature and so, this composition was chosen as the base composition for modification. The quaternary additions from the following groups were investigated:

- I. Transition element
- II. Trivalent element
- III. Other elements different from those of group I and II

The transition elements in **group I** like Fe and Co, which are in between Ni and Mn, have been selected. Substitutions for either Ni or Mn have been intended. Group-II and Group-III additions are elements substituting for Ga. The addition of trivalent elements like Al and B from **group II** has been tried. B-atoms were expected to go into interstices and change the behaviour of the parent Heusler alloy completely. B-additions were therefore made along with Al addition and alloys with B-additions were 5 component alloys. The additions outside groups I and II are categorized as **Group III** additions and the elements added may have low solubility in the L₂₁ phase, generating thereby grain boundary phases, in order to improve the mechanical properties.

Chapter-1 contains the introductory remarks about the role of the ferromagnetic shape memory alloys in the present generation of smart devices and their potential in the context of engineering applications.

Chapter-2 describes the available literatures on the basics of the characterization and the terminology along with the FMSM alloy system with special emphasis on the primary system viz. Ni-Mn-Ga alloys. Finally, the gap in current status of knowledge about FMSM alloys have been identified and the problem under investigation has been formulated.

Chapter-3 presents the experimental techniques and procedures employed for preparation and characterization of the alloys. The preparation technique includes the alloy melting of and subsequent heat treatment of the bulk alloys. The rapid quenching method adopted for select alloy compositions is also elucidated. The chapter also highlights various characterization techniques and specimen preparations and methods for data analysis relevant to this study.

As stated earlier, a base composition Ni₅₀Mn₃₀Ga₂₀ (atom %) was chosen and accordingly quaternary alloys with replacement for the specific elements were prepared by repeated vacuum arc melting of high purity constituent elements. The alloys melted were homogenized for different durations by vacuum heat-treatment. The alloys thus homogenized were characterized as bulk Alloys. As the alloys with boron are normally easy glass formers,

alloys with trivalent additions of Al and/or B additions were processed through rapid quenching route additionally to see the effect of processing technique.

The alloys thus prepared were characterized for their chemical composition, structure and microstructure and were evaluated for chemical, magnetic and thermal properties. Alloy chemistry was analyzed by chemical method as well as energy dispersive and wave length dispersive analysis facilities available with electron microscope. Diffraction pattern using X ray diffractometer for bulk alloys and electron diffraction for ribbon specimens were used for determining crystal structure. Optical and electron microscopy were employed for microstructure characterizations. The differential scanning calorimetry measurements gave the transformation temperatures. Magnetic hysteresis loops were recorded at room temperature using vibrating sample magnetometer. In addition, thermo-magnetic measurements were also made on VSM wherein magnetizations under a constant magnetic field at different temperatures were recorded to complement the transformation temperatures through thermal techniques. Alloys with Fe –additions were analyzed through Mössbauer spectroscopy to understand the site occupancy of Fe atoms. The measurements so made were correlated to arrive at a coherent knowledge base.

Chapter–4 presents the results of studies with the intention to substitute Ni/Mn atoms in Ni₅₀Mn₃₀Ga₂₀ alloy by Group-I additions. Alloys with compositions Ni₄₀M₁₀Mn₃₀Ga₂₀ (transition element M=Fe or Co) with intended substitutions of 10 at% M at Ni sites were prepared by vacuum arc melting and heat-treated at 1273K for 3 hrs and gas quenched in order to investigate the effect of addition of Fe and Co. The as-cast alloys contained small amount of secondary phases. While alloy Ni₄₀Co₁₀Mn₃₀Ga₂₀ showed single-phase structure after heat-treatment, the alloy Ni₄₀Fe₁₀Mn₃₀Ga₂₀ showed the presence of traces of a secondary phase in x ray diffraction studies. The microstructural studies however showed signs of the ploughing out the secondary phase during specimen polishing. The diffraction patterns revealed a cubic L2₁ (Heusler) structure at room temperature for the alloy Ni₄₀Fe₁₀Mn₃₀Ga₂₀ and a modulated martensite (5M) structure for the alloy Ni₄₀Co₁₀Mn₃₀Ga₂₀ after heat-treatment. The obtained phase structures were consistent with the martensite transformation temperatures evaluated for the alloys through two independent techniques of thermal analysis

by differential scanning calorimetry (DSC) and thermo-magnetic measurements on a vibrating sample magnetometer (VSM). The room temperature saturation magnetization improved with addition of ferromagnetic elements Fe or Co respectively over the reported values for ternary base composition. In view of the $L2_1$ structure of Fe containing alloy and the martensite, a one-to-one correlation was difficult. The lowering of martensite transformation temperatures may be explained due to a reduction in electron to atom ratio with Fe/Co additions. The Mössbauer spectrum of the Fe containing alloy indicated the presence of Fe atoms at paramagnetic as well as ferromagnetic sites. In combination with the magnetic measurements, the ferromagnetic spectrum could be explained with Fe atoms placed at Mn sites.

Based on the studies conducted on $Ni_{40}M_{10}Mn_{30}Ga_{20}$ ($M=Fe/Co$), a systematic study for the effect of varying amounts of Fe with intended substitutions for Ni or Mn were undertaken. Series of alloy compositions $Ni_{50}Fe_xMn_{30-x}Ga_{20}$ ($x=2.5, 5$ and 15) and $Ni_{45}Fe_5Mn_{30}Ga_{20}$ were prepared. The heat-treated $Ni_{40}Fe_{10}Mn_{30}Ga_{20}$ has indicated the presence of a trace secondary phase, thereby suggesting that the heat-treatment temperature of 1273 K is in two-phase field. The heat treatment was therefore modified to a two stage heat-treatment i.e. 1273 K for 72h and 1073K for 48h followed by water quenching. The alloys with low Fe content of 2.5 and 5 at% were single-phase martensite structure whereas alloy with 15 at% Fe showed cubic $L2_1$ austenite with about 10 at% Fe along with a second phase depleted in Mn and Ga. The two-phase structure showed that the limit of solubility of Fe in the base $L2_1$ structure is below 15 at% Fe. The room temperature magnetization increased with increasing Fe and the measurements at 173K for the martensite phase for all the compositions indicated the saturation magnetization to follow no specific pattern with Fe. The martensite transformation temperatures measured by DSC and VSM techniques did not follow a consistently increasing or decreasing trend with increasing Fe. The Mössbauer spectrum of the alloys showed the two ferromagnetic sub-spectra for the single phase alloy $Ni_{45}Fe_5Mn_{30}Ga_{20}$. These measurements indicated that Fe went to Ga sites initially and at higher Fe contents but at intermediate level of addition, it went to Mn and then to Ni sites. The Fe atoms are thus located in different chemical environment at different substitution levels.

Chapter-5 presents the studies carried out with Group II and III additions substituting for Ga in Ni₅₀Mn₃₀Ga₂₀ alloy. For the Group-II additions, the initial investigations with Ni₅₀Mn₃₀Ga₁₅Al₅ alloys showed that the martensite transformation may have modified to two stage sequence with Al additions. Moreover the martensite transformation temperatures were lowered with the Al addition even though the average electron to atom ratio, a key parameter to the stability of the martensite is unchanged. Additions of smaller sized atom B were contemplated for compact structures. Envisaging a large replacement of the largest atom Ga with small B atoms may form interstitial alloy rather than substitutional alloys, compositions Ni₅₀Mn₃₀Ga₁₅Al₄B₁ and Ni₅₀Mn₃₀Ga₁₅Al₁B₄ have been prepared and investigated. The addition of B did not change the phase structure, but the magnetizations were drastically reduced even at 1 at% B. The grain sizes were refined as revealed by the peak broadening of the x-ray diffractograms. With B and Al as possible glass formers, alternative technique of rapid quenching using melt spinning was tried to understand the effects of the addition on the processing aspects. The melt spun alloys showed a direct formation of beneficial 7M martensite phase along with varied amount of the amorphous phases of different compositions. The martensite obtained was very fine and the sub martensite structure showing the orientation relationship was also seen.

For Group-III additions, many additives have been reported earlier, however one of the main aims of this study was to understand the effect of modifications in Heusler structure with the additions rather than obtaining secondary phases modifying other functional properties. The rare earth additions were selected as these additions are known to improve the magnetic properties especially in rare earth- transition element permanent magnets through 3d-4f electronic interactions if present in the Heusler structure. 1 at% addition of a light rare earth element Sm and heavy rare earth element Dy for substituting the largest atom of Ga have been selected. Ni₅₀Mn₃₀Ga₁₉Dy₁ and Ni₅₀Mn₃₀Ga₁₉Sm₁ accordingly were prepared and heat-treated at 1273 K for 72h and 1073K for 48h followed by water quenching. EPMA studies of both the alloys showed the matrix phase with rare earth elements below detectable limits, which were detected only in second phase. The change in martensite temperatures and the work hardening behaviour during mechanical testing, however; have indicated the

possibility of small amount of the rare earths in the matrix phase. Magnetization of the alloys lowered with additions in line with lower phase fraction of the matrix phase. The Curie temperature of the alloys lowered and the martensite transformation showed an increase. The modified matrix compositions due to formation of the second phase, showed an increased Mn/Ga ratio over the bulk composition. The studies with the group III elements has shown that these additions though partitioning mainly to second phase, may be retained in very small levels to modify the structure and properties of the $L2_1$ / related martensite phases. Both the transformation temperatures as well as specific magnetization were lower for the heavy rare earth Sm additions. The beneficial effects of the rare earth additions may therefore be through modifications of the secondary functional properties such as ductility, mechanical strength etc. through modified $L2_1$ / martensite phases as well as the secondary phases. These additions may be useful in the wider context involving the other functional aspects.

Chapter 6 outlines the broad conclusions of the present investigation and the emerging trends for future studies.

ACKNOWLEDGEMENTS

At the outset, I am grateful to god to bestow me with knowledgeable and compassionate teachers all through my life; first as my parents and then at various stages of studies. This academic program has been a good learning experience wherein I was taught to look at the problem and results in unconventional ways. I am pleased to express my deep sense of gratitude for Professor Subrata Ray and Dr V Chandrasekaran for their invaluable guidance, constructive criticism, thought provoking discussions and painstaking efforts throughout the course of this work and the experience I enjoyed working with them

My sincere thanks are due to Dr D Banerjee, Dr AM Sriramamurthy and Dr G Malakondaiah, Directors of DMRL for their constant encouragement at all the times. I am specifically grateful to Dr Sreeramamurthy for introducing and expressing his faith in me by entrusting this assignment to me. Encouragement in one or the other way by elders is required at all walks of life. My thanks are due to Mr TSRK Sastry, Mr MS Chordia and Dr D Akhtar for their encouraging words.

The program would not have come to end without the support of friends and well wishers. I am thankful to my team members Shri Ranjan Singh, Dr Manivel Raja, Dr Partha Ghosal and staff of Advanced Magnetics, Analytical Chemistry and Structural Characterization Groups at DMRL, Hyderabad. I am thankful to Dr Sandeep Bansal, Shri Kuldeep Rana, Dr Rajnesh Tyagi, Mr. Narendra Kumar at IIT Roorkee for all their support. Dr Ujjwal Prakash and Mrs. Seema Prakash has been a moral support both at Hyderabad and at Roorkee. My special thanks to Shri Ranjan Singh and Dr Sameer Kamat for theirs all out discussions and support during the thesis preparation.

“You can do it” was my phrase given to my daughters Garima and Anima.. I am thankful to them for returning the same to me at appropriate times. This work would not have come to an end without adjustments on their and their mother’s part. This thesis belongs to them.

RAGHUVIR PRASAD MATHUR

CONTENTS

	Page No.
CANDIDATE'S DECLARATION	
ABSTRACT	i
ACKNOWLEDGEMENTS	viii
CONTENTS	ix
LIST OF FIGURES	xii
LIST OF TABLES	xix
<i>Chapter 1</i>	1
1. INTRODUCTION	1
<i>Chapter 2</i>	7
2. LITERATURE REVIEW	7
2.1 Introduction	7
2.2 behaviour of materials under external magnetic fields	7
2.3 Ferro-Magnetic Shape Memory Effect: Evolution and the alloy systems	12
2.4 Metallurgy of Ni-Mn-Ga alloys	19
2.4.1 Equilibrium phase transformation	19
<i>Structural transformations</i>	19
<i>Magnetic transition</i>	25
2.4.2 Martensite transformation, variants and structures	26
2.5 Quaternary additions	33
2.6 Effect of processing parameters	36
2.7 Formulation of the Problem	38
<i>Chapter 3</i>	42
3. EXPERIMENTAL METHODS	42
3.1 Alloy Preparation	42
3.1.1 Selection of raw materials and alloy compositions	42
3.1.2 Alloy melting	43

3.1.3	Alloy homogenization and bulk alloy preparation	45
3.1.4	Rapid quenching	45
3.2	Compositional analysis	46
3.3	Structural characterization	47
3.3.1	X-ray diffraction	48
3.3.2	Optical microscopy	49
3.3.3	Scanning electron microscopy	50
3.3.4	Transmission electron microscopy	52
3.3.5	Mössbauer spectroscopy	54
3.4	Magnetic Characterization	56
3.5	Thermal Characterization	58
3.6	Mechanical Property Characterization	60
 <i>Chapter 4</i>		61
4.	RESULTS AND DISCUSSION: ALLOYS WITH TRANSITION ELEMENT REPLACEMENTS	61
4.1	Results of Studies with the base alloy composition $Ni_{50}Mn_{30}Ga_{20}$	61
4.1.1	Chemical composition of alloy	61
4.1.2	Structural characterization of the alloy	62
4.1.3	Transformation characteristics	64
4.1.4	Room temperature magnetization behavior	65
4.2	Results of studies with the intention to replace Ni by Fe/Co in $Ni_{50}Mn_{30}Ga_{20}$	66
4.2.1	Chemical composition of alloys	66
4.2.2	Structural characterization of the alloy	67
4.2.3	Transformation characteristics	72
4.2.4	Room temperature magnetization behavior	74
4.3.	Results of Studies with the intention to replace Mn by Fe in $Ni_{50}Mn_{30}Ga_{20}$	75
4.3.1	Chemical composition of alloys	75

4.3.2	Structural characterization of the alloy	76
4.3.3	Transformation characteristics	81
4.3.4	Room temperature magnetization behavior	84
4.4	Discussions	85
 <i>Chapter 5</i>		99
5.RESULTS AND DISCUSSION: ALLOYS WITH ADDITIONS		99
INTENDED For Ga		
5.1	Results of studies for $\text{Ni}_{50}\text{Mn}_{30}\text{Ga}_{15}\text{Al}_{5-x}\text{B}_x$	99
	alloys with intended replacement for Ga by Al/B	
5.1.1	Chemical composition of alloys	99
5.1.2	Structural characterization of the alloy	100
5.1.3	Transformation characteristics	104
5.1.4	Room temperature magnetization behavior	105
5.2	Results of studies for metastable $\text{Ni}_{50}\text{Mn}_{30}\text{Ga}_{15}\text{Al}_{5-x}\text{B}_x$ alloys	106
5.2.1	Structural characterization of the alloy	106
5.2.2	Transformation characteristics	112
5.2.3	Room temperature magnetization behavior	114
5.3	Results of studies for rare earth substitutions	
	intended for Ga	114
5.3.1	Chemical composition of alloys	114
5.3.2	Structural characterization of the alloy	115
5.3.3	Transformation characteristics	117
5.3.4	Room temperature magnetization behavior	119
5.3.5	Room temperature mechanical behavior	119
5.4	Discussions	120
 <i>Chapter 6</i>		130
6. CONCLUSIONS		130
 REFERENCES		135

LIST OF FIGURES

Figure No.	Figure Caption	Page No.
Fig. 1.1	Positioning of various actuator technologies. The magnetic shape memory bridges the gap between ‘smart’ and conventional actuator technologies. (Wilson et al 2007))	3
Fig. 1.2	Typical applications of FMSM alloys in different walks of life	3
Fig. 1.3	Growth in number of publications on FMSM alloys (Chernenko 2007)	5
Fig. 2.1	Typical hysteresis curves for a magnetic material (a) $M - H$ loop (b) $B - H$ loop. The shaded rectangle in the second quadrant of $B - H$ curve represents the energy product, $(BH)_{max}$. The two plots are related by the equation $B = H + 4\pi M$ (CGS).	9
Fig. 2.2	Schematic reorientation of magnetic moments giving Magnetostriction phenomenon	11
Fig. 2.3	λ -H Curves (Butterfly curves) obtained for a typical magnetostrictive material (Terfenol-D) measured at different compressive stress level	12
Fig. 2.4	Schematic illustration of martensite transformation and twinning in two dimensions.	14
Fig. 2.5	Schematic magnetic moments in the twinned martensite (a) Magnetic moments without magnetic field and (b) Redistribution of variants in magnetic field.	15
Fig. 2.6	Schematic of growth of preferentially oriented variant in magnetic field and corresponding change in crystal orientation resulting in large deformation (Tellinen et al 2002).	16
Fig. 2.7	Atomic structure of ordered X_2YZ type alloys derived from BCC structure a) $B2'$ structure with equivalent sites for Y and Z and b) $L2_1$ structure.	19
Fig. 2.8	Binary phase diagrams of Mn-Ni and Ni-Ga.	20

- Fig. 2.9** Schematic phase diagram of the cubic ferromagnet in the (a; b) plane. The solid curves represent phase transitions; the dashed curves are stability boundaries. Dashed and solid lines approaching each other mark a second-order phase transition. (Zayak et al 2002) 21
- Fig. 2.10** The phase diagram of the ferromagnet $\text{Ni}_{2+x}\text{Mn}_{1-x}\text{Ga}$ in the (T;x) plane. The dotted line represents a first-order phase transition; dash-dotted lines are stability area boundaries; solid lines represent phase transitions of second-order. The phases are labeled as P: paramagnetic state, C: cubic lattice, F: ferromagnetic state and T: tetragonal lattice (Zayak et al 2002). 21
- Fig. 2.11** Full (T;x) phase diagram of $\text{Ni}_{2+x}\text{Mn}_{1-x}\text{Ga}$ showing the region of TC and TM intersection. The dotted line corresponds to 1st-order phase transitions; dashed and dash-dotted lines mark the stability boundaries; the solid line represents phase transitions of second order (Zayak et al 2002).. 22
- Fig. 2.12** Isothermal section of ternary Ni-Mn-Ga phase diagram at 800 °C (Chen et al 2004). 22
- Fig. 2.13** Quasi-binary temperature-composition diagram showing experimental transition (Overholser and Wuttig 1999). 24
- Fig. 2.14** DTA cooling scans showing Liquid \rightarrow B2' & B2' \rightarrow L2₁ transitions in Ni₅₀Mn_{25+x}Ga_{25-x} alloys for x= (a) -5 , (b) 0 and (c) 5 (Overholser and Wuttig 1999).. 24
- Fig. 2.15** Contour view of curve fitted Curie temperature T_C (K) with experimental data (Jin et al 2002). 25
- Fig. 2.16** Atomic arrangement and correlaton of the different crystal structures for Ni-Mn-Ga alloys (a) Cubic L2₁ , (b) tetragonal martensite, (c) and (d) the 5 and 7 layered martensite 5M and 7M structures respectively (Brown et al 2002) 27
- Fig. 2.17** Displacements parallel to the a_{ortho} of the atoms in successive (010)_{ortho} for (a) 5M and (b) 7M modulations (Brown et al 2002) 27
- Fig. 2.18** X-ray-diffraction patterns of the as-ground powder sample with $D, 50$ mm a) before annealing and b) after annealing at 500 °C for 10 h at various temperatures (Wang et al 2002) . 28

Fig. 2.19	The room temperature martensite variants as a function of electron to atom ratios in Ni-Mn-Ga alloys. 5M, 7M and T denote the modulated 5M, 7M or non-modulated tetragonal martensite structures respectively (based on data by Soderberg 2004)	30
Fig. 2.20	Saturation magnetization M_s V/s the average number of valence electrons per atom (e/a) shows a peak nearly at 7.5, the value of e/a for the stoichiometric composition Ni_2MnGa . • and + are calculated and experimental M_s for the same composition, respectively (Murray et al 1998).	31
Fig. 2.21	Dependence of martensite transformation temperature on e/a ratio for Fe/Co substituted Ni-Mn-Ga alloys (Khovailo et al 2003)	34
Fig. 2.22	Room temperature Mössbauer spectra of a) $Ni_{2-x}Fe_xMnGa$ and b) $Ni_2Mn_{1-x}Fe_xGa$ (Mitros et al 1987).	35
Fig. 2.23	Microstructures of the polycrystalline $Ni_{54}Mn_{25}Ga_{21}$ alloys (a)optical micrograph for the button sample,(b)optical micrograph,(c)TEM bright field image and (d)the SAED pattern for the rod sample at 20 °C (Li et al 2004)	37
Fig. 2.24	Compressive stress strain curves of the polycrystalline $Ni_{54}Mn_{25}Ga_{21}$ for (a) button and (b) rod samples (Li et al 2004).	37
Fig. 2.25	The basic ingredient of the Ni-Mn-Ga alloys and quaternary addition elements planned for the study	40
Fig. 3.1	The Vacuum Arc Melting furnace	44
Fig. 3.2	The vacuum melt spinning unit and the experimental set up inside.	46
Fig. 3.3	Schematic layout of the x ray diffraction techniques	48
Fig. 3.4	The Scanning Electron Microscope	50
Fig. 3.5	Transmission Electron Microscope and the specimen preparation Precision Ion Polishing System (PIPS)	53
Fig. 3.6	Constant acceleration spectrometer; top: arrangement showing fixed specimen holder and velocity modulator for the ^{57}Fe source and bottom: data logging system	56
Fig. 3.7	The Vibrating Sample Magnetometer	58
Fig. 3.8	The Modulated Differential Scanning Calorimeter along with liquid nitrogen pumping system at left	59

Fig. 4.1	The x-ray diffractogram for the base alloy NMG	62
Fig. 4.2	The calculated x-ray diffractograms for different structures of Ni_2MnGa based on the reported values by Brown et al 2002	63
Fig. 4.3	The DSC thermogram for the heat treated alloy NMG	64
Fig. 4.4	The M-T thermo-magnetic measurements for the heat treated alloy NMG	65
Fig. 4.5	The room temperature magnetization M-H curve for the heat treated alloy NMG	66
Fig. 4.6	X-ray Diffractograms($\text{Cu K}\alpha$) at a scan rate of $1^\circ(2\theta)/\text{min}$ for (a) as-cast and (b) heat-treated quaternary alloys. The identified reflections are marked for cubic austenite phase for alloy $\text{Ni}_{40}\text{Fe}_{10}$ and 5M martensite phase for alloy $\text{Ni}_{40}\text{Co}_{10}$. The un-indexed secondary phase reflections are marked with *	68
Fig. 4.7	Back Scattered Electron Images of as-cast a) $\text{Ni}_{40}\text{Fe}_{10}$ alloy and b) $\text{Ni}_{40}\text{Co}_{10}$ alloy	70
Fig. 4.8	Back Scattered Electron Images of heat treated a) $\text{Ni}_{40}\text{Fe}_{10}$ alloy and b) $\text{Ni}_{40}\text{Co}_{10}$ alloy	70
Fig. 4.9	Electron Probe Microanalysis (EPMA) for annealed alloy $\text{Ni}_{40}\text{Fe}_{10}$ along the arrow in Fig 4.3a.	71
Fig. 4.10	Mössbauer Spectrum of heat-treated $\text{Ni}_{40}\text{Fe}_{10}$ alloy at room temperature	71
Fig. 4.11	DSC thermograms for the heat treated alloys $\text{Ni}_{40}\text{Fe}_{10}$ and $\text{Ni}_{40}\text{Co}_{10}$	72
Fig. 4.12	The magnetization- temperatures curves of a) alloys $\text{Ni}_{40}\text{Fe}_{10}$ and b) $\text{Ni}_{40}\text{Co}_{10}$ in as cast as well as heat treated conditions	74
Fig. 4.13	Room temperature magnetization curves of a) alloys $\text{Ni}_{40}\text{Fe}_{10}$ and b) $\text{Ni}_{40}\text{Co}_{10}$ in as cast and heat treated conditions.	74
Fig. 4.14	X-ray Diffractograms ($\text{Cu K}\alpha$) taken at (a) a scan rate of $1^\circ(2\theta)/\text{min}$ and (b) a scan rate of $0.5^\circ(2\theta)/\text{min}$ for the alloys $\text{Mn}_{27.5}\text{Fe}_{2.5}$, $\text{Mn}_{25}\text{Fe}_5$, $\text{Mn}_{15}\text{Fe}_{15}$ and $\text{Ni}_{45}\text{Fe}_5$. The phases identified (M-martensite and A-austenite) are marked with their reflections. The secondary phase in alloy $\text{Mn}_{15}\text{Fe}_{15}$ is marked with *. The • for alloy $\text{Mn}_{27.5}\text{Fe}_{2.5}$ shows the reflections disappearing on random placement of Fe in other compositions in the series of alloys	77

Fig. 4.15	Back Scattered Electron Images of a) alloy Mn _{27.5} Fe _{2.5} , b) alloy Mn ₂₅ Fe ₅ , c) alloy Mn ₁₅ Fe ₁₅ and d) alloy Ni ₄₅ Fe ₅	79
Fig. 4.16	Mössbauer Spectrum of the alloys Mn _{27.5} Fe _{2.5} , Mn ₂₅ Fe ₅ , Mn ₁₅ Fe ₁₅ and Ni ₄₅ Fe ₅ taken at room temperature. The solid line indicates the fitting curve with parameters shown in Table 4.8.	80
Fig. 4.17	DSC thermograms for the alloys Mn _{27.5} Fe _{2.5} , Mn ₂₅ Fe ₅ , Mn ₁₅ Fe ₁₅ and Ni ₄₅ Fe ₅	82
Fig. 4.18	Thermo-magnetic measurements for the alloys Mn _{27.5} Fe _{2.5} , Mn ₂₅ Fe ₅ , Mn ₁₅ Fe ₁₅ and Ni ₄₅ Fe ₅ .	83
Fig. 4.19	The magnetization curves of the alloys Mn _{27.5} Fe _{2.5} , Mn ₂₅ Fe ₅ , Mn ₁₅ Fe ₁₅ and Ni ₄₅ Fe ₅ at a) room temperature and b) at 100K	84
Fig. 4.20	Variation of lattice parameters of Fe containing alloys (a) with respect to electron to atom ratio and (b) with respect to atom %Fe	91
Fig. 4.21	Variation of transformation temperatures T_0 and T_c for Fe containing alloys (a) with respect to electron to atom ratio and (b) with respect to atom %Fe. The T_c values at higher Fe-levels are for two-phase alloys and indicate higher of the two T_c 's	92
Fig. 4.22	The saturation magnetization of Fe containing alloy at RT and 173K	96
Fig. 5.1	Backscattered electron image of (a) as-cast and (b) heat-treated Ga ₁₅ Al ₅ , along with EPMA analysis for constituent elements for heat-treated alloys (along the arrow), showing uniform distribution of elements.	101
Fig. 5.2	The x-ray diffractograms of the as cast and heat-treated Ga ₁₅ Al ₅ alloy	101
Fig. 5.3	The BSE images for the alloys Ga ₁₅ Al ₄ B ₁ and Ga ₁₅ Al ₁ B ₄	102
Fig. 5.4	The X-ray diffractograms of the heat-treated Ga ₁₅ Al ₄ B ₁ and Ga ₁₅ Al ₁ B ₄ alloys	103
Fig. 5.5	The DSC thermograms for the Ga ₁₅ Al ₅ , Ga ₁₅ Al ₄ B ₁ and Ga ₁₅ Al ₁ B ₄ alloys	104
Fig. 5.6	The thermo-magnetic M-T curves for Ga ₁₅ Al ₅ , Ga ₁₅ Al ₄ B ₁ and Ga ₁₅ Al ₁ B ₄ alloys	105
Fig. 5.7	Room temperature magnetization curves for the Ga ₁₅ Al ₅ , Ga ₁₅ Al ₄ B ₁ and Ga ₁₅ Al ₁ B ₄ alloys	106

Fig. 5.8	The x-ray diffractograms of the melt spun ribbons of Ga ₁₅ Al ₅ , Ga ₁₅ Al ₄ B ₁ and Ga ₁₅ Al ₁ B ₄ alloys	106
Fig. 5.9	(a) The TEM picture of alloy Ga ₁₅ Al ₅ showing martensite plates along with other phase and (b) SAD pattern from the area circled in (a) showing the diffused ring pattern of amorphous or a nanocrystalline phase.	107
Fig. 5.10	(a) The TEM BF image and (b) corresponding SADP for Ga ₁₅ Al ₅ alloy showing the 7M martensite phase	108
Fig. 5.11	The internal twinning within primary martensite plates (tv ₂₀) in Ga ₁₅ Al ₅ alloy	109
Fig. 5.12	(a) The TEM micrograph of Ga ₁₅ Al ₄ B ₁ alloy, (b) the SADP for the structure and (c) dark field image from the (220) reflection	109
Fig. 5.13	(a) The TEM microstructure of the twinned martensite in alloy GaAl ₄ B ₁ and (b) the corresponding SADP indexed with 7M martensite structure	110
Fig. 5.14	(a) TEM image of Ga ₁₅ Al ₁ B ₄ showing cellular structure with bright spots indicative of fall of non-adherent particles. (b) enlarged cells from some area from (a) showing plates within the cell	111
Fig. 5.15	TEM image showing typical microstructural features of (a) the internal twin structure and (b) multiple twin variants noticed in Ga ₁₅ Al ₁ B ₄ alloy ribbons	111
Fig. 5.16	DSC thermograms of the melt spun Ga ₁₅ Al ₅ , Ga ₁₅ Al ₄ B ₁ and Ga ₁₅ Al ₁ B ₄ alloy ribbons	112
Fig. 5.17	Thermo-magnetic M-T measurements for the melt spun alloys Ga ₁₅ Al ₅ , Ga ₁₅ Al ₄ B ₁ and Ga ₁₅ Al ₁ B ₄	113
Fig. 5.18	Room temperature M-H measurements of the melt spun ribbons. The inset shows an enlarged view around origin	114
Fig. 5.19	Back scattered electron images for a) Ga ₁₉ Sm ₁ and b) Ga ₁₉ Dy ₁ alloys	115
Fig. 5.20	X ray diffractograms (Cu K _α) of Ni ₅₀ Mn ₃₀ Ga ₂₀ , Ni ₅₀ Mn ₃₀ Ga ₁₉ Sm ₁ and Ni ₅₀ Mn ₃₀ Ga ₁₉ Dy ₁	116
Fig. 5.21	The DSC thermograms for the alloys Ga ₁₉ Sm ₁ , Ga ₁₉ Dy ₁ and the alloy NMG	117

Fig. 5.22	The thermo-magnetic M-T plots for the alloys Ga19Sm1, Ga19Dy1 and the alloy NMG	118
Fig. 5.23	Room temperature hysteresis curves for the alloys Ga19Sm1, Ga19Dy1 and the alloy NMG. The inset shows the area around origin	119
Fig. 5.24	Room temperature compression test results for the alloys Ga19Sm1, Ga19Dy1 and the alloy NMG.	119
Fig. 5.25	Variation of the structural and magnetic transformation temperatures with boron content in A/B substituted heat treated alloys (HT) as well as melt spun ribbons (Ribbons)	125
Fig. 5.26	Magnetization changes with boron content in A/B substituted heat treated alloys (HT) as well as melt spun ribbons (Ribbons)	126

LIST OF TABLES

Table No.	Title	Page No.
Table 2.1	Comparison of some FMSM alloys (Kakeshita and Ullakko 2002).	14
Table 2.2	Heusler Alloys with electron/atom ratio in the range where FMSM may be found. (Wuttig et al 2000)	18
Table 2.3	Atomic positions for the Ni ₂ MnGa refined in space group Pnnm based on neutron diffraction patterns at different temperatures (Brown et al 2002)	26
Table 2.4	Atomic positions (x,y, z), ADP (U_{iso}), site occupancy factors (s.o.f.) and amplitudes (A_i) of the modulation function of the modulated structure of Ni ₂ Mn _{1.15} Ga _{0.85} martensite (Righi et al 2007)	29
Table 3.1	Nominal compositions of the alloys prepared for the present study	44
Table 4.1	Nominal and analyzed compositions of the base alloy composition NMG	61
Table 4.2	The peak positions, d-spacing and the corresponding atomic plane of the tetragonal martensite phase for the diffractogram of alloy NMG	63
Table 4.3	Nominal and analyzed compositions of the Ni40Fe10 and Ni40Co10 alloys	67
Table 4.4	The assignment of the x-ray diffractogram peaks for the Cast and heat-treated Ni40Fe10 and Ni40Co10 alloys to various phases.	69
Table 4.5	Transformation temperatures through DSC for the alloys investigated	73
Table 4.6	Nominal and Analyzed Compositions of the arc-melted Ni-Fe-Mn-Ga alloys	75
Table 4.7	The assignment of the x-ray diffractogram peaks for heat-treated Mn27.5Fe2.5, Mn25Fe5, Mn15Fe15 and Ni45Fe5 alloys to various phases	78
Table 4.8	Mössbauer parameters Hyperfine magnetic field (H_{hf}), quadrupole splitting (Q.S.), Isomer shift (I.S) and relative intensities for the ⁵⁷ Fe Mössbauer spectra in Ni-Fe-Mn-Ga alloys	81

Table 4.9	Transformation temperatures and enthalpies of transformation for the alloys Mn _{27.5} Fe _{2.5} , Mn ₂₅ Fe ₅ , Mn ₁₅ Fe ₁₅ and Ni ₄₅ Fe ₅	83
Table 4.10	Room temperature phase structure, lattice parameters and the electron to atom ratios of heat treated alloys	87
Table 5.1	Nominal and analyzed compositions of the heat-treated Ni-Mn-Ga-Al-B alloys	100
Table 5.2	The assignment of the x-ray diffractogram peaks for heat-treated Ga ₁₅ Al ₅ , Ga ₁₅ Al ₄ B ₁ and Ga ₁₅ Al ₁ B ₄ alloys to various phases	103
Table 5.3	Transformation temperatures through DSC for the Ga ₁₅ Al ₅ , Ga ₁₅ Al ₄ B ₁ and Ga ₁₅ Al ₁ B ₄ alloys	104
Table 5.4	The x-ray peak reflections and their assignments to various planes for the melt spun ribbons of Ga ₁₅ Al ₅ , Ga ₁₅ Al ₄ B ₁ and Ga ₁₅ Al ₁ B ₄ alloys	107
Table 5.5	Transformation temperatures through DSC for the Ga ₁₅ Al ₅ , Ga ₁₅ Al ₄ B ₁ and Ga ₁₅ Al ₁ B ₄ alloy ribbons	112
Table 5.6	Nominal and analyzed compositions of the Ni ₄₀ Fe ₁₀ and Ni ₄₀ Co ₁₀ alloys	114
Table 5.7	Analyzed average compositions in atom % for the matrix and the second phase in Ga ₁₉ Sm ₁ and Ga ₁₉ Dy ₁ alloys	115
Table 5.8	The assignment of the x-ray diffractogram peaks for heat-treated Ga ₁₉ Sm ₁ and Ga ₁₉ Dy ₁ alloys. The values for NMG alloy is added for comparison	116
Table 5.9	Transformation temperatures for the alloys Ga ₁₉ Sm ₁ and Ga ₁₉ Dy ₁ through DSC	117
Table 5.10	Mechanical properties of the alloys Ga ₁₉ Sm ₁ , Ga ₁₉ Dy ₁ and the alloy NMG	120
Table 5.11	Martensite phase and lattice parameters for the alloys Ga ₁₅ Al ₅ , Ga ₁₅ Al ₄ B ₁ and Ga ₁₅ Al ₁ B ₄ alloys after heat-treatment as well as on rapid solidification	122
Table 5.12	Martensite phase and lattice parameters for the alloys Ga ₁₉ Sm ₁ and Ga ₁₉ Dy ₁ alloys	127

Smart devices which can *sense and act* are finding increasing applications in today's technological world. The word "smart" here signifies self adaptability, self sensing and multiple functionalities of the materials. Materials for smart devices are required to possess a faster and larger mechanical response to an external impetus in order to meet the requirements of miniaturization, time and compatibility of the micro-electronic and micro-mechanical components of the Micro-Electro-Mechanical System (MEMS) devices. Different types of materials are today available responding to physical external stimuli ranging from temperature to electrical or magnetic field. Materials such as Shape memory Alloys (SMA) change their shape reversibly on application of heat where as electrostrictive materials (e.g. lead zirconate titanate PZT), Electro-Active polymers (EAPs e.g. Poly - vinylidene Fluoride PVDF), Electro-Rheological fluids (ER fluids) etc respond to electric fields. Magnetostrictive materials (such as Terfenol-D), Magneto-Rheological fluids (MR fluids) and Ferro-Magnetic Shape Memory (FMSM) alloys on the other hand change their shape reversibly under magnetic fields and are employed in applications as smart materials. Each class of materials has its own advantage over others. The smart materials and their engineering requirements have been extensively reviewed in literature (Wilson et al 2007). Fig 1.1 shows functional property map of various materials currently employed. The conventional devices based on pneumatics, hydraulics or the shape memory materials have lower operating frequencies with a high work output. The smart devices based on electrostrictive, piezo-electric or magnetic shape memory materials usually overcome the disadvantage of low frequency with a faster response times at the cost of work outputs. Magnetic Shape Memory (MSM) alloys bridge the gap between the two extremes and combines high work output with reasonably high frequency. MSMs are therefore employed increasingly in today's devices as smart materials. The smart materials, in addition, are required to have multi-functionality i.e. ability to perform different functions such as sensors as well as actuators. The magnetic shape memory alloys meet this requirement also effectively (Soderberg et al 2007). As these materials show a larger work out put than the

conventional smart materials, the application area for these materials is wider as evident from Fig.1.2 showing a viewgraph classifying some typical applications. In addition to the classification based on field of application, a meaningful classification scheme from the materials standpoint could be based on functional requirements. Thus, the applications envisaged for the FMSM alloys emerge from their ability to deliver a large Magnetic Field Induced Strain (MFIS or λ) and include those in sensors and actuators in smart devices, large force delivery (with optimized force \propto Young's Modulus or optimised $E \cdot \lambda$) system in retractable missile wings and large energy packet (optimized $E \cdot \lambda^2$) delivery in SONAR transducers. With their combination of properties, these materials may improve the performance for some of the current devices using conventional magnetostrictive materials (e.g. in low frequency higher surveillance range sonar transducers in place of Terfenol-D) or a conventional shape memory alloys (faster response actuators and transducers like retractable wings in place of Nitinol). The response of such devices however is a function of frequency in addition to the other parameters (Tellinen et al 2002).

Specific volume changes during martensite / inter-martensite transformations in the FMSM alloys result in large strains. Martensite transformations are typically first order transitions without involving diffusion of atom and are reversible with external physical parameters such as temperature; applied stress conditions (uniaxial or hydrostatic pressure) and magnetic field etc., thereby giving these alloys a name of *shape memory alloys*. For a shape memory, the alloy when deformed in the low temperature phase, recovers its original shape by reverse transformation upon heating to a critical temperature called the reverse transformation temperature. First seen in Au-47.5 at% Cd alloy (Chang and Read, 1951), the shape memory effect was later reported in Ti-Ni alloys (Buehler *et al* 1963) as well. Thereafter, a series of shape memory alloys based on Fe, Ni, Cu and Ti systems (Otsuka and Wayman 1998) are already employed in technological applications and their metallurgy has been investigated (Otsuka and Ren 2005). These conventional shape memory alloys exploit transformations primarily with temperature changes. As a result while these alloys show a large recoverable strain, their response times have been longer due to the dissipation of heat to environment. In contrast, magnetic field application is the external parameter which can be switched at a much faster rate than the thermal cycling and hence Magnetic Shape Memory (MSM) alloys are being investigated extensively.

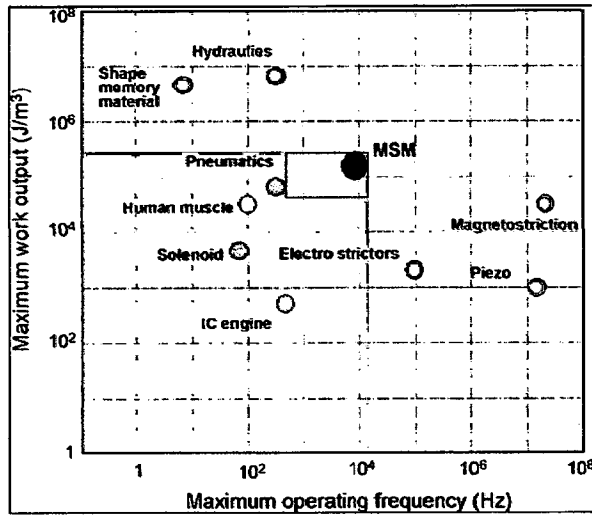


Fig. 1.1: Positioning of various actuator technologies. The magnetic shape memory bridges the gap between ‘smart’ and conventional actuator technologies. (Wilson et al 2007)

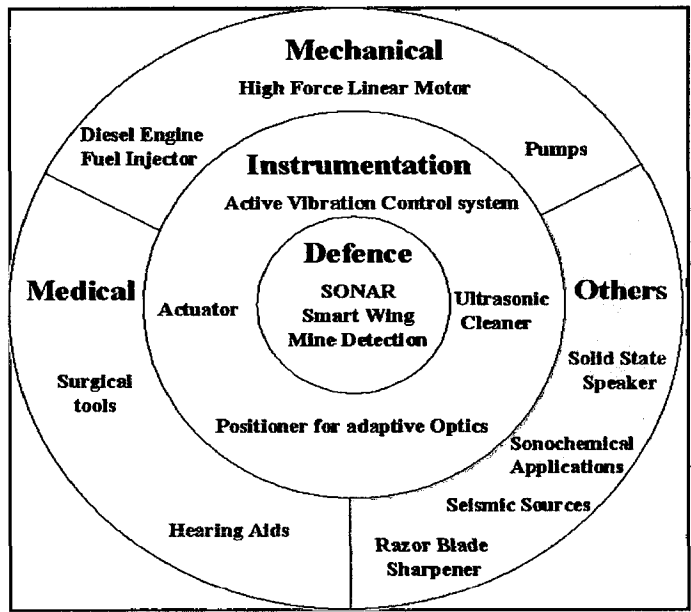


Fig 1.2: Typical applications of FMSM alloys in different walks of life

Alloys with transition elements may undergo martensite transformation under a magnetic field, the required energy for the phase change being provided by the magnetic energy. The driving forces for transformations through magnetic field are, however, smaller compared to thermal impetus and large magnetic fields are necessary to effect the transformation. This type of magnetic shape memory phenomenon is christened meta-magnetic shape memory effect (Kainuma et al 2006). The technological application of the phenomenon is, however, limited because of requirement of large magnetic fields.

The ferromagnetic shape memory effect is functionally similar; but is a distinct phenomenon from the meta-magnetic shape memory mentioned in previous paragraph. The martensite phases normally forming from a cubic precursor are low symmetry structures, commonly tetragonal or orthorhombic, having a preferred easy axis of magnetization in case of ferromagnetic alloys. Thermodynamically, austenite to martensite transformations result in formation of variants of the same martensite phase oriented so as to minimize the transformation strains, the phenomenon being known as self accommodation of the variants. The application of magnetic field on such self accommodated martensite variants results in reorientation of the variants thereby producing large recoverable strains under magnetic fields, much lower than that required for the transformations in meta-magnetic shape memory alloys. The phenomenon is called Ferro-Magnetic Shape Memory (FMSM) effect and the alloys capable of undergoing this effect are called FMSM alloys. Ferromagnetic shape memory (FMSM) effect has been reported (Ullakko et al, 1996) in Ni-Mn-Ga system. A large (0.2%) magnetic field induced strain (MFIS) in an unstressed [001] single crystal of Ni₂MnGa in 800 kAm⁻¹ magnetic field at 256 K has been realized. A range of alloys based on transition elements such as Fe₃Pt, Fe-Pd and Ni-Mn-Ga alloys have shown the FMSM phenomenon at temperatures where ferromagnetic martensite phase exists (Kakeshita and Ullakko 2002). The application temperature is very low for the Fe₃Pt and Fe-Pd alloys; however, Ni-Mn-Ga alloys are reported to show the phenomenon near room temperature. The interest in this phenomenon in Ni-Mn-Ga alloys has gained considerable attention amongst the researchers from the application point of view. The magneto-structural phenomenon in this type of alloys is explained on the basis that twin variants of the martensite phase are redistributed by the application of magnetic field. Due to redistribution of the twin variants a

large strain is obtained without a change in the external temperature (Lieu et al 2004). The reversibility in strain can be obtained by either the application of compressive stress or magnetic field in direction perpendicular to the original applied field (Tickle and James, 1999). The Ni-Mn-Ga alloys have thus shown tremendous potential as smart or intelligent materials and are being employed as actuator and sensors (Adaptamat Ltd, Finland, www.adaptamat.com).

In view of the technological importance of the FMSM alloys, Ni-Mn-Ga alloys along with other potential alloy systems have received attention of the materials scientists globally. The interest in the FMSM alloys can be gauged with the number of publications emerging in the recent past as shown in Fig 1.3 (Chernenko, 2007). Details about some of these publications are covered in the next chapter on literature review. However, a majority of them covers the preparation and characterization of ternary Ni-Mn-Ga alloys. About a sixth of these publications are devoted to alternate alloy system iso-structural with Ni-Mn-Ga alloys. Major alloy development programs usually involve multi-component systems wherein individual components add to improvement in or more functional properties. Information on multi-component FMSM alloys however is very limited and the present study plans to cover this grey area by systematically investigating the effect of quaternary additions in a ternary base composition of $\text{Ni}_{50}\text{Mn}_{30}\text{Ga}_{20}$.

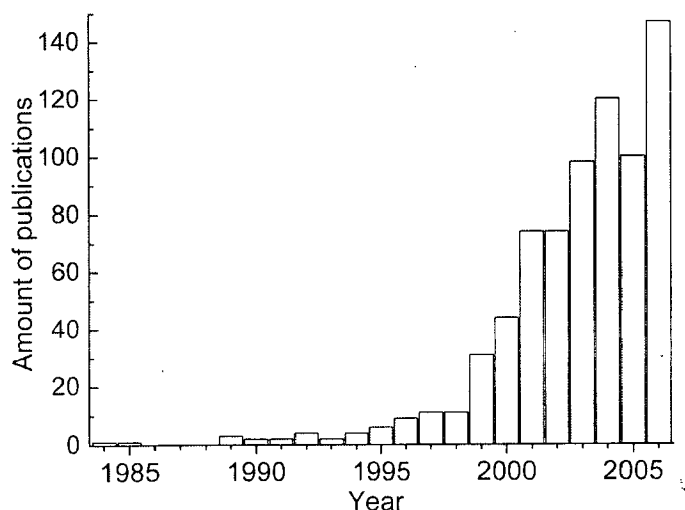


Fig 1.3: Growth in number of publications on FMSM alloys (Chernenko 2007)

The dissertation begins with a review of available literature in the field and identification of the gap in knowledge, wherefrom the scope of the present study emerges. Alloy development begins with alloying addition to substitute the transition elements as well as trivalent Ga in $\text{Ni}_{50}\text{Mn}_{30}\text{Ga}_{20}$. The transition element Fe or Co have been added to substitute either Ni or for Mn in the aimed compositions. Trivalent Al and/or B have been added as substitute for Ga based on valency, whereas addition of rare earth Sm or Dy have been attempted for Ga based on the size. The influence of processing route of the alloys has been investigated in the limited context of conventional casting and heat treatment, and rapid solidification by characterizing their structural, magnetic and thermal properties and transformations. The obtained results have been analyzed and correlated in terms of the effect of the quaternary elements and their atomic site occupation.

2.1 INTRODUCTION

The functional properties of the FMSM alloys are derived from the reorientation of ferromagnetic martensite phase variants. The study for these alloys therefore needs an understanding of the martensite phase and transformations leading to them. The desired martensite phases are required in a ferromagnetic state in order to respond to external magnetic fields. A brief introduction to basics of magnetism is required to understand the responses of various materials under the magnetic field. Some ferromagnetic martensites may show reversible shape changes as a response. The magnetism and magnetic properties of these materials, their responses leading to FMSM phenomenon and the manner which the chemistry/ processing may modify the functional properties of the alloys are the primary requisite to understand the material system. This chapter accordingly discusses the available literature information on (i) the basics of magnetism (ii) Ferro-Magnetic Shape Memory (FMSM) effect and (iii) Metallurgy of Ni-Mn-Ga alloy system with emphasis on the Ni_2MnGa structure and their characterization.

2.2 BEHAVIOUR OF MATERIALS UNDER EXTERNAL MAGNETIC FIELDS

Magnetism mainly arises from the orbital and spin motions of electrons in atoms. The moving charges i.e. electrons behave like tiny magnets due to these motions. The magnetic moment of an electron due to spin alone is the smallest unit of the magnetic moment called a 'Bohr magneton'. The behavior of materials under an external magnetic field is essentially the collective response of the atomic magnetic moments to the applied field. At the atomic level, majority of the magnetic moment of the electrons cancel out because of the Pauli's exclusion principle, which states that each electronic orbit can be occupied by only two electrons of opposite spin. However, in case of unfilled electron level in 3d and 4f shells of

transition metals and rare earth elements, such magnetic moments are not cancelled. These elements therefore show perceptible magnetic moments. In transition elements, the magnetic moment arise only from the spin of the electrons and the orbital moments are quenched due to crystal field effects. As the unfilled orbits are deeply located, the rare earths have unquenched orbital moments and both the spin and the orbital moments contribute to the magnetic moment. Different elements when combined in alloys and compound have their net magnetic moments responding differently to the applied external field. Materials are accordingly classified as ferromagnetic, ferrimagnetic, antiferromagnetic, paramagnetic, and diamagnetic (Lacheisserie et al 2003). While the net magnetic moment of a diamagnetic material is zero due to pairing of electrons with opposite spins, the paramagnetic materials show a negligible magnetic moment due to thermally disordered moments. Cooperative phenomenon between the atomic magnetic moments due to exchange coupling and spontaneous magnetization are the characteristics of ferromagnetic materials and their magnetic behaviour is explained through domain theory. Negative exchange coupling between equal and unequal atomic moments leads to anti-ferromagnetism and ferrimagnetism. Both ferromagnetic and ferrimagnetic materials show perceptible magnetic moments, though at atomic levels the former having atomic moments aligned parallel whereas the latter having a unequal magnetic moments coupled anti-parallel to each other. It may be noted that the net magnetic moments are function of temperature, atomic separations etc. and the same material may behave differently at different temperatures with transitions defined by various laws such as Curie or Curie-Weiss laws.

The magnetization, M of a material is measured and plotted as a function of external applied field H and a typical M - H curve, also known as an intrinsic hysteresis loop, is shown in Fig.2.1. Initially, the material is in virgin magnetization state, and when the field is applied, the magnetization vector undergoes reversible rotation within the domain and accordingly reversible domain wall rotation takes place. As the field increases, domains with their moments aligned parallel to the applied field grow at the expense of the domain whose moments are not favorably orientated with the direction of field. This part of the curve is referred to as the virgin curve, or initial magnetization curve. At sufficiently high field when

the saturation magnetization (M_s) is reached domain walls no longer exist. The material is then said to be uniformly magnetized with $M = M_s$. When the external magnetic field is removed, the value of magnetization measured is non-zero and is called the remanent magnetization M_r . The magnitude of this remanent magnetization depends on the distribution of the easy axes in the material. For a perfectly aligned material, the remanent magnetization is equal to the saturation magnetization and $M_r/M_s = 1$.

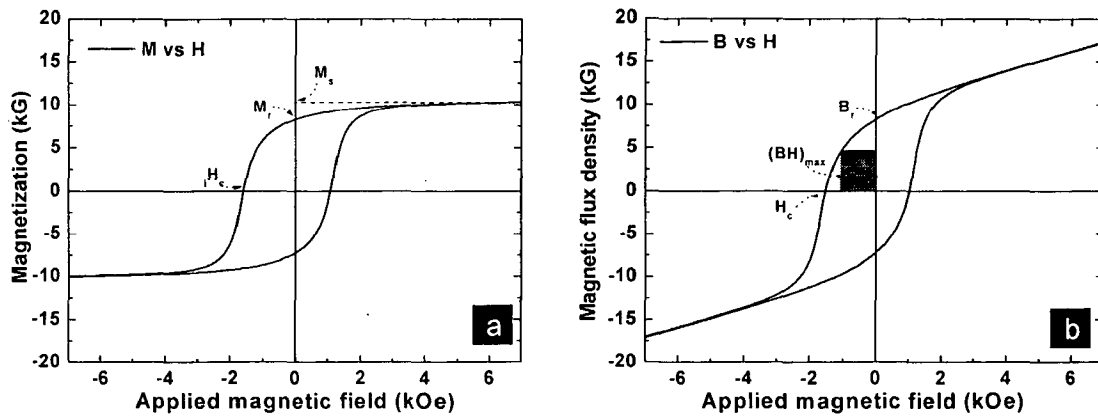


Fig 2.1: Typical hysteresis curves for a magnetic material (a) $M - H$ loop (b) $B - H$ loop. The shaded rectangle in the second quadrant of $B - H$ curve represents the energy product, $(BH)_{max}$. The two plots are related by the equation $B = H + 4\pi M$ (CGS).

For a material with isotropic orientation of the grains, this ratio, called the remanence ratio, is about 0.5 though larger values than this reported in case of exchange interaction at nanosizes. When a sufficiently large reverse magnetic field is applied, the magnetization will be reduced to zero at the coercivity H_c . This occurs by non-reversible rotation of the magnetization or by the nucleation and propagation of the reverse domains. The coercivity is a measure of the magnet's resistance to demagnetization by reverse fields. The coercivity H_c from the $M-H$ loop (Fig.2.1a) is known as the intrinsic coercivity. Hysteresis loop shown in Fig.2.1.b is known as the $B-H$ curve or $B-H$ loop. The $B-H$ loop is more useful to characterize hard magnetic materials as it allows the evaluation of the maximum energy product, $(BH)_{max}$ signifying the stored magneto-static energy as a figure of merit for permanent magnets. The hysteresis curves

show the effect of alignment of the internal magnetic moments of the materials. Such curves therefore have been used extensively to determine the suitability of materials for delivering the magnetic fields as permanent or electromagnets.

It may be noted that a host of physical properties of the materials stands changed when the electron parameters such alignments, and orbital etc. are modified. In the recent decades, modifications in the physical properties under a magnetic field have opened up fascinating applications for the magnetic materials. The properties like physical dimensions, transport properties viz electrical resistance or the impedance and the free energy of the materials are reported to undergo a change under a magnetic field. The free energy changes during magnetization are being exploited as environment friendly magneto-caloric refrigeration applications and the materials with large magneto-resistance or the magneto-impedance effects are employed as sensors. The materials with reversible dimensional changes on magnetization are used as smart materials as they can both sense and act on external impetus.

The dimensional change on magnetization is an important magnetic property called 'magnetostriction' derived from the words Magnet (Greek) + Strictus (Latin) literally meaning dimensional change with magnet. This phenomenon is a common occurrence for all the substances. Saturation magnetostriction (λ_s) of a material is defined as change in physical dimensions in response to magnetic field.

$$\lambda_s = \Delta L / L$$

Where ΔL is the change in length and L is the original length of the material. Most ferromagnetic materials exhibit some measurable magnetostriction. Cobalt as an element shows a highest room temperature saturation magnetostriction of 60×10^{-6} (or 60 microstrains). The cubic laves phase iron alloys containing the rare earth elements Dy or Tb (eg. DyFe_2 , and TbFe_2) have shown magnetostriction up to about 2000 microstrains in a field of 2 kOe at room temperature under a mechanical-bias. Being pioneered by the Naval Oceanographic Laboratory (NOL), USA, and the giant magnetostrictive materials of the form $\text{Tb}_x\text{Dy}_{1-x}\text{Fe}_2$ are commonly called as Terfenol-D (TERbium- FERRum-NOL- Dy). The mechanism of magnetostriction at an atomic level is relatively a complex subject matter but

on a macroscopic level may be segregated into two distinct processes of domain wall movement and domain rotations at higher fields. These mechanisms allow the material to change the domain orientation which in turn causes a dimensional change. Excepting forced magnetostriction at very large magnetic fields, such deformation is normally isochoric i.e. without volume change and an opposite dimensional change in the orthogonal direction appears as a result. Although there may be many mechanisms to the reorientation of the domains, the basic idea of the rotation and movement of magnetic domains is represented schematically in Fig.2.2 showing a physical length change in the material.

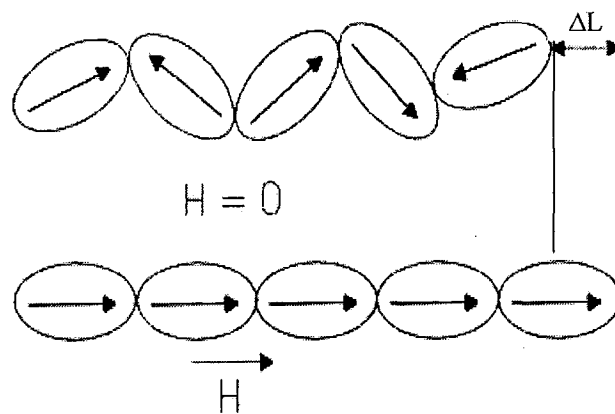


Fig 2.2: Schematic reorientation of magnetic moments giving Magnetostriction phenomenon.

The reversible behavior of the strains like hysteresis curves can be shown graphically as λ -H curves shown in Fig 2.3. Like the M-H or B-H hysteresis curves, these curves also show different paths during magnetization/ demagnetization. As the dimensional change is immaterial of the direction of magnetization these curves have a butterfly shape and are accordingly referred to as butterfly curves. It may be pointed out here that a reversible magnetostriction of a few percent has been reported in Ni_2MnGa single crystals. Such large values cannot be explained by a mere rearrangement of the electronic cloud and has been explained through different mechanism of ferromagnetic shape memory phenomenon described later.

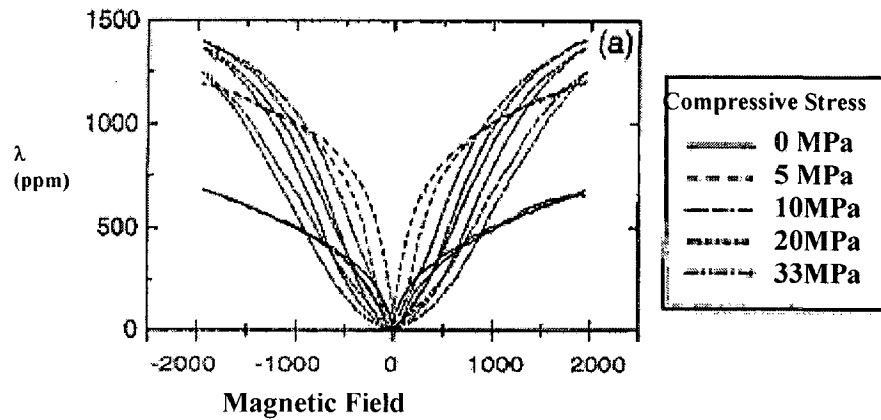


Fig 2.3: λ -H Curves (Butterfly curves) obtained for a typical magnetostrictive material (Terfenol-D) measured at different compressive stress level.

2.3 FERRO-MAGNETIC SHAPE MEMORY EFFECT: EVOLUTION AND THE ALLOY SYSTEMS

The shape memory i.e. recall of shape with reversible temperature has been known for more than a half century. Conventional shape memory phenomenon was first reported for an Au-Cd alloy (Chang and Read 1951) and for Ti-Ni alloys (Buehler et al 1963). The initial findings were followed by reports for other alloy systems as well (for a review Otsuka and Wayman 1998) and a range of alloys are known today displaying the phenomenon. In addition to shape memory phenomenon, these alloys also showed super-elasticity or a large nonlinear recoverable strain on loading and unloading. Both the super-elasticity as well as the shape memory phenomenon is attributed to reversible martensite transformations. The alloy undergoing martensite transformation changes its shape due to formation of low symmetry martensite phase; on heating reversible transformation to high temperature phase causes the recall of the shape. Majority of the alloys showing these transformations belong to BCC structure around electron to atom ratio of 1.5. The ordered BCC structure of the alloys is stabilized due to nesting at the Brillouin zone boundary. At lower temperature entropy term in Gibbs free energy becomes negligible and the requirement of decrease in internal energy drives the parent phase structure to low symmetry to long period stacking order structure also called super period structures of martensite. The martensitic transformation is a

diffusion-less structural phase transformation in solids, in which atoms move cooperatively, and often by shear-like mechanism. The periodicity and modulations in long period superlattices are represented in notations such as Ramsdel notation and Zdanov symbol in literature (Otsuka and Wayman 1998). The Ramsdel notation gives a number and a letter, the number representing the number of atomic layers in super period and the letter representing the crystal structure, though the letter M for modulated martensite is sometimes used without specifying the crystal structure. Normally a thermal energy driven transformation, the martensite transformation can under suitable conditions be affected by other physical impetus such as mechanical forces like strain, hydrostatic pressures or magnetic field.

The functional property of the FMSM alloys *viz.* Magnetic Field Induced Strain (MFIS) is attributable to atomic rearrangements under magnetic fields unlike the electronic rearrangement in case of magnetostrictive materials. The exact mechanism of the large reversible strains is reported to be due to a combination of either a martensite transformation or twin variant conversion and reorientation directly by applied field or indirectly by the magnetic force generated by non uniform magnetic field (Wilson et al 2007).

The FMSM phenomenon has been reported as early as 1968 in Dy single crystals at low temperatures. (Rhyne et al 1968, Libermann and Graham 1977). Similar to the conventional shape memory alloys, the alloy systems undergoing martensite transformations possessing a net magnetization show such phenomenon under suitable conditions (Kakeshita and Ullakko 2002) with the parent austenite phase having a variety of crystal structures (Table-2.1). Martensite phase is a lower symmetry phase as compared to the parent or the austenite phase. Since there are usually several crystallographically equivalent ways to deform the high symmetry structure into low symmetric structure, the deformation may take different directions in different regions of the sample to form the same type of martensite crystal structure, thus generating the orientation variants of the phase. In general martensite transformation is accompanied by volume change and in order to get shape memory effect this change in volume should be minimum (< 1%). This condition is achieved by self accommodation of martensite variants, which gives rise to twinned microstructure as shown in Fig 2.4. The two variants of the martensite are twin related to each other with well defined twin boundary between them.

Table 2.1: Comparison of some FMSM alloys (Kakeshita and Ullakko 2002).

	Ni₂MnGa	Fe₆₉Pd₃₁	Fe₃Pt
Structure	L2₁	A3	L1₂
T _c (K)	380	600	430
T _{ms} (K)	318	225	85
c/a (measured at temperature K)	0.940 (4.2)	0.940 (77)	0.944 (14)
Easy Axis	c-axis	a-axis	c-axis
Max Strain (%)	6	3.1	-2.2

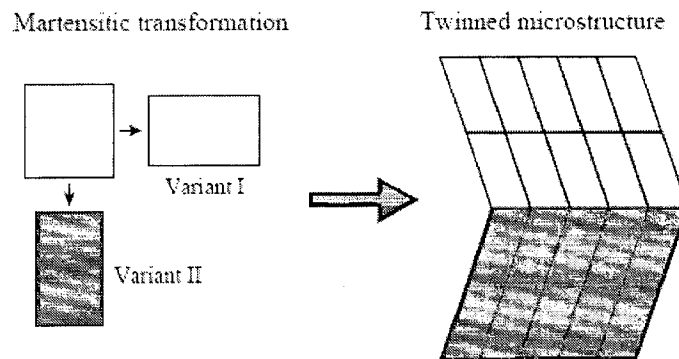


Fig.2.4: Schematic illustration of martensite transformation and twinning in two dimensions.

The mobility of inter-variant twin boundaries is exploited for functional applications in the temperature driven shape memory effect. The easy movement of the twin boundaries permits an easy deformation of the sample device in the martensite phase. When the material is heated back to the austenitic phase, the sample reverts back to its original shape, i.e. it “remembers” the shape it had before cooling. Even though the strains in the temperature-driven shape memory effect is large up to several percent, the heating and especially the cooling (i.e. dissipating heat to the surrounding) are relatively slower rate controlling

processes. Ways and means to drive the shape change with a faster response are necessary for many fast switching/ high frequency applications. The magnetic degree of freedom instead of temperature overcomes the slower response times and permits faster responses.

Magnetic materials such as ferromagnets, anti-ferromagnets and ferrimagnets are characterized by their spontaneous magnetizations. In absence of an external magnetic field their magnetic moments have a preferable direction with respect to the crystal lattice, commonly referred as easy direction of magnetization. In a twinned microstructure the lattice orientations of the twin variants are different and therefore the magnetization directions also differ, as shown in Fig. 2.5a.

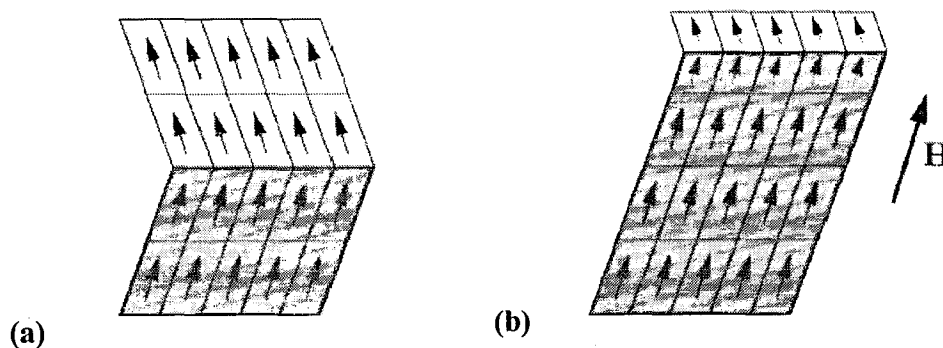


Fig.2.5: Schematic magnetic moments in the twinned martensite (a) Magnetic moments without magnetic field and (b) Redistribution of variants in magnetic field.

When an external magnetic field is applied, the magnetic moments try to align with the field. If the energy needed to rotate the magnetization away from the easy direction (i.e. the magnetic anisotropy energy) is high enough, it may be energetically favorable to move the twin boundaries instead of the magnetic moment alone. In such a case the fraction of twins with the easy axis in the direction of the field grows at the expense of the other twin variants by the application of magnetic field as shown in Fig. 2.5b. This process results in large shape changes as shown schematically in Fig.2.6, with a little contributions from other factors mentioned earlier. This phenomenon is called ferromagnetic shape memory effect.

The basic requirements for the appearance of the FMSM effect therefore emerges as a (ferro)magnetic materials exhibiting martensite transformation with magnetic martensite at operating temperatures ; and an adequate magnetic anisotropy energy providing the energy needed to move the twin boundaries (detwinning) . The strength of the required external field depends on the local magnetization of the material, so the magnetic moment should be high. Adequate magneto-crystalline anisotropy energy coupled with high saturation magnetization is, therefore, required for these materials. It may be noted that suitable martensite variants (described later) is also an essential requirement and such variants form only when martensite transformations are lower than Curie transition temperatures.

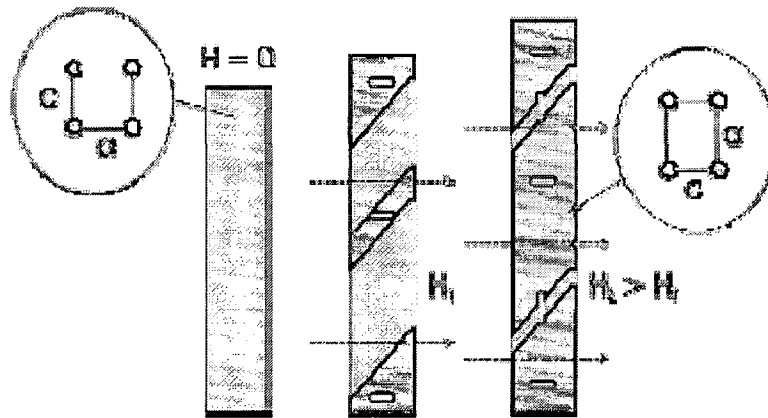


Fig.2.6: Schematic of growth of preferentially oriented variant in magnetic field and corresponding change in crystal orientation resulting in large deformation (Tellinen et al 2002).

A look at table 2.1 shows that though a range of alloys show the phenomenon, martensite transformations are usually low temperature transformations and as such the phenomenon had been limited to low temperatures permitting exploitation in practical devices at cryogenic temperatures only. With the reports (Ullakko et al 1996) that the transformation temperature of the Heusler alloy derivative Ni-Mn-Ga alloys are high enough to qualify for practical applications, these alloys are being investigated in great details. For elevated temperature operations, high martensite transformation temperatures with higher Curie temperatures are required. Various alloys iso-structural with Ni-Mn-Ga systems are

therefore being explored. The criteria for predicting the ferromagnetic shape memory phenomena for a range of alloys have been proposed recently based on average number of electron per atom (Slater- Pauling Curves) or energy wells in free energy densities of martensite phase permitting favorable low energy microstructures (Wuttig et al 2000). Of these systems, the Heusler alloys containing at least one of Ni, Mn, Co or Fe as constituent elements contributing magnetism to the alloy system have shown a large promise. Like the binary alloys (table 2.1), ternary alloys based on transition metals displaying FMSM phenomenon may also belong to different crystal systems. Co-Ni-Al alloys with $L1_0$ structure show thermo-elastic martensite (Valiullin et al 2006). Majority of the ternary FMSM alloys however possess high temperature structure derived from BCC crystal structure with *structureberitch* classification $L2_1$. The ordered doubled bcc cell is described by the space group $Fm\bar{3}m$ (Fig 2.7b). The alloys with this space group are also called the Heusler alloys having the formula X_2YZ . The first Heusler alloys based on copper-manganese-aluminum were ferromagnetic whereas their individual constituent elements were not. The $L2_1$ alloys with a martensite transition below magnetic transition, i.e. with a ferromagnetic martensite transition are listed in table 2.2 (Wuttig et al 2000). The alloys in table 2.2 have element X as a ferromagnetic, element Y i.e. Mn as anti-ferromagnetic and element Z as a non-magnetic element. Though the alloys have similar atomic structure, their physical, metallurgical and crystallographic properties are considerably different being function of atom type and the inter-atomic distances etc. Their technologically important properties viz FMSM strains, operating temperature and mechanical properties vary considerably and different alloys may suit different windows of functional requirements. For example, Co-Ni-Al based alloys are reported to possess better workability in the class of $L2_1$ FMSM alloys (Oikawa et al 2001). Many of these alloys also have been systematically investigated for their functional properties (Li et al 2003) or for their atomic structures (Bhobe et al 2008).

Table 2.2 shows that many alloys have potential for applications as FMSM alloys and may have their relative advantages over other candidates. The Ni-Mn-Ga system has however shown adequate mix of properties to be exploited as active material for the FMSM devices. The available information on the metallurgical aspects of Ni-Mn-Ga alloys and their relevance to magnetic property are therefore presented in next section.

Table 2.2: Heusler Alloys with electron/atom ratio in the range where FMSM may be found. (Wuttig et al 2000).

Alloy(X ₂ YZ)	Curie Temperature (K)	Electrons per atom (e/a)
Co ₂ MnIn Fe ₂ MnP Co ₂ MnAl Co ₂ MnGa Ru ₂ MnSb Rh ₂ MnAl Rh ₂ MnGa Rh ₂ MnIn	693 694 Tn=200	7
Co ₂ MnGe Co ₂ MnSn Rh ₂ MnGe Co ₂ MnSi Rh ₂ MnSn Ph ₂ MnPb	829 985 410 355	7.25
Pd ₂ MnGa Ni ₂ MnGa Ni ₂ MnAl Co ₂ MnSb Pt ₂ MnAl Pd ₂ MnIn Rh ₂ MnSb	379 Tn=50 323 Tn=150	7.5
Ni ₂ MnSn Pd ₂ MnGe Pd ₂ MnSn	345	7.75
Ag ₂ MnIn Cu ₂ MnAl Ni ₂ MnSb Cu ₂ MnSn Pd ₂ MnAs Cu ₂ MnIn Au ₂ MnAl Pd ₂ MnSb Cu ₂ MnGa	603 331 530 500 220 >RT	8
Cu ₂ MnSb		8.5

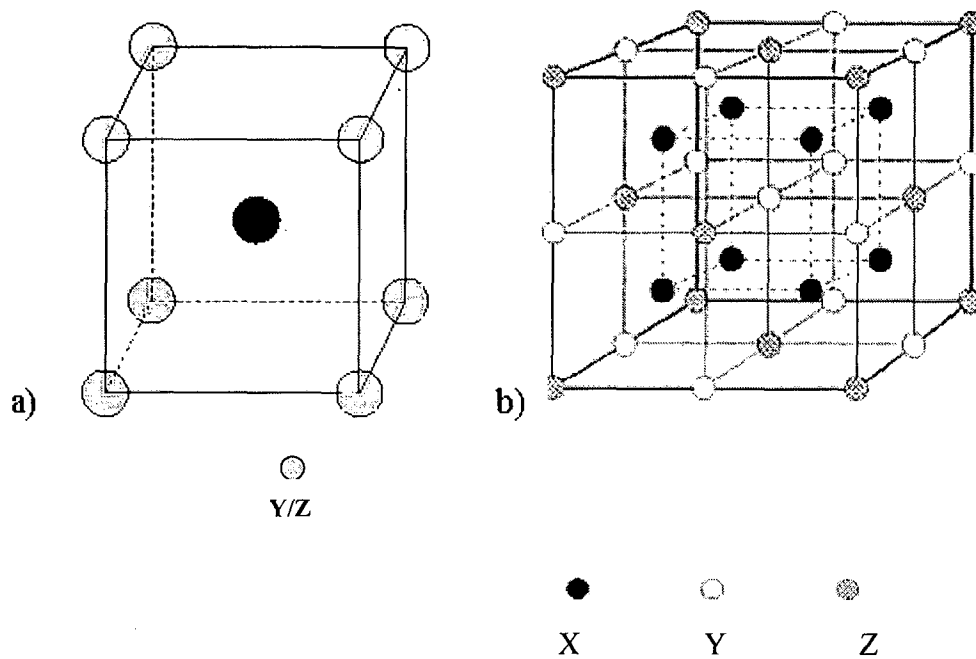


Fig 2.7: Atomic structure of ordered X_2YZ type alloys derived from BCC structure (a) $B2'$ structure with equivalent sites for Y and Z and b) $L2_1$ structure.

2.4 METALLURGY OF Ni-Mn-Ga ALLOYS

2.4.1 Equilibrium Phase Transformations

Structural Transitions

Binary phase diagrams of the constituents have been compiled (American Society of Metals) and are shown in Fig 2.8. The binary Ni-Mn system (Fig 2.8a) shows a stable martensite transformation. The transformation of η into η' is martensite of nearly thermo-elastic nature. Martensite structure was observed in the alloys within the region with 50 at.% Ni or less after quenching. The martensite plates were internally twinned on $\{111\}$ planes. Slow cooling from η and $\eta + (\gamma\text{Mn,Ni})$ regions with less than 50 at.% Ni became tempered and exhibited low-density twins crossing one another. Ni-rich quenched alloys showed a finely twinned structure different from martensite, with a twin plane of $\{101\}$ due to ordering. The crystal structure of both Ni-rich and Ni-lean phases were the same $L1_0$ structure.

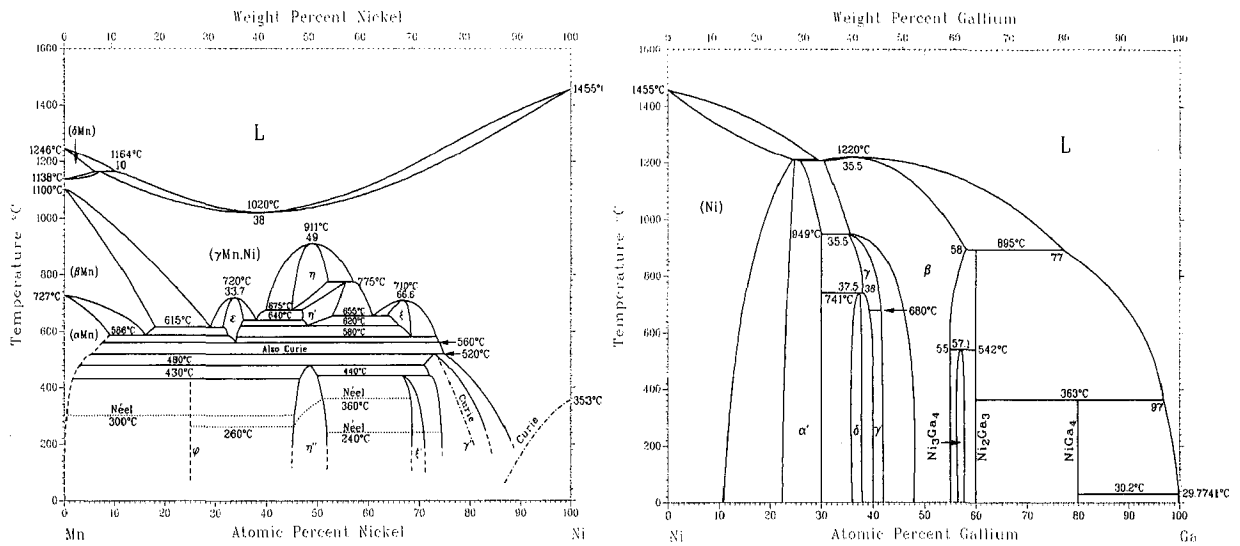


Fig.2.8: Binary phase diagram of Mn-Ni and Ni-Ga.

Detailed ternary phase diagram of the Ni-Mn-Ga system are not reported to our knowledge. However, technically important sections of ternary phase diagrams showing either phase transformations or the physical property variations (such as T_c variations) have been drawn using theoretical calculations as well as experimental data.

Magneto-structural free energy minimization using Ginzburg-Landau theory has been used to generate phase diagrams for $Ni_{2+x}Mn_{1-x}Ga$ for ferromagnetic and martensite transitions (Zayak et al 2002). The phase diagrams generated are shown in Fig.2.9-2.11. A pre-martensite transformation of high temperature cubic phase to intermediate phase is proposed to precede the modulated martensite structure. The intermediate phase is the parent cubic phase derived through modulation by transverse waves.

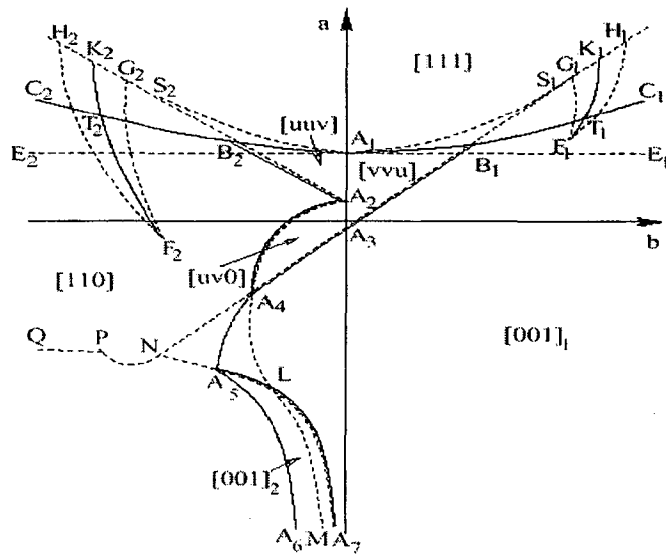


Fig 2.9: Schematic phase diagram of the cubic ferromagnet in the (a; b) plane. The solid curves represent phase transitions; the dashed curves are stability boundaries. Dashed and solid lines approaching each other mark a second-order phase transition. (Zayak et al 2002)

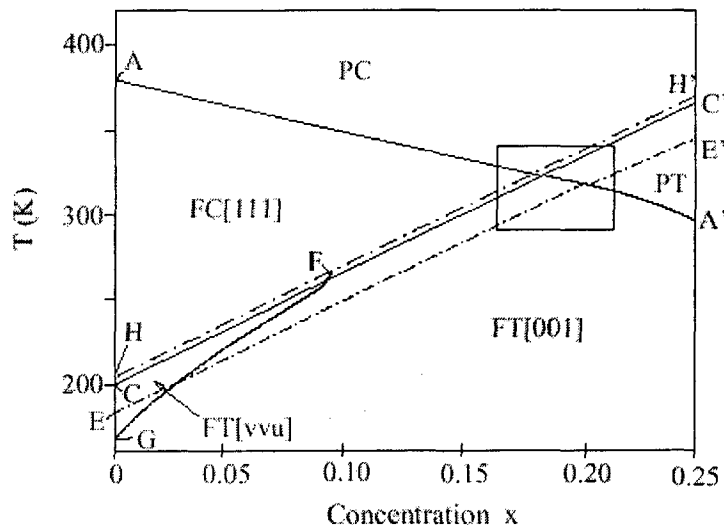


Fig 2.10: The phase diagram of the ferromagnet $\text{Ni}_{2+x}\text{Mn}_{1-x}\text{Ga}$ in the (T;x) plane. The dotted line represents a first-order phase transition; dash-dotted lines are stability area boundaries; solid lines represent phase transitions of second-order. The phases are labeled as P: paramagnetic state, C: cubic lattice, F: ferromagnetic state and T: tetragonal lattice (Zayak et al 2002).

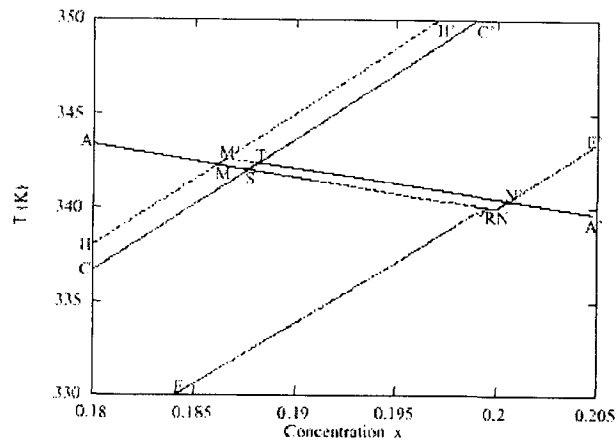


Fig 2.11: Full (T;x) phase diagram of $\text{Ni}_{2+x}\text{Mn}_{1-x}\text{Ga}$ showing the region of TC and TM intersection. The dotted line corresponds to 1st-order phase transitions; dashed and dash-dotted lines mark the stability boundaries; the solid line represents phase transitions of second order (Zayak et al 2002).

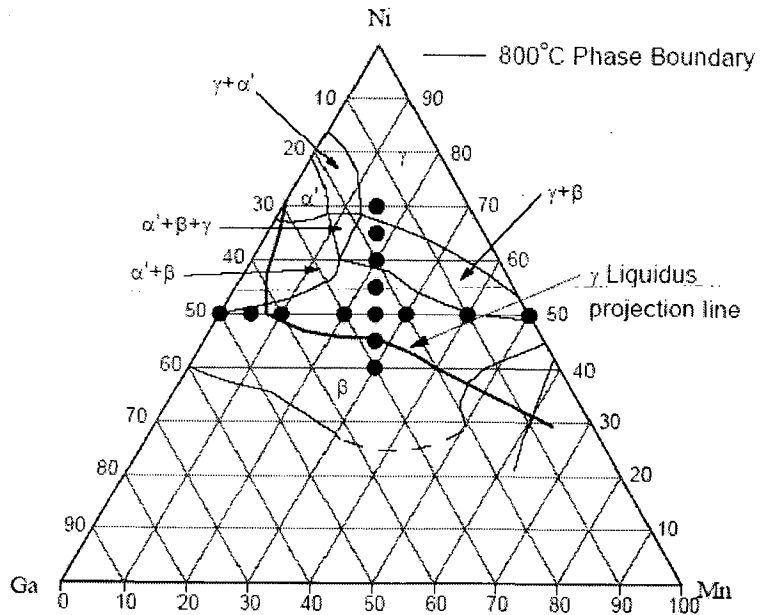


Fig.2.12: Isothermal section of ternary Ni-Mn-Ga phase diagram at 800 °C (Chen et al 2004).

The information on experimental ternary phase diagram of the alloy system is scanty and limited section / portions on the compositions nearby the stoichiometric Heusler composition are available. The shape of liquidus surface, which is critical for controlling the solidification process, is unknown. However, the 800 °C and 1000 °C isothermal sections for ternary Ni-Mn-Ga alloys are available and isothermal section at 800 °C is shown in Fig.2.12 (Chen et al 2004). For the alloys close to the stoichiometry composition ($\text{Ni}_{50}\text{Mn}_{25}\text{Ga}_{25}$), the FCC γ -Ni solid solution phase solidifies first from the liquid, as per the binary phase diagram Fig.2.8 and the ternary phase diagram Fig 2.12. At 800 °C the β -NiMnGa phase covers the large area of the ternary phase diagram, including the compositions close to stoichiometry. The β -NiMnGa phase has B2' CsCl structure at high temperature and changes to the $L2_1$ Heusler type structure at lower temperature.

The ordering sequence in $\text{Ni}_{50}\text{Mn}_x\text{Ga}_{50-x}$ has been studied using neutron diffraction and Differential Thermal Analysis (DTA) techniques (Overholser and Wuttig, 1999). Analytical calculation based on Bragg-Williams-Gorski (BWG) approximation for the order parameters have been made using Murakami model proposed for off-stoichiometric Heusler alloys and matches well with the ordering sequence liquid \rightarrow B2' \rightarrow $L2_1$. Fig 2.13 shows the quasi-binary phase diagram illustrating the observed liquid \rightarrow B2' \rightarrow $L2_1$ experimental data along with calculated boundaries for A2 \rightarrow B2' and B2' \rightarrow $L2_1$ transitions as per Murakami model. The solid-solid weak enthalpy changes for B2' \rightarrow $L2_1$ were corroborated by DTA thermo-grams (Fig 2.14). The phase B2' in the report was not retainable in annealed alloys after quenching. The peaks corresponding to the B2' \rightarrow $L2_1$ change is so shallow that it is difficult to conclude if there is peak area corresponding to it or just a slope change. The order of this transition cannot be concluded based on DTA data. The experimental DTA as well as the neutron diffraction did not suggest the existence of an A2 \rightarrow B2' transition.

For the alloys close to the stoichiometry composition ($\text{Ni}_{50}\text{Mn}_{25}\text{Ga}_{25}$), the FCC γ -Ni solid solution phase solidifies first from the liquid, as per the binary phase diagram Fig 2.8 and the ternary phase diagram Fig.2.12. At 800 °C the β -NiMnGa phase covers the large area of the ternary phase diagram, including the compositions close to stoichiometry. The β -NiMnGa phase has B2' CsCl structure at high temperature and changes to the $L2_1$ Heusler type structure at lower temperature. In Ni-Mn-Ga Heusler alloys the $L2_1$ cubic structure of parent phase (P) is highly ordered (Fig 2.7b). This $L2_1$ ordered structure can arise from the high temperature disordered A2 phase either directly (A2 \rightarrow $L2_1$) or via the intermediate B2' phase (A2 \rightarrow B2' \rightarrow $L2_1$) (McCormack and de Fontaine 1996).

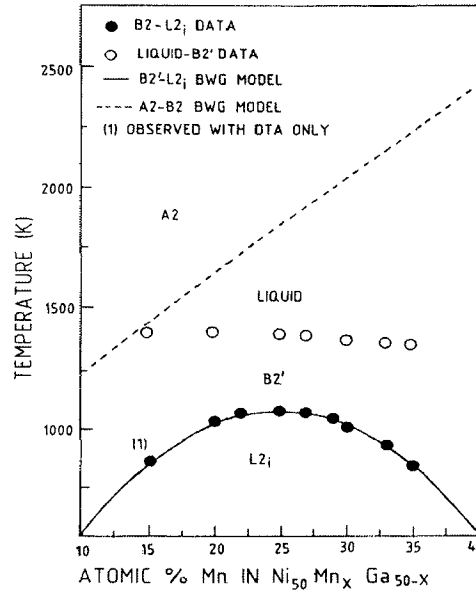


Fig.2.13: Quasi-binary temperature composition diagram showing experimental transition (Overholser and Wuttig 1999).

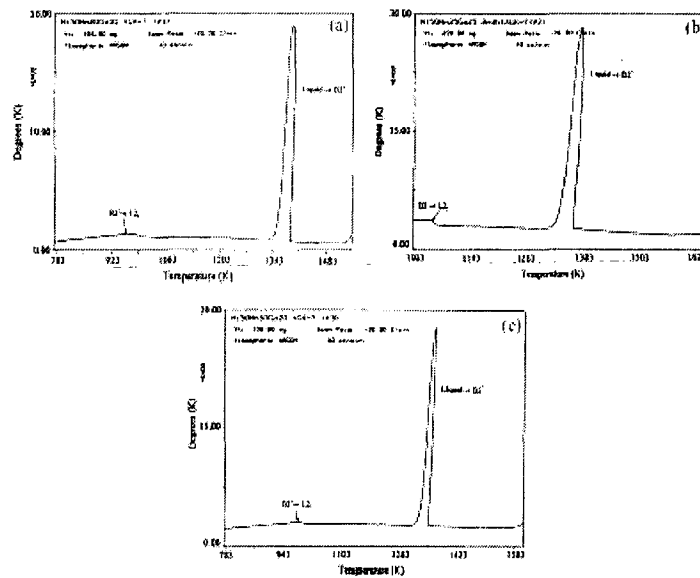


Fig 2.14: DTA cooling scans showing Liquid→B2' & B2'→L2_i transitions in Ni₅₀Mn_{25+x}Ga_{25-x} alloys for x= (a) -5 , (b) 0 and (c) 5 (Overholser and Wuttig 1999).

Magnetic transitions

At the Curie point (T_C), a ferromagnetic material becomes paramagnetic by losing the long-range magnetic order. The FMSM alloys require a ferromagnetic martensite at the operating temperatures for functional applications, a lower magnetic transition is sometimes a major constraint limiting the service temperatures of the alloys. The magnetic moment of Ni-Mn-Ga alloys originates mainly from Mn having the largest magnetic moment, while a small magnetic moment from the Ni sites is also assigned (Kudryavtsev et al 2001). Experimental T_C data for a wide range of Ni-Mn-Ga alloys are shown in Fig 2.15 with superimposed contours of a second-order, two variable polynomial fitting curves (Jin et al 2002). The Ni-Mn-Ga alloys appears to have Heusler phase with a relatively stable ferromagnetic transition temperature over large range of composition (Mn: 20-35 at%, Ga 16-27 at%).

The contours of constant T_C show that T_C of the Ni-Mn-Ga alloys is lowered with increasing Ni content. In Ni-Mn-Ga alloys with $e/a < 7.6$ -7.62 the martensitic transformation takes place below T_C , while in the alloys with $e/a > 7.62$ -7.7 the structural transformation occurs in the paramagnetic state. The co-occurrence of the structural and magnetic transitions has recently been studied more, due to the possibility of the magnetocaloric effect. The cubic parent phase and the tetragonal martensite phase both have their own Curie points with an approximately 30 K difference. The Curie point of the low-volume tetragonal martensite was higher than that of the high-volume cubic parent phase. In addition to the different lattice volumes, the different Curie points were explained by the dissimilar Mn-Mn atom distances and the different electronic structures.

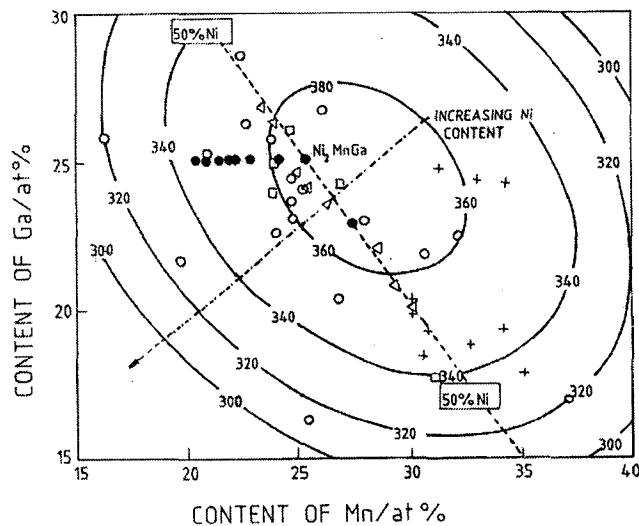


Fig.2.15: Contour view of curve fitted Curie temperature T_C (K) with experimental data (Jin et al 2002)

2.4.2 Martensite Structures and Variants

The neutron diffraction studies on single crystals of the Ni₂MnGa alloys have been carried out at different temperatures revealing a L₂₁ structure at high temperature and three different crystal structures at lower temperatures of 230 ,215 and 20K (Brown et al 2002). Table 2.3 shows the position of constituent atoms in the space group Pnnm refined from the diffraction studies. The transformation of L₂₁ structure to a stable martensite occurs through intermediate phases. The phases termed as precursor, pre-martensite phases are described by orthorhombic cell with different periodicity of the super structure.

The martensite super-period structures are schematically shown in Fig 2.16. The three layered tetragonal martensite can be obtained from the parent structure similar to Bain transformations. The 5 or 7 layered long period structures designated as 5M (Webster *et al* 1984) or 7M (Martynov and Kokorin 1992) are commonly encountered in Ni-Mn-Ga alloys and are produced with modulated placement of atoms as shown in Fig 2.17 (Brown et al 2002).

Table 2.3: Atomic positions for the Ni₂MnGa refined in space group Pnnm based on neutron diffraction patterns at different temperatures (Brown et al 2002).

		230K			215K			20K		
		x	y	z	x	y	z	x	y	z
2Mn1	2a 000									
4Mn2		0.013(2)	1/3	0	0.0218(5)	1/3	0	0.041(4)	1/7	0
4Mn3	4g xy0							-0.070(6)	2/7	0
4Mn4								0.072(5)	3/7	0
2Ga1	2b 00 1/2									
4Ga2		0.0015(9)	1/3	1/2	0.0051	1/3	1/2	0.009	1/7	1/2
4Ga3	4g xy0							0.026(2)	2/7	1/2
4Ga4								0.062(1)	3/7	1/2
4Ni1	4f 1/2 0z			1/4			1/4			1/4
8Ni2		0.4930	1/3	1/4	0.4870(1)	1/3	1/4	0.476(1)	1/7	1/4
8Ni3	8h xyz							0.549(1)	2/7	1/4
8Ni4								0.433(1)	3/7	1/4

The crystal structure of the martensitic phase in Ni-Mn-Ga strongly depends on composition, temperature and internal stresses. The lattice parameters of the martensite phases are reported in orthorhombic coordinates in which the axes are parallel to the diagonal

directions of the cubic coordinates as well as in the original cubic coordinates. The former approach is convenient in the description of the crystal lattice modulation as a long-period superstructure, whereas the latter is more practical for a simple description of the strain values induced by stress or magnetic field (Soderberg et al 2005). When applying the cubic coordinate system, the modulated structures 5M and 7M have a lattice parameter ratio $c/a < 1$ and in the non-modulated tetragonal T martensite $c/a > 1$.

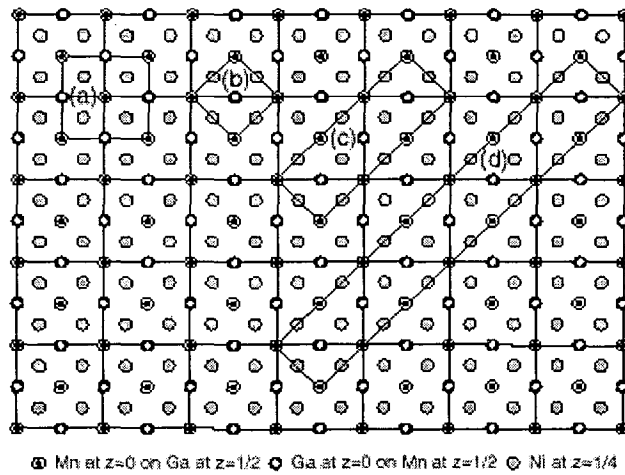


Fig 2.16: Atomic arrangement and correlation of the different crystal structures for Ni-Mn-Ga alloys (a) Cubic $L2_1$, (b) tetragonal martensite, (c) and (d) the 5 and 7 layered martensite 5M and 7M structures respectively (Brown et al 2002)

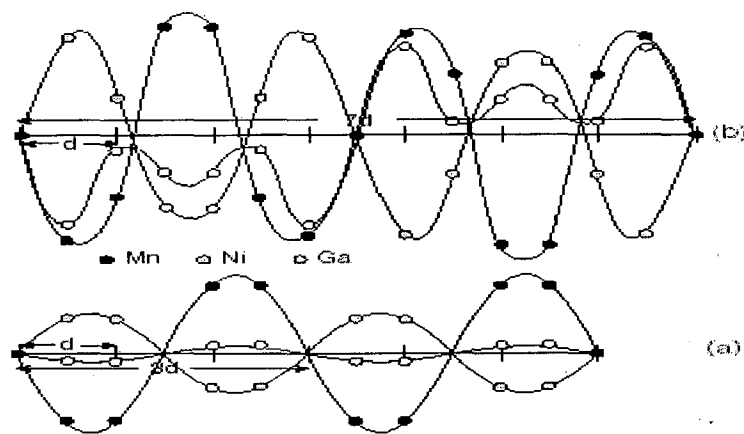


Fig 2.17: Displacements parallel to the a_{ortho} of the atoms in successive $(010)_{ortho}$ for (a) 5M and (b) 7M modulations (Brown et al 2007)

The various martensite phases are normally described with the crystallographic axes as defined above. However, analysis of experimental data may be performed in a common set of axes in the studies involving both martensite and parent phases. The parent phase coordinates are normally chosen for the purpose. The powder diffraction patterns of the martensite and parent phase in a common crystallographic coordinates for an $\text{Ni}_{52}\text{Mn}_{24}\text{Ga}_{24}$ single crystal alloy is shown in Fig 2.18.

The Rietveld refinements on the powder x ray diffraction data on a $\text{Ni}_{1.95}\text{Mn}_{1.19}\text{Ga}_{0.86}$ alloy has been carried out (Righi et al 2007). Due to similar x ray scattering factors for the Ni and Mn atoms, the fittings were carried out with formulae $\text{Ni}_2\text{Mn}_{1.15}\text{Ga}_{0.86}$. The fitting revealed a slight monoclinic distortion of the 5M orthorhombic lattice. The fittings show a presence of Mn atoms at Mn and Ga sites (Table 2.4).

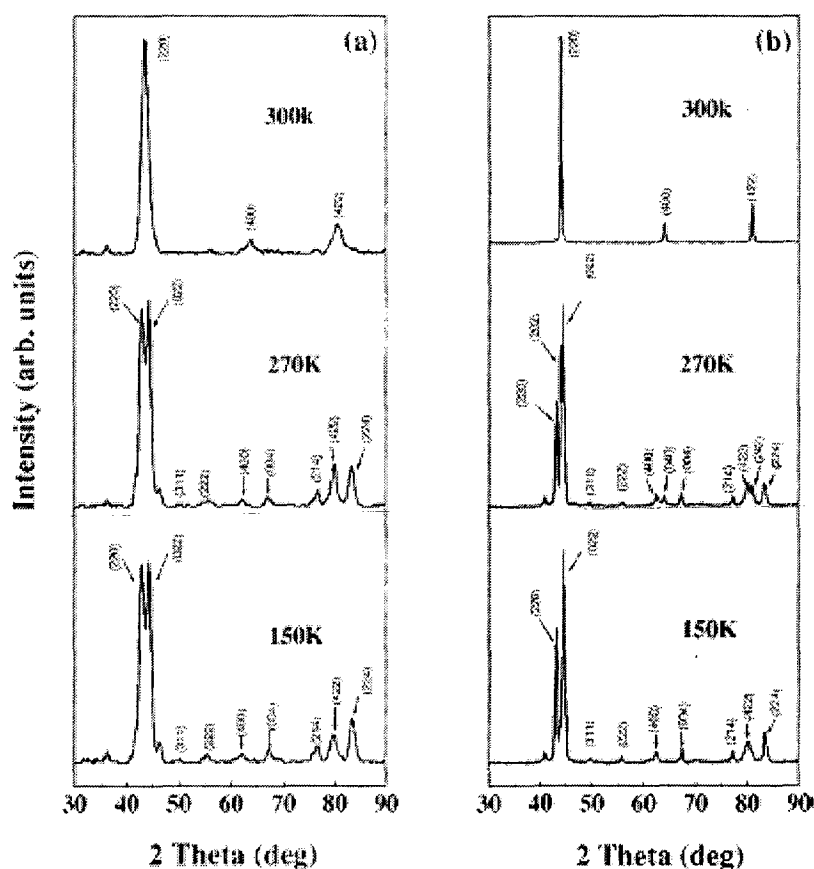


Fig 2.18: X-ray-diffraction patterns of the as-ground powder sample with $D, 50$ mm a) before annealing and b) after annealing at 500 °C for 10 h at various temperatures (Wang et al 2002).

Table 2.4: Atomic positions (x,y, z), ADP (U_{iso}), site occupancy factors (s.o.f.) and amplitudes (A_i) of the modulation function of the modulated structure of $Ni_2Mn_{1.15}Ga_{0.85}$ martensite (Righi et al 2007)

Name	Atom	Wyck.		x	y	z	s.o.f.	U_{iso}
Mn1	Mn	2a	A_1	0	0	0	1	0.008(6)
				0.070(8)	0	0		
			A_2	[0.066]				
				0.001(43)	0	0		
Ga1	Ga	2d	A_1	0	1/2	0	0.85(6)	0.010(5)
				0.070(7)	0	0		
			A_2	[0.070]				
				-0.005(35)	0	0		
Mn2	Mn	2d	A_1	0	1/2	0	0.15(5)	0.010(5)
				0.070(7)	0	0		
			A_2	[0.070]				
				-0.005(35)	0	0		
Ni1	Ni	4h	A_1	1/2	1/4	0	1	0.008(4)
				0.064(6)	0	0		
			A_2	[0.072]				
				0	0	0		

* The values in square brackets refer to the $A_2(x)$ amplitudes of the Ni_2MnGa martensitic modulated structure [21]. Although the fundamental structure in Ni_2MnGa has orthorhombic symmetry, a direct comparison is possible because the basic atomic coordinates of Mn, Ga and Ni are identical to those of the present monoclinic structure.

In addition to diffraction analyses, other techniques are also used for determining the actual site occupancy of the constituent atoms in the $L2_1$ lattice. The EXAFS technique has been employed to analyze the local atomic arrangements in the Ni_2MnGa alloys (Bhobe et al 2006).

The martensite transformations in off stoichiometric Ni_2MnGa alloys have been studied theoretically (Zayak and Entel 2006) as well as experimentally. The off stoichiometric $Ni_{52.6}Mn_{23.6}Ga_{23.8}$ alloy shows the transformation sequence to the stable martensite as $10M \leftrightarrow 14M \leftrightarrow 2M$ with transformation temperatures depending upon the magnetic field applied. The crystal structure of martensite is an important factor that affects the magnetic anisotropy and behaviour (Heczko et al 2003, Sozinov et al 2001, Sozinov et al 2002) as well as the mechanical properties of Ni-Mn-Ga alloys (Sozinov et al 2003, Koho et al 2003) and the chemical behaviour (Liu et al 2002, Liu et al 2003). The martensite structures, transformation temperatures and the Curie points have been systematized as functions of the average number of valence electrons per atom (e/a) (Chernenko 1999). Using a value of 10 for nickel from the outer electron shells as $3d^8 4s^2$, 7 for manganese from $3d^5 4s^2$ and 3 for gallium from $4s^2 4p^1$, the e/a ratio is given as

$$e/a = (10 * at\% Ni + 7 * at\% Mn + 3 * at\% Ga) / 100. \quad (2.1)$$

The crystal structure of the martensite phase in Ni-Mn-Ga strongly depends on composition, temperature and internal stresses. In line with the stability of the martensite structure being quoted in terms of the electron to atom ratio (e/a ratio) for conventional shape memory alloys, martensite transformation in Ni-Mn-Ga alloys is often related to e/a ratio. The relationship of e/a with martensite variants formed for different alloys has been generated in Fig 2.19 based on the available data (Table 2 in Soderberg 2004). The three structures have been marked as modulated 5 or 7 layered martensite or non modulated tetragonal structures marked as 5M, 7M or T in the figure. As the tetragonal martensite does not show any FMSM strains, the composition window for the suitable FMSM alloy is very narrow around e/a ratio of 7.7 corresponding to $\text{Ni}_{50}\text{Mn}_{30}\text{Ga}_{20}$ alloy.

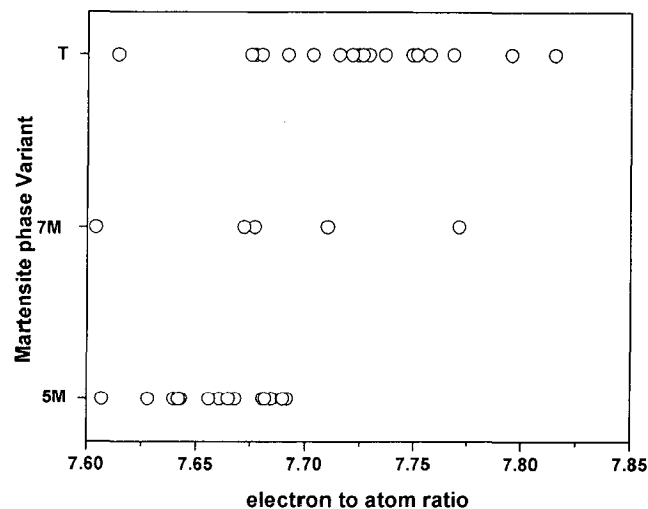


Fig 2.19: The room temperature martensite variants as a function of electron to atom ratios in Ni-Mn-Ga alloys. (5M, 7M and T denote the modulated 5M, 7M or non-modulated tetragonal martensite structures respectively (based on data by Soderberg 2004).

The martensite and intermartensite transformation temperature in single crystals of Ni and Mn rich Ni_2MnGa alloys have been determined as a function of quenching temperature by internal friction and Young's modulus measurements (Segui et al 2007). While the

martensite temperature was not effected with quenching temperatures. The intermartensite transformation temperatures were effected in a transformation sequence $L2_1 \Rightarrow 14M (+10O) \Rightarrow 2M (+ \text{residual } 14M)$.

Alloy composition modifies the structure properties such as martensite transformations mentioned above, as well as the physical properties. Being magnetic alloys, the magnetic proerties magnetization and magnetic anisotropy have been reported to be a function of composition (Murray et al 1998, Albertini et al 2002 and Jin et al 2002). Fig 2.20 shows a compilation of the reported modification in saturation magnetization as function of composition i.e in terms of electron to atom ratio for ternary Ni-Mn-Ga alloys.

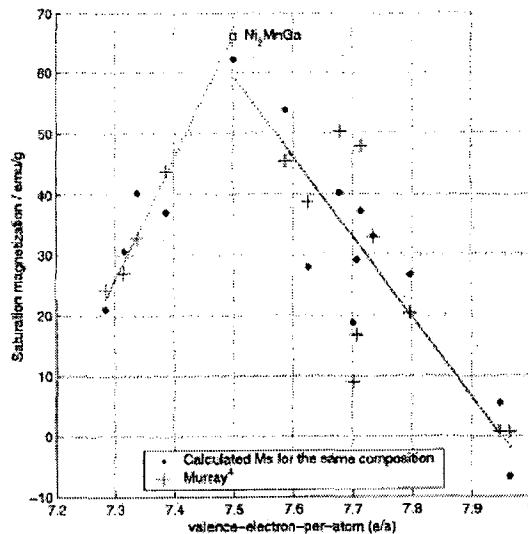


Fig. 2.20: Change in Saturation magnetization M_s with the average number of valence electrons per atom (e/a) shows a peak nearly at 7.5, the value of e/a for the stoichiometric composition Ni_2MnGa . • and + are calculated and experimental M_s for the same composition, respectively (Murray et al 1998).

The FMSM effect is related to easy de-twinning of the martensite phases with forces generated due to applied magnetic field. The twinning stress value reported for 5M and 7M is less than 5MPa and for tetragonal martensite this value is more than 15MPa. The 5M or 7M martensite structures therefore show a pronounced FMSM strains when compared to T martensite and are therefore desired.

The transformation temperature of the martensite phase in the Ni-Mn-Ga alloys depends strongly on the chemical composition: both the deviation from the stoichiometry and the doping with other elements. Increasing the Ni content and increasing the Mn/Ga ratio while keeping the Ni amount fixed, results in the higher martensite transformation temperature. In the stoichiometric Heusler Ni₂MnGa alloy, the martensitic transformation occurs at approximately 200 K leading to a modulated tetragonal martensite with lattice parameters $a = b = 0.5920$ nm and $c = 0.5566$ nm. Off stoichiometric Ni-Mn-Ga alloys however show other martensite structures such as 5 or 7 M structures in addition to the non-modulated tetragonal martensite (T). The type of martensite that forms during cooling depends on the composition of the alloy and the thermal stability of the different martensitic phases. The martensite transformation being a shear transformation, even the previous thermo mechanical history may influence the phase obtained. There seems to be a certain order according to which they emerge in the martensite transformation or change in the inter-martensitic transformations. The 'T' structure is the most stable one among the three martensite phases. The alloys transforming straight to the T martensite from the parent phase have typical transformation temperatures close or above the Curie point. The 5M structure transforms directly from the parent phase at lower temperatures close to the ambient one, while the 7M martensite appears directly from the parent phase only in a narrow temperature range below the Curie point. The transformation to the stable non-modulated martensite with $c/a > 1$ can also take place via the inter-martensite transformation such as $P \rightarrow M1 \rightarrow M2$, $P \rightarrow 8M$ (10M) $\rightarrow T$ or $P \rightarrow 5M \rightarrow 7M \rightarrow T$. Due to the change in the crystal structure, the inter-martensitic reaction seems to set the low service temperature for the magnetic shape memory effect.

In addition to the temperature being the thermodynamic variable in the phase diagrams, physical parameters like stresses, pressures, magnetic field etc may affect the phase transitions and a few studies are available on these aspects (e.g. Karaca et al 2007). The effect of these parameters is usually investigated through experimentally as well as analytically. Analysis of the data by fitting through neural networks has also been reported recently for certain shape memory alloys (Eyericioglu et al 2008).

The off-stoichiometric Ni₂MnGa alloys may show a range of other intermediate martensite phases. 10 or 14-layered martensite (similar to 5 or 7 layers of L1₀ in Ni-Al alloys) have been proposed either with long period stacking of $\{110\}_p$ or by latticed modulated by shuffling. Non modulated martensite phase has also been reported. The high twinning stresses of the order of 6-18 MPa do not allow this variant to show the FMSM phenomena and least data is available for this phase. Crystal structure of the ternary martensite phase strongly depends on composition and temperature. The Ms- Mf temperatures, T_c, *c/a* ratio etc. have been compiled within Ni₄₇₋₅₅Mn_{26.8-33.1}Ga_{19.1-22.1} with martensite structure at room temperature as 5M, 7M or NM. Inter-Martensite Transformation (IMT) reversible with either temperature or magnetic field through 10M → 14M → 2M (L1₀) have been noticed. The martensite transformation kinetics is a function of temperature, strain and the magnetic field applied. The martensite transformation temperatures increase with increase in applied magnetic field, indicating that the magnetic energy helps in martensite transformations. Variations in Ms with applied field H has been estimated with the modified Clausius-Clapeyron equation and are in good agreement with the experimental observations.

2.5 QUATERNARY ADDITIONS

As is clear from the foregoing information, conversion of different variants of martensite leads to the FMSM properties. The maximized magnetostrictive strain is obtainable if the single crystal of the precursor phase is available. In case of isotropic polycrystalline material, the FMSM strains achieved are considerably reduced. Besides polycrystalline alloys are brittle and their mechanical properties are dependent on the microstructure of the alloys. While ternary alloys have been investigated in details, the actual technological compositions are expected to be more complex alloy systems with ingredients added for specific benefits. The alloy development for Ni-Mn-Ga alloys on these lines is already thought about.

Table 2.2 indicates that the Heusler alloys X₂YZ are formed with X as a transition element Fe, Co, Ni or Cu, Y as Mn and Z as tri-valent element such as Ga or Al. Being iso-

structural with Ni₂MnGa alloys, it is expected that the elements would be soluble in the Ni₂MnGa structure.

The additions of Fe and Co have been made in Ni-Mn-Ga alloys (Khovailo et al2003). Alloys with minor additions of Fe and Co replacing either Ni or Mn in Ni_{2.16}Mn_{0.84}Ga compositions were characterized for their magnetization and the martensite and Curie transition temperatures. The Fe/Co replacements for Ni reduce the e/a ratios and accordingly the martensite temperatures fell (Fig 2.21), the Curie temperatures however with additions increased in this report. The Fe additions are reported to improve the much needed ductility in the Ni-Mn-Ga alloys (Xu et al 2006). As increase in both Curie temperature and martensite temperature is desirable from the application point of view, optimal quantities of the additions needs to be explored.

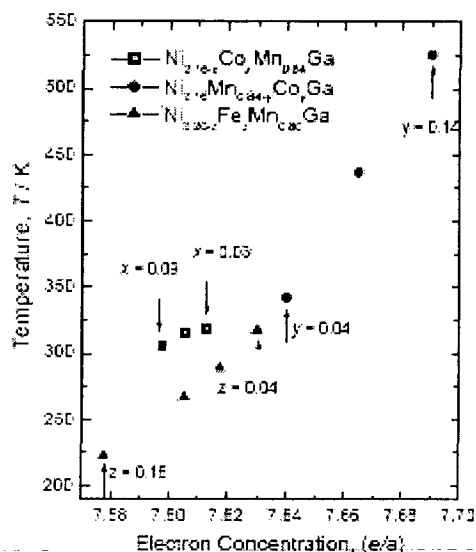


Fig 2.21: Dependence of martensite transformation temperature on e/a ratio for Fe/Co substituted Ni-Mn-Ga alloys (Khovailo et al 2003).

The trace additions of Fe in Ni-Mn-Ga alloys have been explored for site occupancy using Mössbauer spectroscopy (Mitros et al 1987). The Mossbaeur spectrum obtained is shown in Fig 2.22 The presence of Fe was possible at Ni, Mn or Ga sites with values of the magnetic hyperfine field of Fe at the Ni, Mn, and Ga sites at room temperature as 86(5) kOe, 146(5) kOe, and 145(5) kOe respectively.

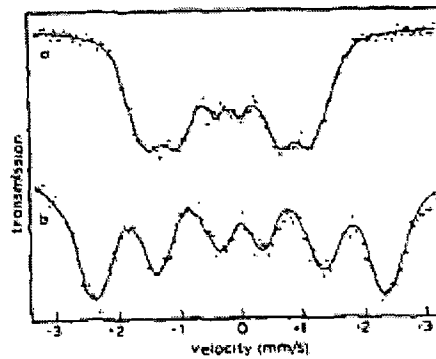


Fig 2.22: Room temperature Mössbauer spectra of a) $\text{Ni}_{2-x}\text{Fe}_x\text{MnGa}$ and b) $\text{Ni}_2\text{Mn}_{1-x}\text{Fe}_x\text{Ga}$ (Mitros et al 1987).

The rare earth additions to transition element alloy systems such as Nd-Fe-B and Sm-Co alloys are reported to improve the magneto-crystalline anisotropy via 3d-4f electron coupling (Stmat 1988). The solubility of the rare earths in Heusler alloys is however low and small amounts of rare earths have been reported to be dissolved in the Heusler alloys at about 1 atom % gross addition levels. The studies on $\text{Ni}_{50}\text{Mn}_{29}\text{Ga}_{21-x}\text{Dy}_x$ (at.%; $x = 0, 0.1, 0.5, 1, 2$) revealed a 7M phase formation for Dy containing alloy and a two stage martensite transformation (Gao et al 2006). No Dy was found in matrix phase up to $x=1$ and alloys with $x=2$ where Dy was present in matrix phase did not show any different trend. The alloys $\text{Ni}_{50}\text{Mn}_{29}\text{Ga}_{21-x}\text{Gd}_x$ ($x = 0, 0.1, 0.5, 1, 2$) shows a change of 5m martensite to 7M martensite beyond $x=0.5$ (Gao et al 2008). The Curie transition and the martensite transformation overlapped in these alloys and compositions with T_c higher or lower than the martensite transformation could be obtained. Ni-Mn-Ga alloys with other rare earth such as Y- additions (Cai et al 2007) and Tb- additions (Leonowicz et al 2006) are also reported. The addition of Sm has been reported to improve the ductility of the Ni-Mn-Ga alloys, the rare earth addition at grain boundary causes disorder at the grain boundary thereby the otherwise poor ductility of the ordered structure is improved. (Tschiya et al 2004).

2.6 EFFECT OF PROCESSING

Conversion/ reorientation of different variants of martensite leads to the FMSM properties. The maximized FMSM strain is usually obtained using single crystals of the precursor phase. Majority of the functional characterization for the Ni-Mn-Ga alloys viz measurement of the MFIS is reported on the single crystals of austenite phase. In case of isotropic poly crystalline material, the FMSM strains achieved are considerably reduced. Besides poly-crystalline alloys are brittle and their mechanical properties are dependent on the microstructure of the alloys. Similarly growing single crystals of long lengths is a cost sensitive process. With the advent of the micro-electronic mechanical system (MEMS) devices, the FMSM devices may need materials as thin films. Alternate processes to that of growing single crystals through conventional processes are therefore being studied both as thin films as well as in bulk forms. The reports of characterization on poly-crystals and studies on improvement of the functional properties such as ductility are therefore being carried out. $\text{Ni}_{54}\text{Mn}_{25}\text{Ga}_{21}$ alloys have been arc melted in the button form as well as in a faster cooled rod form (Li et al 2004). The XRD trace revealed the same phases under the two conditions; however faster cooling resulted in finer austenite grains as well as finer lamellae of the martensite on martensite transformation (Fig 2.23). Fig 2.24 shows the compressive stress strain curve of the two forms. The improved ductility behavior for the rod sample is attributed to the finer grain size. Melt texture in bulk alloys have been developed by solidifying Ni-Mn-Ga alloy in a hot ceramic mould with a copper chill plate (Porschke et al 2007). Thin film preparation techniques such as magnetron or di polar plasma sputtering, laser ablation etc have been employed for preparation of the Ni-Mn-Ga alloys (Liu et al 2008, Girard et al 2008). The thin film grown in these techniques may be single layer or composite polycrystalline Ni-Mn-Ga (Kohl et al 2006). $\text{Ni}_{51.4}\text{Mn}_{28.3}\text{Ga}_{20.3}$ thin films have shown substantial temperature vs. film thickness dependencies of interatomic spacing measured in the direction of the film normal in the range of 25–200 °C and 0.1–5 μm , respectively (Besseghini et al 2008) Rapidly quenched $\text{Ni}_{51}\text{Mn}_{28}\text{Ga}_{21}$ alloy ribbons have shown martensite transformation temperatures around room temperatures and below Curie transitions and hence a field induced detwinning was possible at low fields of 2 KOe (Gutierrez et al 2006). Melt spun $\text{Ni}_{52.5}\text{Mn}_{24.5}\text{Ga}_{23}$ alloys have shown a mixed phase structure of austenite and martensite at room temperatures (Panda et al 2008).

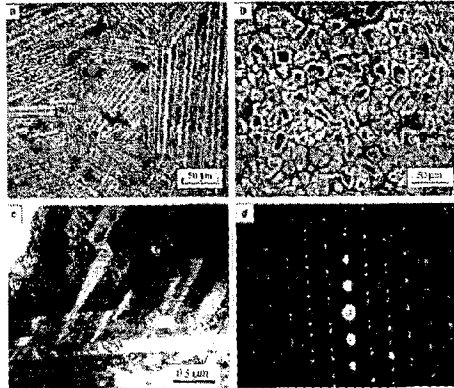


Fig 2.23: Microstructures of the polycrystalline Ni₅₄ Mn₂₅ Ga₂₁ alloys (a)optical micrograph for the button sample,(b)optical micrograph,(c)TEM bright field image and (d)the SAED pattern for the rod sample at 20° C. (Li et 2004)

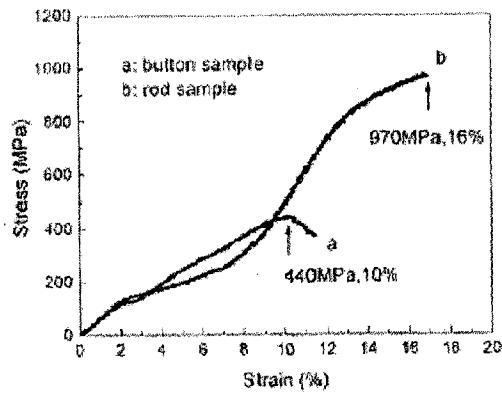


Fig 2.24: Compressive stress strain curves of the polycrystalline Ni₅₄ Mn₂₅ Ga₂₁ for (a) button and (b) rod samples (Li et 2004).

2.7 FORMULATION OF PROBLEM

The foregoing information reveal that the ternary Ni-Mn-Ga alloys have been studied in great details for their crystal structures, atomic ordering and various other aspects and their affect on the functional properties. Considering the limitation of the Ni-Mn-Ga alloys especially in terms of further improvement in their operating temperatures and ductility, alternatives are required to be explored. These alternatives range from alternate Heulser alloy systems like Ni-Fe-Ga, Co-Mn-Al etc. or the quaternary alloying additions within Ni-Mn-Ga systems to improve one or more functional properties. More often than not, these studies are limited to show the potential but the scientific details about the underlying parameters such as atomic structure, atomic spacing or ordering are often unexplored.

Commercial alloy development programs normally require studies on multi-component systems based on binary or ternary alloy system in which components are added in trace or larger amounts for improving one or the other property. Details about quaternary or more complex systems in case of Heusler alloy based FMSM alloys are very limited. Therefore further scope of research exists in the areas such as:

- Identification of alternate ferromagnetic Heusler type structures and their characterization for ferromagnetic shape memory effects
- Modification of the ternary Ni-Mn-Ga alloys with quaternary additions in order to improve the functional properties of the ternary alloys such as improved transformation temperatures, ductility etc.
- Study the role of processing parameters such as heat-treatment and cooling rates on the homogeneity and ordered structures of the alloys and thereby understand their effect on the functional properties
- Generate process-composition –property maps for selection of the alloys for specific applications in given environment

In view of the importance of quaternary FMSM alloys, it is proposed to carry out structure property correlations in quaternary alloys based on ternary Ni-Mn-Ga alloys. Considering the compositional optimizations already carried out in ternary alloys for FMSM effect, an optimized composition $\text{Ni}_{50}\text{Mn}_{30}\text{Ga}_{20}$ (NMG) has been selected as a base for

quaternary alloy composition. The following addition groups were identified for the investigations and their relative position *vis-à-vis* the ternary components in the periodic table are shown in Fig 2.25:

- I. Transition element addition like Fe or Co to substitute partially for Ni or Mn in NMG
- II. Trivalent element like Al/B to substitute partially for Ga in NMG
- III. Other elements different from group I and II, additions of a light rare earth Sm and a heavy rare earth Dy to substitute partially for Ga. .

With the Mn-rich Ni-Mn-Ga compositions are reported with optimal combination of properties, the few available literature studies reports effects of small quaternary additions in Ni-Mn-Ga alloys. In view of the reports that ternary Heusler alloys other than Ni-Mn-Ga system also have potential for the FMSM applications, it is possible that the Ni-Mn-Ga alloys with quaternary additions may form potential Heusler alloys as a mixture of two Heusler compositions or with an intermediate composition. For example Ni-Mn-Ga alloys with Fe addition may form Heusler alloys between the known Ni-Mn-Ga and Ni-Fe-Ga systems. Small as well as reasonably large additions of the quaternary additions have therefore been planned for structure property correlations in polycrystalline quaternary alloys.

As is evident from literature, the properties of the alloys are dependent on both the alloy phase structure and the microstructure. These alloys are essentially intermetallic alloys and may require improved mechanical and environmental stability through controlled microstructures. The primary functional property viz. magnetic field induced strain however is mainly dependent on the alloy structure defining its physical properties. The magnetic and structural transformation temperatures define the possible operating temperatures of the FMSM alloys. While the lattice parameters like c/a ratios would give the values of the maximum attainable magnetic field induced strains, their actual realization would be dependent on ability of the magnetic fields to cause the detwinning of the martensite twins. These parameters viz. magnetic and structural transformation temperature and the specific magnetization of the alloys are therefore proposed to be investigated as primary characterization parameters of the alloys.

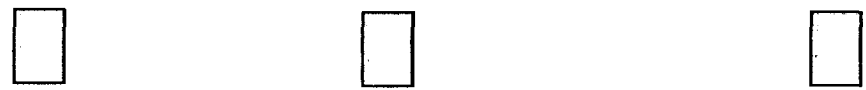
hydrogen 1 H 1.0079																	helium 2 He 4.0026				
lithium 3 Li 6.941	beryllium 4 Be 9.0122															boron 5 B 10.811	carbon 6 C 12.011	nitrogen 7 N 14.007	oxygen 8 O 15.999	fluorine 9 F 18.998	neon 10 Ne 20.180
sodium 11 Na 22.990	magnesium 12 Mg 24.305															aluminum 13 Al 26.982	silicon 14 Si 28.086	phosphorus 15 P 30.974	sulfur 16 S 32.065	chlorine 17 Cl 35.453	argon 18 Ar 39.948
potassium 19 K 39.098	calcium 20 Ca 40.078	scandium 21 Sc 44.956	titanium 22 Ti 47.867	vanadium 23 V 50.942	chromium 24 Cr 51.996	manganese 25 Mn 54.938	iron 26 Fe 55.845	cobalt 27 Co 58.933	nickel 28 Ni 58.693	copper 29 Cu 63.546	zinc 30 Zn 65.39	gallium 31 Ga 69.723	germanium 32 Ge 72.61	arsenic 33 As 74.922	selecnium 34 Se 78.96	bromine 35 Br 79.904	krypton 36 Kr 83.80				
rubidium 37 Rb 85.468	strontium 38 Sr 87.62	yttrium 39 Y 88.906	zirconium 40 Zr 91.224	niobium 41 Nb 92.906	molybdenum 42 Mo 95.94	technetium 43 Tc 98	ruthenium 44 Ru 101.07	rhodium 45 Rh 102.91	palladium 46 Pd 106.42	silver 47 Ag 107.87	cadmium 48 Cd 112.41	indium 49 In 114.82	tin 50 Sn 118.71	antimony 51 Sb 121.76	tellurium 52 Te 127.60	iodine 53 I 126.90	xenon 54 Xe 131.29				
cesium 55 Cs 132.91	barium 56 Ba 137.33	* 57-70	lanthanum 57 La 138.91	hafnium 58 Hf 178.49	tantalum 59 Ta 180.95	wolfram 60 W 183.84	reuterfordium 61 Re 186.21	osmium 62 Os 190.23	iridium 63 Ir 192.22	platinum 64 Pt 195.08	gold 65 Au 196.97	mercury 66 Hg 200.59	thallium 67 Tl 204.38	lead 68 Pb 207.2	bismuth 69 Bi 208.98	polonium 70 Po 209	astatine 71 At 210	radon 72 Rn 222			
francium 87 Fr 223	radium 88 Ra 226	* * *	actinium 89 Ac 227	rutherfordium 103 Rf 261	bohrium 104 Bh 264	hassium 105 Hs 269	meitnerium 106 Mt 268	darmstadtium 107 Ds 271	roentgenium 108 Rg 272	copernicium 109 Cn 285	nihonium 110 Nh 286	flerovium 111 Fl 289	tennessine 112 Ts 289	unbinilium 113 Uub 288	unquadrium 114 Uuq 289						

* Lanthanide series

lanthanum 57 La 138.91	cerium 58 Ce 140.12	praseodymium 59 Pr 140.91	neodymium 60 Nd 144.24	promethium 61 Pm 145	samarium 62 Sm 150.36	europium 63 Eu 151.96	gadolinium 64 Gd 157.25	terbium 65 Tb 158.93	dysprosium 66 Dy 162.50	holmium 67 Ho 164.93	erbium 68 Er 167.26	thulium 69 Tm 168.93	ytterbium 70 Yb 173.04
---------------------------------	------------------------------	------------------------------------	---------------------------------	-------------------------------	--------------------------------	--------------------------------	----------------------------------	-------------------------------	----------------------------------	-------------------------------	------------------------------	-------------------------------	---------------------------------

** Actinide series

actinium 89 Ac 227	thorium 90 Th 232.04	protactinium 91 Pa 231.04	uranium 92 U 238.03	neptunium 93 Np 237	plutonium 94 Pu 244	americium 95 Am 243	curium 96 Cm 247	berkelium 97 Bk 247	californium 98 Cf 251	eskeium 99 Es 252	fermium 100 Fm 257	mendelevium 101 Md 258	nobelium 102 No 259
-----------------------------	-------------------------------	------------------------------------	------------------------------	------------------------------	------------------------------	------------------------------	---------------------------	------------------------------	--------------------------------	----------------------------	-----------------------------	---------------------------------	------------------------------



Ingredients of base composition Substitutions for Ni/Mn Substitutions for Ga based on valancy /size

Fig 2.25: The basic ingredient of the Ni-Mn-Ga alloys and quaternary addition elements planned for the study.

A systematic investigation of the modifications in physical properties of the ferromagnetic shape memory alloys is therefore proposed to be studied in this study. Base composition Ni₅₀Mn₃₀Ga₂₀ has been modified during the course of the study with different quaternary additions thus modifying the alloy structure and/ or atomic placements in the structure. The scope of the work thus consists of :

- Preparation of alloys with quaternary additions of the groups defined above in a base composition Ni₅₀Mn₃₀Ga₂₀ (at %). This includes the melting of alloys and their heat-treatment as well as use of Rapid Solidification as an alternative processing technique.

- Structural characterization of the alloys using microscopic , spectroscopic and diffraction techniques to understand the crystal structure information
- Characterization of physical properties viz. thermal and magnetic characterization of the alloys prepared and
- Development of the relationship between structural information and the properties obtained for an understanding of the role of the quaternary additions thereby paving way for an effective alloy development beyond ternary alloys.

EXPERIMENTAL METHODS

The Heusler alloys are ordered alloys and therefore the alloy preparation techniques is expected to modify the underlying phase structure and/ or the level of ordering. These processing will therefore affect the properties as well. The details of the experimental techniques employed in carrying out the present work are described in this chapter. The characterization of the alloys has been done for their structure as well as the physical properties such as magnetic, thermal and thermo-magnetic properties etc. The experimental procedures and techniques adopted for the thesis work can be broadly divided into the following:

Alloy preparation and processing:

- (i) Alloy selection and preparation of the alloys by vacuum arc melting
- (ii) Preparation of bulk alloy specimens & heat-treatment of the samples; and preparation of ribbon specimens by rapid solidification

Alloy Characterization:

- (iii) Characterization for chemistry, phase structure and microstructure using microscopic, diffraction and spectroscopic techniques.
- (iv) Physical properties *viz.* magnetic and / or thermal characterization of the alloys for identifying phase transformation temperatures and characteristics using thermal analysis, magnetic and thermo-magnetic measurements
- (v) Mechanical properties

The above methods are described in detail in subsequent sections of the chapter

3.1 ALLOY PREPARATION

3.1.1 Selection of Raw Materials and Alloy Compositions

The basic raw materials used for preparation of the alloys in this study are transition elements Ni, Fe, Co and Mn; trivalent elements Ga, Al and B. The boron lumps of 99.5 % purity were used , whereas all other ingredients were of purity better than 99.9%.

Quaternary additions made to a $\text{Ni}_{50}\text{Mn}_{30}\text{Ga}_{20}$ base composition have been classified in three groups. A range of compositions were selected so as to ensure the dissolution of the additions within the Heusler phase avoiding secondary phases in order to determine the role of the additions on the property modifications in the phase. Group I alloys are the alloys with addition of transition elements Fe or Co. Initial alloys were made with Fe/ Co substituting for Ni. Based on the understanding developed subsequent alloys were made with formulae substitutions for Mn and Ni. The group –II alloys were prepared initially with Al replacing Ga. A set of alloys were later prepared based on the understanding developed with the initial alloy. A varied amount of both Al and B replacements were made for Ga in these alloys. Eleven quaternary alloys in addition to the base ternary alloy $\text{Ni}_{50}\text{Mn}_{30}\text{Ga}_{20}$ were prepared and investigated during the course of this study. Table 3.1 shows the nominal compositions of the alloys planned in the study and their designation followed in this report. The element being replaced and its content after replacement are given first followed by the element(s) replaced and their content. Thus the alloy designation Ga15Al4B1 signifies an alloy with 15 atom % Ga with 4atom %Al and 1atom %B with other constituents Ni and Mn remaining at 50 and 30 at% in the base composition $\text{Ni}_{50}\text{Mn}_{30}\text{Ga}_{20}$. The base composition is designated as NMG.

3.1.2 Alloy Melting

The charges for melting were first weighed according to the nominal composition of each alloy. The elemental losses were ascertained by trial melts. Loss of Mn being the lowest boiling point element was noticed in these trials and accordingly an excess of 3 % Mn was added to achieve the aimed compositions. Alloy charges were prepared for 50g batch. A vacuum arc melting furnace (M/s Vacuum Techniques, Bangalore make, Fig 3.1) was employed for melting of the alloys. The furnace has a facility of a water-cooled copper cup with five mould cavities each with 80mm diameter and 10-12 mm depth. Elemental charges were loaded into one of the mould cavity. A pre-melted Ni-Mn-Ga alloy button was also separately placed in another cavity and was used to strike the initial arc. The chamber was evacuated to the vacuum of the order of 10^{-5} torr, followed by back filling with argon pressure to 200 mm. The arc was struck with starting Ni-Mn-Ga alloy button kept for the purpose and then moved over to the alloy charge and melting was carried out moving the electrode over the entire button area slowly ensuring complete melting. The typical melting parameters were 40 V and 200-300A current. Repeated melting of the button flipping the same each time was performed to ensure chemical macro-homogeneity.

Table 3.1: Nominal compositions of the alloys prepared for the present study.

Group	Alloy Designation	Atom %				Weight %			
		Ni	Mn	Ga	Additive	Ni	Mn	Ga	Additive
*	NMG	50	30	20	Nil				Nil
I	Ni40Fe10	40	30	20	10Fe	39.47	27.70	23.44	9.39Fe
	Ni40Co10	40	30	20	10Co	39.26	27.56	23.32	9.86Co
	Mn27.5Fe2.5	50	27.5	20	2.5Fe	49.08	25.26	23.32	2.34Fe
	Mn25Fe5	50	25	20	5Fe	49.06	22.96	23.31	4.67Fe
	Mn15Fe15	50	15	20	15Fe	48.99	13.75	23.28	13.98Fe
	Ni45Fe5	45	30	20	5Fe	44.29	27.64	23.38	4.68Fe
II	Ga15Al15	50	30	15	5Al	50.92	28.59	18.15	2.34Al
	Ga15Al4B1	50	30	15	4Al,1B	51.06	28.67	18.20	1.88Al 0.19B
	Ga15Al1B4	50	30	15	1Al,4B	51.50	28.92	18.35	0.47Al 0.76B
III	Ga19Sm1	50	30	19	1Sm	48.44	27.21	21.87	2.48Sm
	Ga19Dy1	50	30	19	1Dy	48.35	27.15	21.82	2.68Dy

*Base ternary alloy composition

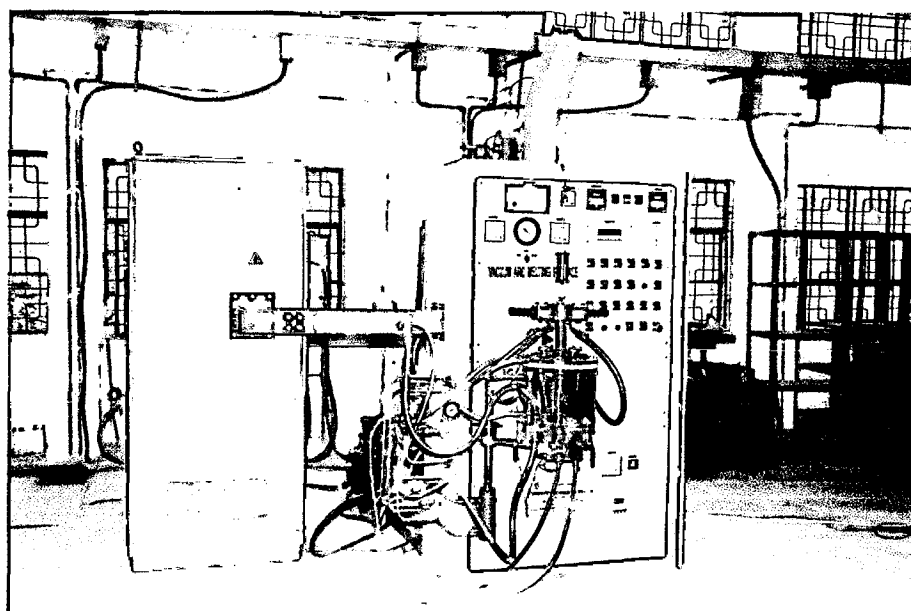


Fig 3.1: The Vacuum Arc Melting furnace

3.1.3 Alloy Homogenization and Bulk Alloy Preparation

The as melted alloy buttons so prepared were heat-treated suitably for homogenization. The alloy buttons were cut into small pieces using a low speed table top saw (ISOMET, Buhler) for heat treatment. Long duration heat-treatments on vacuum heat-treatment furnaces were thought unviable. The alloy homogenization being controlled by diffusion processes, initial heat-treatments were carried out at relatively high temperature with heat-treatment durations of a few hours i.e. 1273 K for 3 hrs in a vacuum furnace and gas quenched. The alloys Ni₄₀Fe₁₀, Ni₄₀Co₁₀ and Ga₁₅Al₅ alloys have been prepared with this heat-treatment to be referred as heat treatment 1.

It was realized that while high temperature treatment may hasten atomic diffusion, the ordered structure of the alloy may be adversely affected at higher temperature (Segui et al 2007), the heat-treatment procedure was modified accordingly for the latter alloys. Remaining alloy compositions were heat-treated for 1273 K for 72 h followed by 1073K for 48 h and then water quenched to ensure both diffusion of the elemental species and a lower temperature ordering. The first type of treatment was carried out directly in a vacuum heat-treatment furnace (BREW Furnace, USA) under high vacuum (10^{-5} mbar) and gas quenched within the furnace by circulating high pressure argon on completion of the heat-treatment period. This heat-treatment called heat treatment 2, was carried out in sealed evacuated ampoules. The cut specimens were then vacuum sealed to a high vacuum ($<10^{-5}$ mbar) in quartz ampoules and heat treated for the time/ temperature combinations in muffle furnaces for long duration heat treatments followed by water quenching of the ampoules.

3.1.4 Rapid Quenching

Group II alloy compositions with Al/ B additions are normally reported as easy glass forming compositions. In addition to the bulk alloy preparation through standard methods, these alloys have been additionally processed through the rapid quenching route also to study the effect of rapid quenching and the metastable phases produced. Master alloy were prepared by melting the constituent elements in vacuum arc melting furnace in 50g scale as per the melting procedure described above. Small pieces of the master alloys of the size 3-5mm were rapidly quenched to form ribbon specimens in a high vacuum melt spinner (Fig 3.2). The

melt spinner unit has 300mm diameter copper wheel capable to rotate at varied rpm ranging from about 300 rpm to 3000rpm (corresponding to linear wheel speeds of 5- 47 m/s). The alloys were re-melted in quartz crucibles and to ensure contamination-free re-melting, rapid induction heating power was applied using an RF induction power supply of rating 15kW, 400-500kHz. The metal pieces were placed in a quartz crucible (18mm OD, 16 mm ID and ~15cm length) with an elliptical slit of width 1.15 mm and length 10 mm. The crucible was put into the copper induction coil to melt the master alloys. Inductive power was applied after creation of high vacuum ($<10^{-5}$ mbar) and back filling with argon to 600mm pressure. The rapid quenching rates are complex function of various parameters such melt ejection rates (controlled by ejection pressures, nozzle size, fluidity of the melt (superheat etc) and the spinning rates viz. wheel speed. For comparative studies, alloys were melt-spun with wheel rotating at 2000 rpm (32 m/s. Ejection pressures of 5 psi (~ 0.35 bar) were applied to eject the melts onto the rotating copper wheel to obtain the ribbon samples.

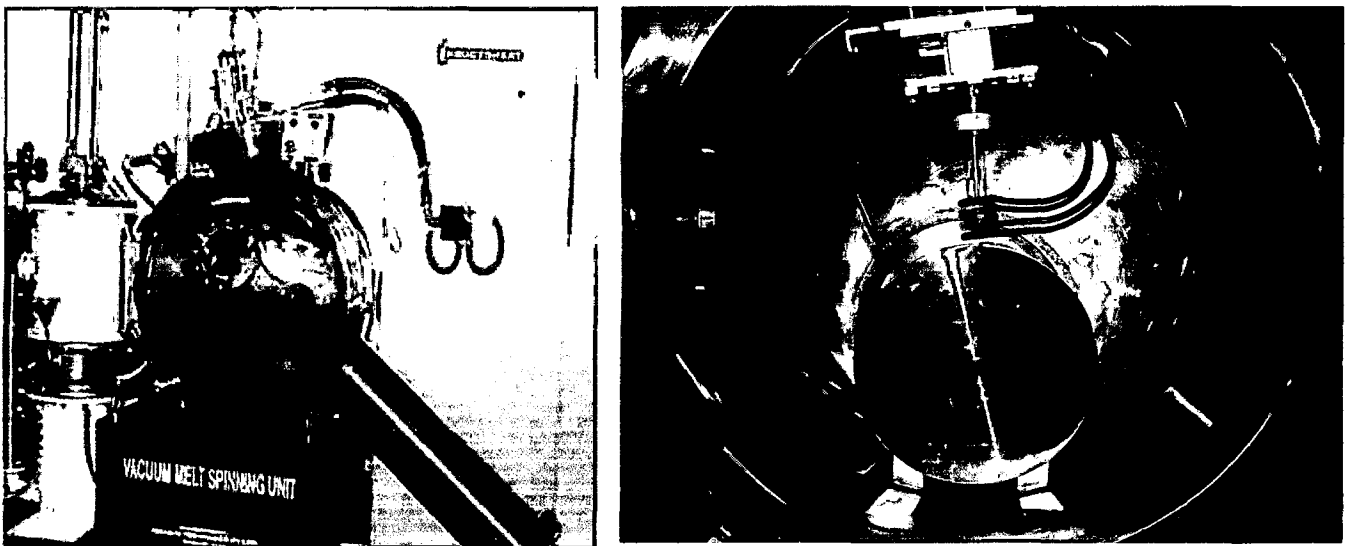


Fig. 3.2: The vacuum melt spinning unit and the experimental set up inside

3.2 COMPOSITIONAL ANALYSIS

Elemental compositions have been determined for the bulk alloys using conventional techniques and for the phases using wave length or energy dispersive x-ray analysis attached to the electron microscopes. The latter techniques are described along with the electron

microscopy in later parts of the chapter. A range of techniques are available for determining chemistry of the alloys (Thomas 1999). The instrumental techniques are more common for faster analysis of the various elements present in the system. Though common for small additions analysis, with proper standards and verification, these techniques can be adapted for bulk analysis of principal constituents also. The bulk alloys were analyzed using Inductively Coupled Plasma Optical Emission Spectroscopy (ICP-OES) for the constituent elements of the alloys. The principle and experimental details of ICP-OES technique are covered in detail in literature (for example Wang 2005). The ICP-OES is a multi-elemental technique that uses extremely hot plasma source to excite atoms to the point that they emit wave length specific photons of characteristic of a particular element. The number of photons produced is directly related to the concentration of elements.

For the analysis, 1gm of sample was dissolved completely in 20 ml of an acid mix (15ml of H₂SO₄, 5ml of HNO₃) by gently heating the solution in 400ml beaker till complete digestion of the solids. 2ml of HF was added to the solution and again heated. After cooling the solution to room temperature, it was diluted to make it a 100ml solution. Out of this, 10 ml of solution was taken out and again diluted to 100ml solution. This solution was used for the analysis. The intensity values were obtained from associated software and the elemental percentages calculated.

3.3 STRUCTURAL CHARACTERISATION

Structural characterization of alloys is carried out using a range of techniques (Barrett and Massalski 1980). The ultimate properties of the materials are dependent on the crystal structure and microstructures of the materials. The techniques like x ray radiography and Mössbauer spectroscopy have been employed to understand crystal structure whereas optical and electron microscopy techniques are used for microscopic examination. The x-ray diffraction has been employed as a primary tool to characterize the crystal structure of the room temperature phase in as-cast as well as annealed alloys. Mössbauer spectroscopy has been employed in case of Fe containing alloys to study the ⁵⁷Fe-spectrum from various Fe containing phases present in our alloys. In addition to conventional optical microscopy, Scanning Electron Microscopy (SEM) was used for studying the micro-structural features. The finer details of the

rapidly quenched ribbons were investigated with the Transmission Electron Microscopy (TEM). The electron microscopy units had Energy Dispersive Analysis of X-rays (EDAX) unit attached for the elemental analysis. Details of these methods are described here.

3.3.1 X-Ray Diffraction

The x-ray diffraction is based on the Bragg's law of diffraction describing conditions for constructive interference of x-rays scattered from atomic planes of a crystal. The condition for constructive interference is given by the Braggs' formulae $2d \sin\theta = n\lambda$, where, λ is the wavelength of X-rays, d is the lattice spacing, n is the order of diffraction and θ is the glancing angle of x-rays. The lattice spacing d is related to the $(h k l)$ indices of the planes and the dimension of the unit cells (Cullity 1978). The different techniques for diffraction studies involve keeping one of three variables d , θ and λ constant and varying one of the remaining as a function of the other.

The diffractometer technique uses monochromatic x-rays (fixed λ) and varies θ to study constructive interference from various d -spacing of the specimen crystal. A Phillips x ray diffractometer model PW 1320 has been employed for the diffraction studies here and consists of three basic modules – an x-ray tube, specimen holder, a goniometer to count the diffracted x ray photons and an electronic circuit panel with an automatic recorder. The schematic diagram of the x-ray diffractometer is presented in Fig.3.3

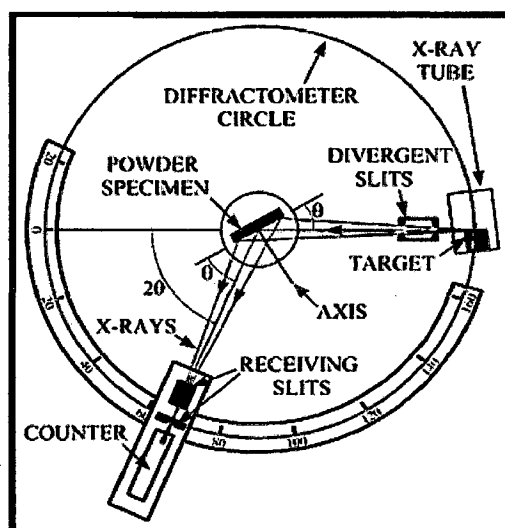


Fig 3.3: Schematic layout of the x ray diffraction techniques

A powdered specimen was uniformly spread on a flat plate supported on a table that can be rotated about an axis perpendicular to the plane of the drawing. The x-ray source was kept in line with focal spot on the target of the x-ray tube. Source also normal to the plane of drawing was therefore parallel to the diffractometer axis. X-rays diverging from the source were diffracted by the specimen to form a convergent diffracted beam coming to a focus at the receiving slit. The receiving slits and detector were supported on the carriage moving on diffraction circle in Fig 3.3. Detector was rotated about the axis and whose angular position 2θ readable on the graduated scale were logged into a computerized data-logger recording diffracted x ray counts for each angular position.. The mechanical coupling within the system ensured that a rotation of the detector through $2x$ degrees is automatically accompanied by the rotation of the specimen through x degrees. Obtained diffractograms *viz* plots of normalized diffracted beam intensities with angle 2θ were analyzed and indexed to understand the crystal structure(s) in the specimens.

X-ray diffractograms so obtained were indexed using the available literature information on ternary and quaternary Ni-Mn-Ga alloys. These diffractograms corresponded to the cubic and martensite phases similar to those obtained earlier. The high temperature austenite phase corresponded to cubic phase and has been indexed accordingly. The non-modulated tetragonal martensite has been indexed in tetragonal coordinates, the modulated variants of the martensite phases are indexed in either coordinates. We have followed the pattern followed by Wang et al 2002 indexing modulated martensite phases in parent phase coordinates.

3.3.2 Optical Microscopy

Optical microscopy has been used for preliminary examination of all the alloys in as-cast and heat-treated condition with detailed examination through electron microscopy described later.. The samples were prepared using standard metallographic procedure. A thin sample was cut from the bulk sample using an ISOMET cutter. The sample was then mounted on the bakelite disc by hot pressing of the bakelite powder. The sample is mounted so that the plane and flat surface of the sample is exposed to the environment. The sample is then polished on grinding wheel and subsequently on emery papers graded from 1 to 6. The

final polishing is done on cloth polishing wheels to finally obtain a shining polished surface. The polished samples were etched using a waterless Kallings reagent (50% HCl + 50% Methanol+ 2-5g CuCl₂) normally used for Ni base alloys (Small-2008; Page technologies).

3.3.3 Scanning Electron Microscope (SEM)

Morphology and microstructures studies of the as-cast alloys, as well as the heat treated alloys have been examined using LEO 440i scanning electron microscope (SEM) with an OXFORD ISIS300 ultra-cool energy dispersive X-ray SiLi detector (EDAX) shown in Fig.3.4. The principle and application of the SEM are available in literature (Murr 1970, Goldstein and Yakowitz 1975). The microstructural details of the specimen is investigated using such microscopes using secondary or back scattered electrons (SE or BSE); and characteristic x-rays emerging out from specimen when finely focused electron beam strikes the specimen. The electron beam incident on the specimen is made to scan the surface under examination and hence the name 'Scanning Electron Microscope' (SEM) The information about the specimen surface generated through the SE/ BSE/ x-rays etc is collected point to point. While SE images are generally used for surface topography studies or to thus reveal the grain structures, BSE images show the atomic number contrast and thus reveal the phase contrasts in the samples. The EDAX analysis are used to understand the phase chemistry as the specific energy photons signify the elements and their respective counts the quantity of the specific element.

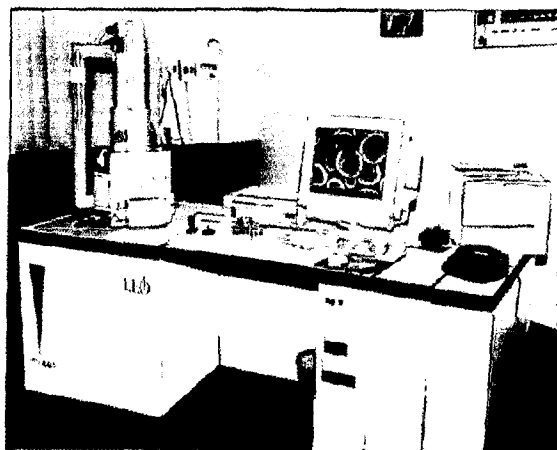


Fig. 3.4: The Scanning Electron Microscope

The general instrumentation is well described in published reports (Amelinckx et al 1997). The prime components of the equipment are the electron gun, the magnetic focusing lenses, the sample vacuum chamber and specimen stage and the electronics console containing the control panel, the power supplies and the scanning modules. The electron beam is produced by electron gun. The magnetic lenses concentrate the beam onto the area of interest. The beam is focused on the sample by a series of magnetic lenses. Each lens has an associated defining aperture that limits the divergence of the electron beam. The top lenses are called condenser lenses, and often are operated as a single lens. By increasing the current through the condenser lens, the focal length is decreased and the divergence increases. The beam next arrives at the objective lens-aperture combination. The objective lens does the ultimate focusing of the beam onto the surface of the sample. The sample is attached to a specimen stage that provides x- and y motion, as well as tilt with respect to the beam axis and rotation about an axis normal to the specimen's surface. A final "z" motion allows for adjustment of the distance between the final lens and the sample's surface. This distance is called the working distance. The working distance and the limiting aperture size determine the convergence angle. Typically the convergence angle is a few milli-radians and it can be decreased by using a smaller final aperture or by increasing the working distance. The smaller the convergence angle, gives large depth of focus.

The samples were mounted with thermoplastic resin (Bakelite) and polished down to ½ micron (with diamond polish) to a metallographic surface finish. The observations were carried out after ultrasonic cleaning of the sample. Majority of the micro-structural features were seen under back-scattered electron (BSE) image in as-polished conditions SE images were taken wherever required on specimens lightly etched with Kallings reagent earlier described. Qualitative analysis was carried out by EDAX to know the chemical composition of the alloys. Preloaded elemental standards for the characteristic x ray intensity of elements other than Ga were used to compare and to have a realistic estimate of the constituent elements. Semiconductor grade gallium arsenide was used to compare the counts for Ga and the analysis so obtained to low magnifications were compared with results obtained by other techniques for correlation.

3.3.4 Transmission Electron Microscope (TEM)

The Transmission Electron Microscopy (TEM) is a well established technique to see micro-details of the samples. An optical microscope uses lens combinations serially magnify the image. Resolutions possible with visible light limits the meaningful magnifications possible to ~1500X. The wavelength of illumination that is produced by an energized beam of electrons in TEM increases greatly the resolving capabilities, thus permitting the use of TEM to examine the specimen structure, composition or properties in submicroscopic details with higher resolution as well as magnification.

The principles and instrumentation of TEM has been described in details in literature (Thomas 1962, Heidenreich 1964, Barrett and Massalski 1980). The basic components of a TEM are a high vacuum column and suitable electron optics. High vacuum is necessary to permit a hindrance path to moving electrons and electron optics *viz.* the electromagnetic lenses serve the function of bending the particles/ waves much the same way as conventional lenses in optical microscopy. There are essentially three types of lenses used to form the final image in the TEM. These are the condenser, objective, and projector lenses. The main function of the condenser lens is to concentrate and focus the beam of electrons coming off of the filament onto the sample to give a uniformly illuminated sample. The objective lens and its associated pole pieces is the heart of the TEM and the most critical of all the lenses. It forms the initial enlarged image of the illuminated portion of the specimen in a plane that is suitable for further enlargement by the projector lens. Also, the TEM builds an image by way of differential contrast. Those electrons that pass through the sample go on to form the image while those that are stopped or diffracted by dense atoms in the specimen are subtracted from the image. In this way a black and white image is formed called Bright field image. If the diffracted beam is used to produce image, it is called a dark field image. Sometimes the image of the diffracted beams is used for further projection giving the diffraction pattern or selected area diffraction pattern giving useful information about the inter-atomic spacing much the same way as x-ray diffraction, but for the minute area selected in TEM. Finally, one uses the projector lens to project the final magnified image onto the phosphor screen or photographic emulsion. It is in the projector lens that the majority of the magnification occurs. Thus total magnification is a product of the objective and projector magnifications. For higher magnifications an intermediate lens is often added between the objective and

projector lenses. This lens serves to further magnify the image. The image is then projected onto either the fluorescent screen or onto the photographic film.

As the electrons have to pass through the specimen, very thin samples are essential requirement for the TEM. Elaborate specimen preparation procedures are available today. While the conventional thinning techniques such electro-polishing etc. were used earlier, ion beam thinning techniques are more common today to minimize the artifacts of the sample preparation techniques.

Thin foils for TEM were prepared by using the ultrasonic disc cutter to cut 3mm disc from the ribbons and then mounted into GATAN-PIPS (precision ion polishing system) holder and milled gently using initially at 5KV and subsequently at 4KV in varying angles of the ion gun. The milled foiled is removed and loaded inside the TEM. TEM studies were carried out in a FEI Tecnai G2 Transmission Electron Microscope using 200 kV. Fig 3.5 shows the equipment used for microscopy and specimen preparation. While the bright filed images have been mainly taken for understanding the microstructural ribbons, the Selected Area Diffraction (SAD) patterns were taken to understand the crystal structure of the ribbon specimens. The information obtained through SAD patterns has been correlated to the x-ray diffraction patterns. The x ray diffraction patterns only have been relied for lattice parameters estimation as a more accurate technique. .

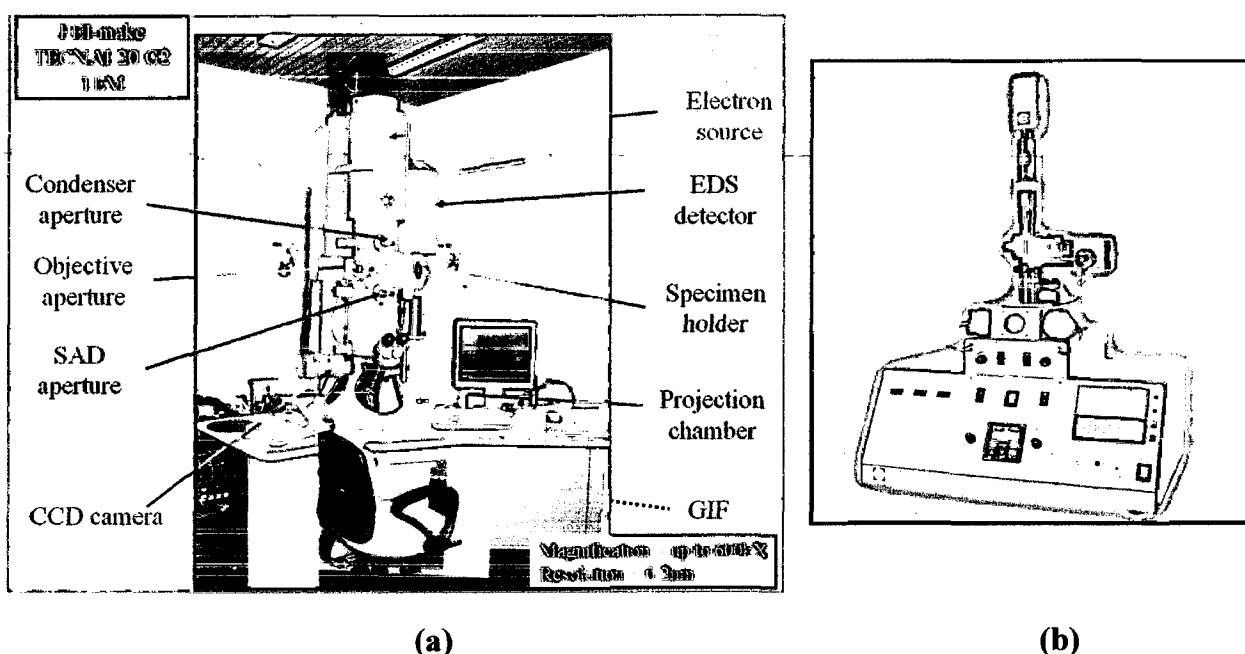


Fig 3.5: (a) Transmission Electron Microscope and (b) the specimen preparation Precision Ion Polishing System (PIPS)

3.3.5 Mössbauer Spectroscopy

Though limited only to some isotopes and to solid materials or frozen solutions, Mössbauer spectroscopy often plays a decisive role in the area of materials science as a complementary tool to the diffraction techniques (Wertheim 1964). The phenomenon of recoilless emission and resonant absorption of nuclear gamma rays in solids discovered by the German Physicist Rudolf L. Mössbauer is called the Mössbauer effect (Mössbauer 1958, 1959).

Nuclei in atoms undergo energy level transitions, often associated with the emission or absorption of γ - rays. These energy levels are influenced by their surrounding environment, both electronic and magnetic, which can change or split these energy levels. The changes in the energy levels can provide information about the atom's local environment within a system provided the information about them is observed using resonance-fluorescence. The recoil of the nucleus in a single atom as the γ -ray is emitted or absorbed prevents resonance and secondly the 'hyperfine' interactions between the nucleus and its environment are extremely small as compared to the γ - ray energy.

The recoil of the nucleus is avoided if the emitting / absorbing atom is embedded in a much heavier crystal lattice thereby making the recoil of the atom almost zero. Under such recoilless conditions, both emitting/ absorbing nuclei if under identical environment will be in resonance giving a single line absorption spectrum. In reality, the absorbing nuclei have an environment different from emitting nuclei in terms of energy level modifications such as electron monopole interactions, anisotropic charge distribution around nucleus or the magnetic splitting.

Even though the emitted γ -rays energy is very large, small hyperfine interactions between the atom and the surroundings can be probed view of the small line width caused by the average life time of decay of the nucleus undergoing transition. The relative number of recoil-free events (and hence the strength of the signal) is strongly dependent upon the γ - ray energy and so the Mössbauer effect is only detected in isotopes with very low lying excited states. Similarly the resolution is dependent upon the lifetime of the excited state. These two factors limit the number of isotopes that can be used successfully for Mössbauer

spectroscopy. The most used is ^{57}Fe , which has both a very low energy gamma-ray and long-lived excited state, matching both requirements well. Fe containing materials are accordingly investigated through this technique.

A Mössbauer spectrometer is employed to produce a known and precise energy shift between the Mössbauer source and absorber. The method of velocity modulation of the gamma ray energy by means of Doppler Effect, described by Mössbauer provides the basis for all Mössbauer spectrometers. This is accomplished by either the measurement of the total number of transmitted gamma photons for a fixed time at a constant velocity, followed by subsequent counting at other velocities, in the way the spectrum is scanned step-wise; or by rapid scanning through the whole velocity range in one cycle and subsequent numerous repetitions of this scan. The spectrometers are accordingly classified as constant velocity or the constant acceleration spectrometers.

A constant acceleration spectrometer (M/s fast ComTech) using a ^{57}Fe source has been used for analysis of Fe containing alloys in this study and is shown in Fig 3.6. The spectrometer was calibrated with natural iron foils (25 μm thick) prior to data collection for the spectrum. The alloys were hand crushed to powders of less than 20 μm to ensure γ -ray penetration. In view of low Mössbauer fractions earlier reported for Ni-Mn-Ga alloys, no dilution was used for the powders and long time data acquisition was carried out for counts exceeding 8×10^5 for each sample. With source strength of 25 mC, this required about 120-140 h of data collection with data collection time increasing proportionately with lower source strength. The obtained spectra were analyzed using PCMOSS-II program using a line width of 0.35-0.40 mm/s. The isomer shifts are reported with respect to natural iron. The analyzed spectra gave the values obtained for isomer shift, quadrupole splitting and the magnetic hyperfine field and the obtained values have been interpreted to understand the environment of the Fe nuclei contributing to the concerned spectrum.

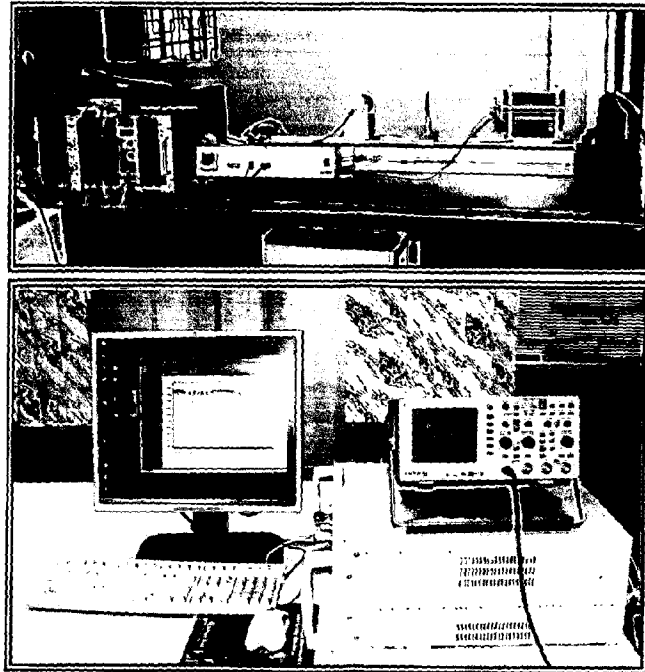


Fig 3.6: Constant acceleration spectrometer; top: arrangement showing fixed specimen holder and velocity modulator for the ^{57}Fe source and bottom: data logging system.

3.4 MAGNETIC CHARACTERISATION

The principle of VSM was first developed by Foner (Foner 1956, 1959) and details of the basic instrumentation are available in literature (Cullity 1972, Jiles 1998). A sample placed in a uniform magnetic field encounters a magnetic dipole moment directly proportional to the sample's susceptibility and the applied magnetic field is induced in the sample. Under sinusoidal vibrating motion, this moment induces an electric signal in suitably located pick-up coils. The induced signal is at the vibration frequency and is proportional to the sample's magnetic moment, vibrational amplitude and frequency. The material being investigated is kept in a sample holder placed within uniform magnetic field of an electromagnet as shown in Fig 3.7.. A slender vertical sample rod connects the sample holder with a transducer assembly located above the magnet, which in turn is supported by sturdy and adjustable support rods. The transducer converts a sinusoidal drive signal, provided by an amplifier located in the console of the electronic system, into a sinusoidal vertical vibration

of the sample rod and the sample is thus made to undergo a sinusoidal motion in a uniform magnetic field. The sinusoidal motion is at a fixed frequency, causing the field due to sample magnetization to vary at the same frequency.

Pick up coils are mounted on the pole pieces of the electromagnet to record the signal resulting from the sample motion. The signal, as indicated earlier is proportional to the magnetic moment as well as instrumental parameters such as vibration amplitude and frequency. A separate vibrating capacitor placed on the vibrating rod is used to generate compensating signal proportional to vibration amplitude and frequency so that the differential signal is proportional to the magnetic moment of the sample.

The system is calibrated prior to the measurements using a nickel reference disk specimen (weight 0.0925g at uniform magnetic field of 5kOe to give a saturation moment of 56emu/g). Calibrations could be maintained within $\pm 0.05\%$. The open loop measurements in VSM need correction for the demagnetization factor for different shapes. A uniform specimen size of 2mm x 1mm was therefore chosen to ensure a one to one comparison without incorporating the demagnetization factors. The bulk samples were cut in to rectangular shape of dimension 2mm l x 1mm w x 1mm t with the help of an ISOMET cutter. For the ribbon samples 2mm x 1mm rectangle was punched. The sliced specimen was fixed onto a quartz rod and was placed on the vibrating assembly with thickness perpendicular to the magnetic field. For the thermo-magnetic measurements, a small constant magnetic field of 500 Oe or 1000 Oe was applied within a temperature range of -80°C to 200°C , with a heating rate of $3^{\circ}\text{C}/\text{min}$ and the corresponding magnetic transitions and phase transformation were studied. The transition temperatures were determined by the tangent intercept method wherein the onset of transition is taken as the intersection point of the tangents surrounding the transition. The hysteresis loops (M-H curve) have been obtained at room temperature applying magnetic field up to -20 kOe to $+20$ kOe.

Magnetic measurements were carried out using a vibrating sample magnetometer (VSM)-Model EV9 from M/s ADE Technologies shown in Fig.3.6. A maximum magnetic field of 2.5 T can be applied while the sample temperature is controlled between 80K and 1000K.

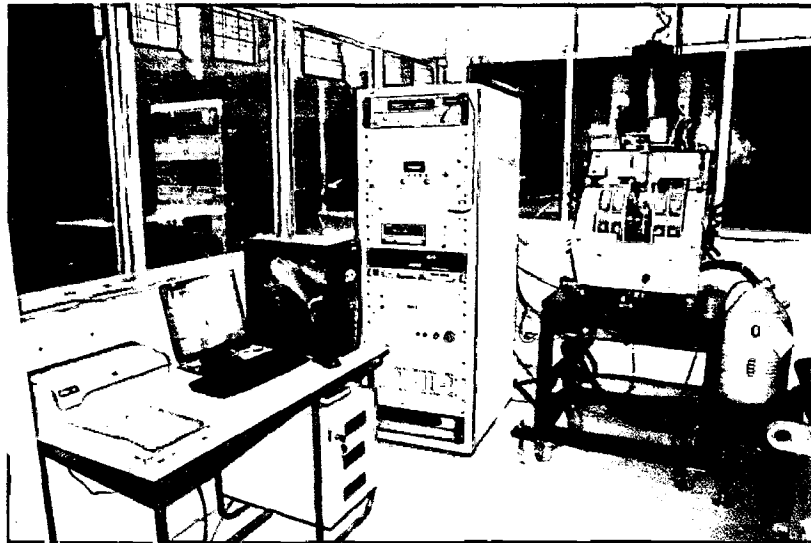


Fig.3.7: The Vibrating Sample Magnetometer

3.5 THERMAL ANALYSIS

The thermal analysis techniques involve measurement of physical properties of a sample vis – a –vis an inert reference as a function of a pre-programmed thermal heat inputs. The heat inputs can be at constant temperature (isothermal) or at constant heating rates (isochronal) or combinations. Based on the physical properties measured, a range of techniques are available for characterization. Of these, the Differential scanning calorimetry (DSC) is employed here. The differential heat flow is the physical property under measurement for the former, whereas the latter employs the differential temperature between the sample and reference. Though the basic signal in both the techniques is temperature difference, the signal is normalized to the calorimetric values electronically. The DSC units normally have limited temperature ranges as conversion of the basic signal becomes difficult when heat transfers to the specimens are not linearly proportional at higher temperatures due to mixed mode heat transfers (all the modes of heat transfers viz conduction, convection and radiation may be active in interim temperatures of ~1000-1500K). High temperature DSCs have however become possible with advancements in electronics and data storage facilities.

Differential scanning calorimetry (DSC) as a thermo-analytical tool has been employed to identify the structural and magnetic transition temperatures in the present study.

As a scanning over temperature range was required, isochronal treatments at fixed heating/cooling rates were programmed. The sample undergoing a physical transformation requires a different heat flow than the reference to maintain both at the same temperature. By observing the difference in heat flow between the sample and the reference, the amount of energy absorbed or released during such transitions can be estimated. M/s TA Instruments make MDSC Q100 (Fig 3.8) was used for monitoring low enthalpy change solid state transformations/ transitions. The transition temperatures here also were estimated through tangent intercept method defined for thermo magnetic measurements through VSM.

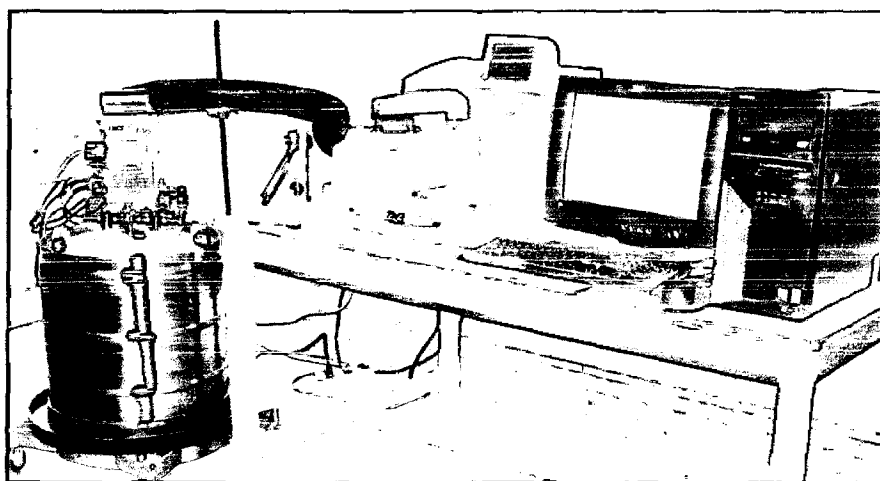


Fig.3.8: Modulated Differential Scanning Calorimeter along with liquid nitrogen pumping system at left

For DSC measurement, a small sample with two flat surfaces was cut from bulk alloy. The sample weight was in the range of 20-100 mg. After weighing sample was encapsulated in aluminum cups and then carefully placed in the DSC cell. The differential heat flow measurements were carried out in temperature range of 123 K to 873 K using Liquid nitrogen cooling system and finned air cooling system. The heating/cooling rate was kept constant (20 °C/min) for all measurement. The obtained data was then analyzed for studying martensite transformation and ferromagnetic transition.

3.6 MECHANICAL PROPERTIES MEASUREMENTS

Mechanical testing was employed for a few specimens to know their ductility and the detwinning stresses for the martensite phases. An Instron 5500 unit was used. Cuboidal specimens with a square cross-section of dimensions 3.75mmX 3.75mm X 7.5-8mm were tested in compression using a cross-head speed of 0.01 mm/min. The stress strain curves were then plotted. No arrangement for the magnetic field application could be made with the setup and the measurements are zero magnetic field measurements.

RESULTS AND DISCUSSION: ALLOYS WITH TRANSITION ELEMENT REPLACEMENTS

This chapter describes preparation and characterization of the quaternary alloys based on substitution by Fe/Co in ternary $\text{Ni}_{50}\text{Mn}_{30}\text{Ga}_{20}$ alloy. The results obtained with a base alloy for reference are first compiled followed by those for alloys developed with the intention of fixed addition of Fe/Co substituting for Ni and the alloys developed with the intention to replace Mn with varied amount of Fe. The obtained results are discussed in terms of the phase structure, its modification with additions at different atomic sites and the transformation characteristics.

4.1 RESULTS OF STUDIES WITH THE BASE ALLOY COMPOSITION

$\text{Ni}_{50}\text{Mn}_{30}\text{Ga}_{20}$

A base alloy composition designated as NMG was arc melted, cast, cut, sealed in evacuated quartz ampoules and heat-treated at 1273 K for 72h and 1073K for 48h in a vacuum furnace and water quenched.

4.1.1 Chemical Composition of Alloys

The Table 4.1 gives nominal and composition of the alloy analyzed by ICP-OES technique. The analysis in weight % has been shown as equivalent atom % for comparison with the intended composition. The analyzed alloy composition showed the Ga content to be ~17 atom% instead of intended 20%, the Mn/Ga ratio for the alloy accordingly works out to be 1.86 instead of 1.5 for the intended nominal compositions.

Table 4.1: Nominal and analyzed compositions of the base alloy composition NMG

Chemical Composition	Atom %			Weight%		
	Ni	Mn	Ga	Ni	Mn	Ga
Nominal	50	30	20	49.098	27.572	23.330
Analyzed	51.00	31.89	17.11	50.41 ±0.42	29.50 ±0.50	20.09 ±0.30

4.1.2 Structural Characterization of the Alloy

The room temperature x-ray diffractogram of the heat-treated alloy is shown in Fig 4.1. While the stoichiometric Ni₂MnGa alloys are reported to show an L2₁ structure, the off stoichiometric alloys show different martensite structures at room temperatures. The ternary β-NiMnGa phase is reported with the B2 CsCl type structure at high temperature and changes to the L2₁ Heusler type structure at lower temperature (Overholser et al 1999). The calculated diffraction pattern based on crystal structure data reported in literature for stoichiometric Ni₂MnGa alloy (Brown et al 2002) for different structures are shown in Fig 4.2. Fig 4.2 has been employed as a template for comparison of diffraction patterns of Ni-Mn-Ga and derived alloy compositions. The alloy NMG showed a tetragonal martensite structure and has been indexed accordingly. The peak positions, d-spacing and the corresponding diffracting plane index are provided in table 4.2.

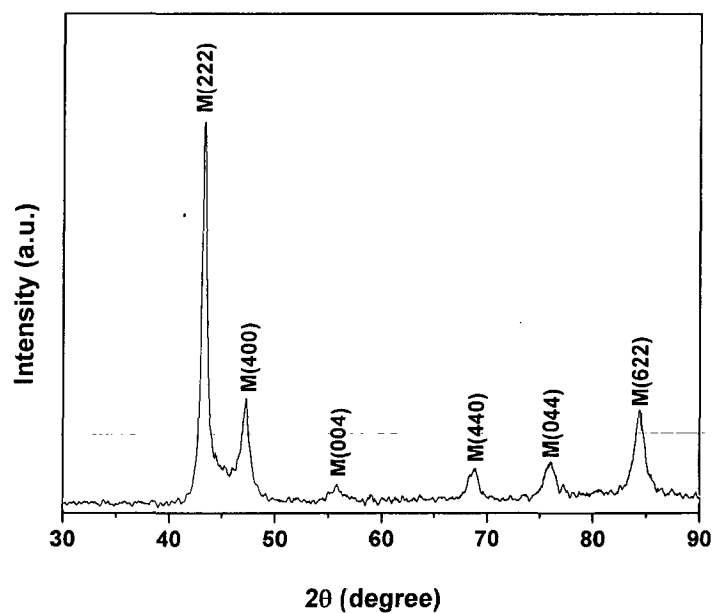


Fig 4.1: The x-ray diffractogram for the base alloy NMG

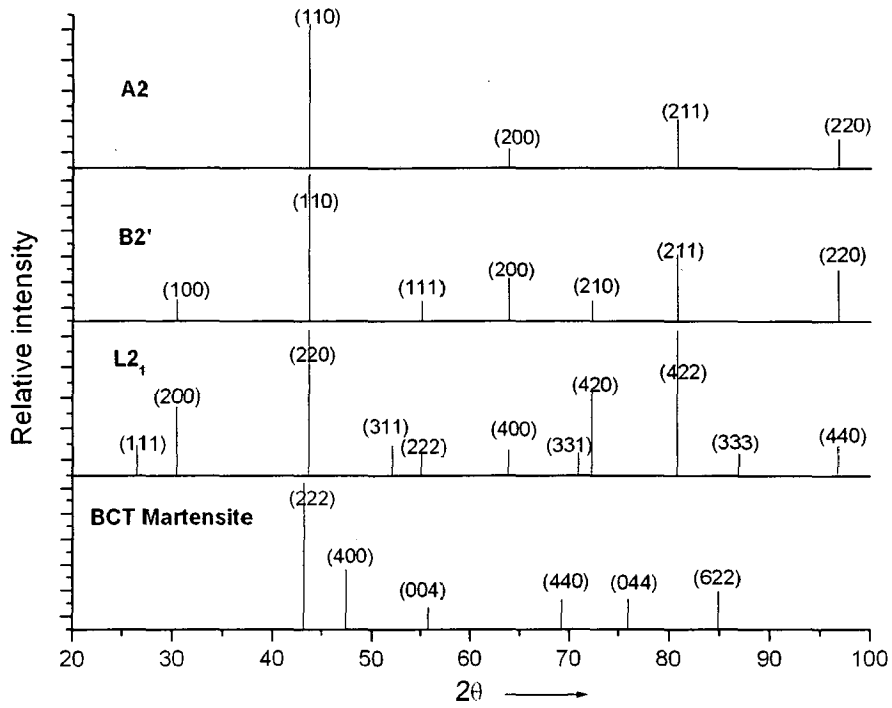


Fig 4.2: The calculated x-ray diffractograms for different structures of Ni₂MnGa based on the reported values by Brown et al 2002

Table 4.2: The peak positions, d-spacing and the corresponding atomic plane of the tetragonal martensite phase for the diffractogram of alloy NMG.

2θ (deg)	d-spacing (Å)	Corresponding atomic plane of the tetragonal martensite phase
43.18	2.093	222
47.129	1.926	400
55.679	1.649	004
68.68	1.365	440
75.86	1.253	044
84.32	1.147	622

The lattice parameter for the martensite phase fitted with the above d-spacing were calculated with least square fitting and were found to be $a = 7.7306 \text{ \AA}$ and $c = 6.5906 \text{ \AA}$. The unit cell volume for the phase therefore is estimated as 393.868 \AA^3 with c/a ratio of 0.852.

4.1.3 Transformation Characteristics

The Differential Scanning Calorimetry (DSC) has been employed to investigate the transformation characteristics of the alloy. Fig 4.3 shows the DSC thermogram of the alloy. The observed structural transformation temperatures i.e. martensite transformation (start T_{Ms} and finish T_{Mf} during cooling as well as austenite start T_{As} and finish T_{Af} temperatures during heating) obtained from the thermograms are 364, 351, 366 and 379K respectively. The enthalpy change during cooling i.e during martensite transformation was 6.343 J/g and during heating i.e. reverse transformation was 6.512 J/g.

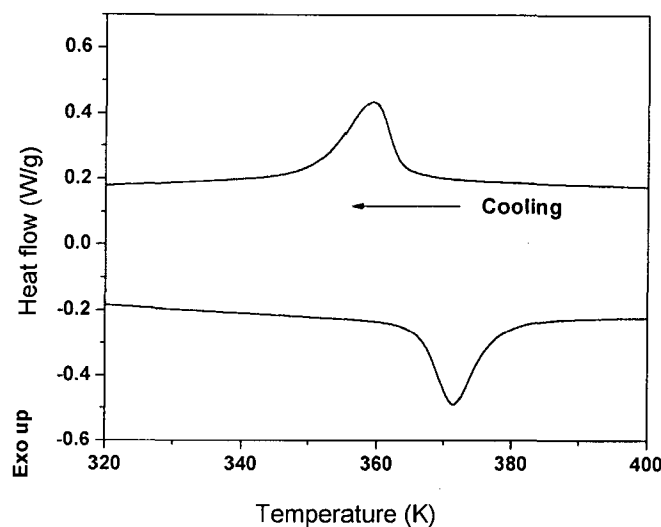


Fig 4.3: The DSC thermogram for the heat treated alloy NMG

The thermo-magnetic measurements have been employed to supplement the DSC transformations and are shown in Fig 4.4 as the magnetization of the alloy as a function of temperature at a biasing field of 500 Oe. The measurement in Fig 4.4 shows an anomalous increase in magnetization with increase in temperature followed by fall due to Curie transition on further rise in temperatures. The magnetization usually falls with increasing temperature due to thermal disorder of the magnetic domains. An anomalous rise of magnetization with increasing temperature is commonly noticed for Ni-Mn-Ga alloys prior to a fall due to

paramagnetic (Curie) transitions. The saturation magnetization of martensite phase is normally higher than the corresponding austenite phase, however these phases are more anisotropic than their cubic counterparts and the specific magnetization at low biasing field show a rise with increasing temperature on the martensite to austenite transformation. The rise in magnetization therefore is attributable to a martensite transformation. These measurements for the alloy NMG therefore revealed Curie transition at 377K and martensite transformation temperature at 344 K. As stated earlier, unlike isochronal measurements in DSC, the M-T measurements have been taken during heating cycle measured as a step of 3K allowing adequate time for magnetization to stabilize. Considering different measurement techniques the difference in measured transitions is small and the two measurements complement each other.

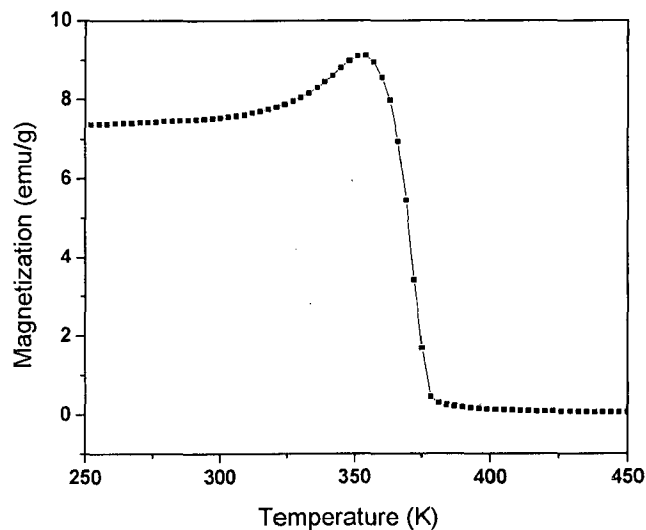


Fig 4.4: The M-T thermo-magnetic measurements for the heat treated alloy NMG

4.1.4 Room Temperature Magnetization Behavior

The room temperature magnetization curve for alloy NMG is presented in Fig 4.5. The curve showed a moderate coercivity and a saturation magnetization value of 50.89 emu/g.

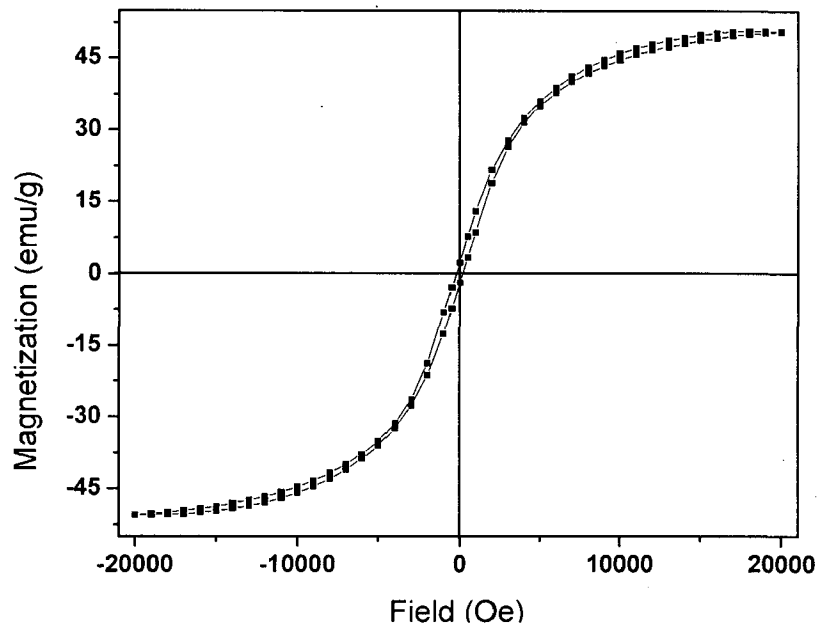


Fig 4.5: Room temperature magnetization M-H curve for the heat treated alloy NMG

4.2 RESULTS OF STUDIES WITH THE INTENTION TO REPLACE Ni by Fe/Co in $\text{Ni}_{50}\text{Mn}_{30}\text{Ga}_{20}$

The alloys $\text{Ni}_{40}\text{Fe}_{10}$ and $\text{Ni}_{40}\text{Co}_{10}$ were cast and the cast alloys were cut, heat-treated at 1273 K for 3 hrs in a vacuum furnace and gas quenched as described in Chapter-3. The alloys were characterized both in as cast and heat-treated conditions to understand the effect of the additives as well the effectiveness of the heat-treatment given.

4.2.1 Chemical Composition of Alloys

Table 4.3 gives the nominal compositions and the analyzed compositions of the alloys prepared. The analyzed compositions of the alloys are within about 3 atom % of the intended compositions. While the analyzed compositions show the Ga content to be around 18%, The Mn/Ga ratio for the $\text{Ni}_{40}\text{Mn}_{10}$ and $\text{Ni}_{40}\text{Co}_{10}$ alloy ratio with these result works out to be 1.62 and 1.68 respectively instead of 1.5 for the intended nominal compositions.

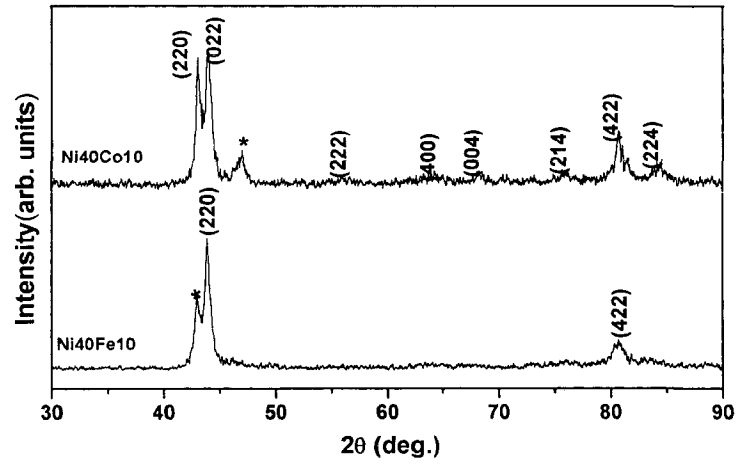
Table 4.3: Nominal and analyzed compositions of the Ni40Fe10 and Ni40Co10 alloys

Alloy Designation	Nominal Composition				Analyzed Composition							
	Atom %				Wt%				Equivalent average atom%			
	Ni	Mn	Ga	Additive	Ni	Mn	Ga	Additive	Ni	Mn	Ga	Additive
Ni40Fe10	40	30	20	10Fe	42.33 ±0.36	25.92 ±0.31	20.34 ±0.64	11.39 ±0.27Fe	42.70	27.94	17.28	12.08Fe
Ni40Co10	40	30	20	10Co	38.35 ±0.23	29.56 ±0.29	22.20 ±0.40	9.89 ±0.12Co	38.95	32.07	18.98	10.00Co

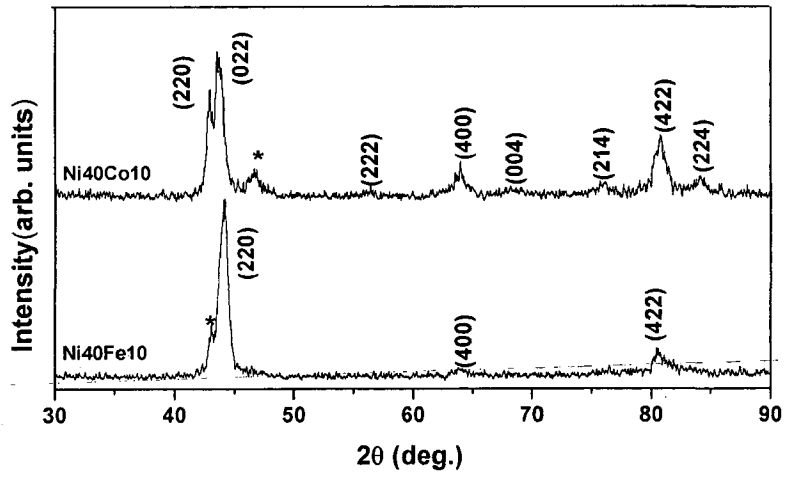
4.2.2 Structural Characterization of the Alloys

(a) X-ray Crystallography

The X-ray diffractograms of the two alloys Ni40Fe10 and Ni40Co10 are shown in as-cast and heat-treated conditions in Fig 4.6a and Fig.4.6b, respectively. The diffractograms can be indexed to either BCC or BCC derived structures. Patterns for the alloy Ni40Fe10 have been indexed to L2₁ (austenite) phase in line with previous reports wherein the superlattice L2₁ reflections were not visible in x-ray diffractograms (Jiang et al 2004, Xu et al 2006, Li et al 2003). The diffractograms for the alloy Ni40Co10 showed lower symmetry than cubic structure of alloy Ni40Fe10 and could be indexed to a martensite structure. The crystallographic presentation for the martensite structure is done either through modified tetragonal co-ordinates or the parent phase co-ordinates (Soderberg et al 2005). As we have got both L2₁ and 5M martensite structure in our alloys, we have followed the parent phase co-ordinates for ease of comparison. The diffractograms for our alloys have been analyzed and reflections marked are shown accordingly in the diffractograms (Fig 4.1). The table 4.2 gives the observed peak positions, the inter-planar d-spacing and their assignment to the reflecting planes of the corresponding austenite and martensite phases. The indexing patterns being similar to those reported earlier for martensite structure indexed in parent phase coordinates (Wang et al 2002), the literature indexing values for Ni₅₂Mn₂₄Ga₂₄ single crystals have also been shown alongside in the table. One reflection each for Ni40Fe10 and Ni40Co10 could not be attributed to these phases. The major phase structure of cast alloys at room temperature did not change on the heat-treatment; however the relative intensity of the extra reflection went down on heat-treatment with corresponding small change in inter-planar spacing.



(a)



(b)

Fig 4.6: X-ray Diffractograms (Cu $K\alpha$) at a scan rate of $1^\circ(2\theta)/\text{min}$ for (a) as-cast and (b) heat-treated quaternary alloys. The identified reflections are marked for cubic austenite phase for alloy Ni₄₀Fe₁₀ and 5M martensite phase for alloy Ni₄₀Co₁₀. The un-indexed secondary phase reflections are marked with *

Table 4.4: The assignment of the x-ray diffractogram peaks for the Cast and heat-treated Ni40Fe10 and Ni40Co10 alloys to various phases. (A denotes 2θ (deg) and B denotes d-spacing (Å))

Alloy Ni40Fe10				Alloy Ni40Co10				Similarly indexed Ni-Mn-Ga alloy phases#			
As Cast Condition		heat-treated		As Cast Condition		heat-treated		Austenite Cubic L2 ₁		Martensite 5M	
2θ (°)	d-spacing (Å)	2θ (°)	d-spacing (Å)	2θ (°)	d-spacing (Å)	2θ (°)	d-spacing (Å)	(hkl)	d-spacing (Å)	(hkl)	d-spacing (Å)
42.91	2.105	42.89	2.106					*			
				43.05	2.099	42.78	2.111			220	2.100
43.77	2.066	44.25	2.044					220	2.059		
				44.00	2.055	43.67	2.070			022	2.023
				46.96	1.933	46.59	1.947	*			
				56.30	1.632	56.27	1.633			222	1.672
		63.86	1.456					400	1.456		
				64.07	1.451	63.92	1.455			400	1.485
				68.27	1.372	68.72	1.364			004	1.382
				75.92	1.252	75.97	1.251			214	1.226
80.53	1.191	80.56	1.191					422	1.188		
				80.68	1.189	80.72	1.189			422	1.197
				84.42	1.146	84.18	1.145			224	1.154

* shows the reflections which could not be indexed to the major phase and are attributable to secondary phase # Values for Ni₅₂Mn₂₄Ga₂₄ single crystals (Wang et al 2002)

(b) Microstructure and Phase Constituents

The microstructures in Fig 4.7a and 4.7b respectively for the as-cast Ni40Fe10 alloy and Ni40Co10 alloy show the presence of secondary phase in the former alloy but the latter has only one phase. Fig 4.3a shows streaking marks suggesting erosion of secondary phase during polishing. Fig 4.8 shows the back scattered electron image of the heat-treated alloys. Homogeneity of the microstructure was checked using point analysis by the Electron Probe Microanalysis (EPMA). Both the alloys showed the constituent elements distributed

homogeneously. A typical line scan along the arrow mark in Fig 4.4a is presented in Fig 4.9. However, there are faint dark marks discontinuously along the grain boundary in Fig. 4.4a which could indicate presence of a small amount of secondary phase. The EPMA probe (size $0.9\ \mu\text{m}$) however did not show perceptible compositional variations along different line scans. The heat-treatment imparted to the alloys has thus ensured a homogeneous chemistry of the alloys

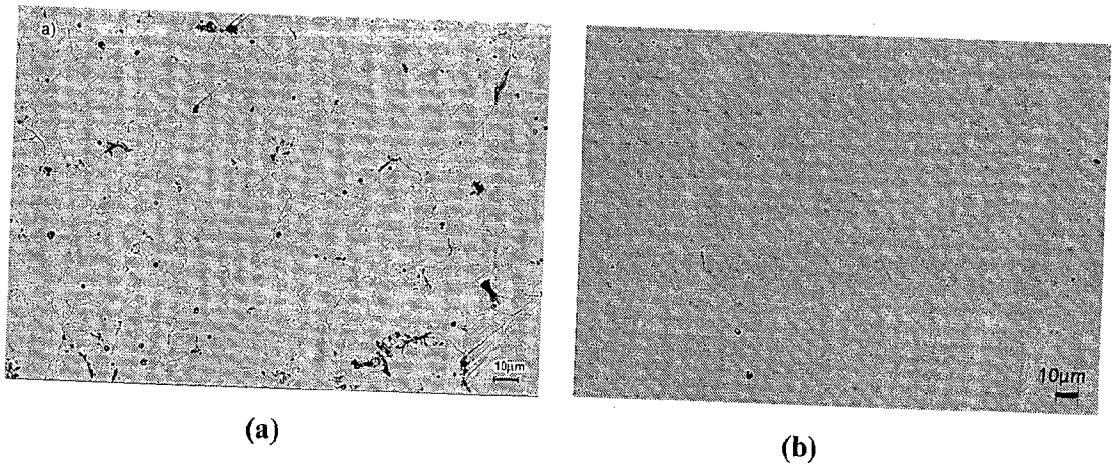


Fig 4.7: Back Scattered Electron Images of as-cast a) Ni40Fe10 alloy and b) Ni40Co10 alloy

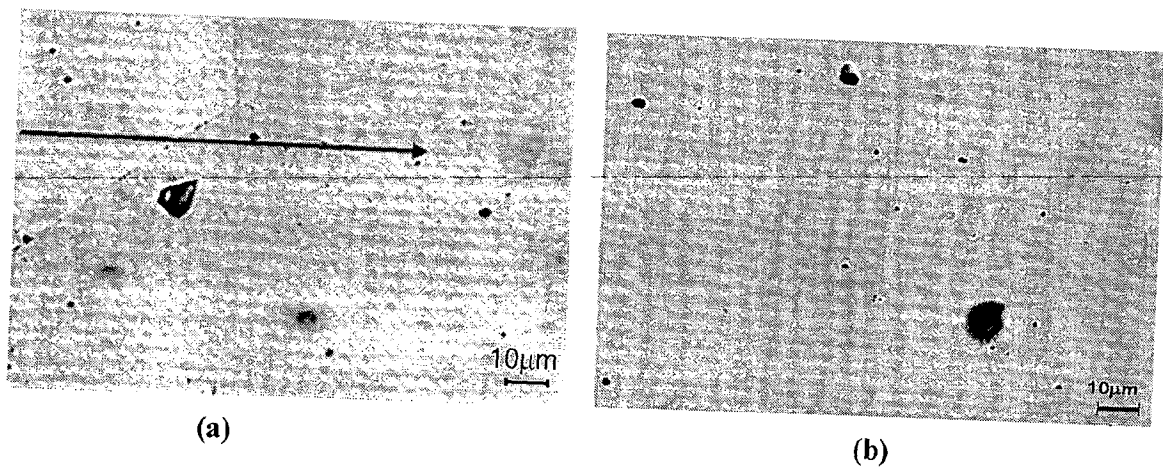


Fig 4.8: Back Scattered Electron Images of heat treated a) Ni40Fe10 alloy and b) Ni40Co10 alloy

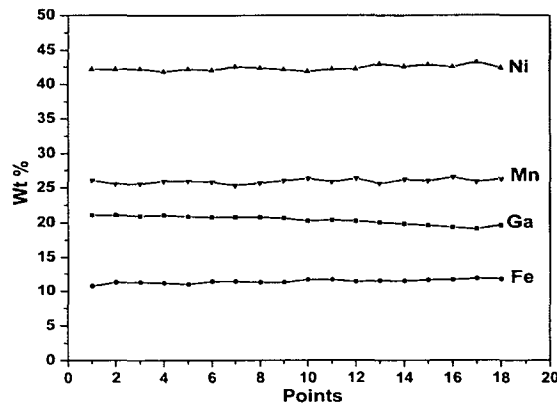


Fig 4.9: Electron Probe Microanalysis (EPMA) for annealed alloy Ni40Fe10 along the arrow in Fig 4.3a.

(c) *Mössbauer Studies*

Mössbauer spectrum of Fe containing alloy Ni40Fe10 in heat-treated condition was taken to understand and ascertain the occupation of Fe through magnetic nature of the phases present. Fig 4.10 shows the spectrum obtained for the heat-treated alloy. The obtained absorption spectrum analyzed with least square-fitting program available with the equipment could be de-convoluted to a sextet and a doublet (shown as spectrum S1 and S2, respectively) indicating the presence of Fe in both ferromagnetic and paramagnetic environment and the respective Fe intensity ratio is calculated to be 92 and 8% in the two environments with hyperfine field of Fe in the ferromagnetic sites as 29.3 T ($1.95 \mu_B$).

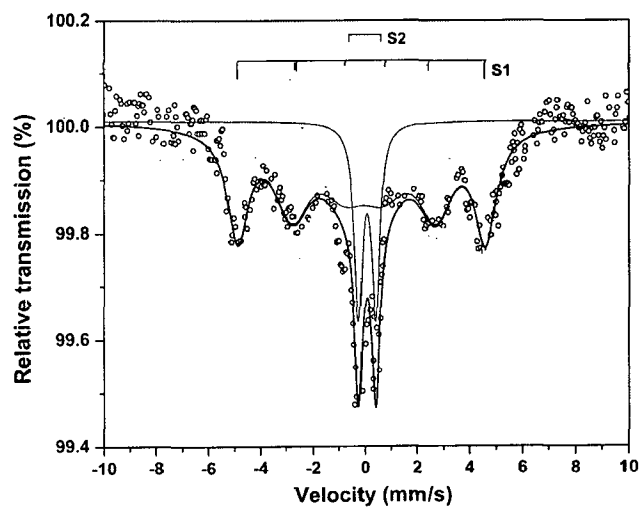


Fig 4.10: Mössbauer Spectrum of heat-treated Ni40Fe10 alloy at room temperature

4.2.3 Transformation Characteristics

The thermal analysis and thermo-magnetic measurements have been carried out to estimate the transformation temperatures for the alloys. The DSC thermo-grams (Fig 4.11) show the observed structural transformation temperatures i.e. martensite transformation (start T_{Ms} and finish T_{Mf} during cooling as well as austenite start T_{As} and finish T_{Af} temperatures during heating) and the Curie temperatures T_C . The values measured from the thermograms are compiled in Table 4.3. The second order Curie transition is seen as a change of slope in these thermograms. The Curie temperature during heating and cooling has shown a variation of about 2-3 K and the average temperatures have been noted. The martensite transformation appeared as a well-defined peak area signifying a first order transition with a discreet enthalpy change in case of the alloy Ni40Fe10. The alloy Ni40Co10 did not show any well defined peak for these transformations. A change in the characteristics of the curves however was noticed around at 361 K in cooling and 364 K in heating cycle signifying a transition in terms of the thermal characteristics. The change is marked with the arrow in heating cycle in the Fig 4.7.

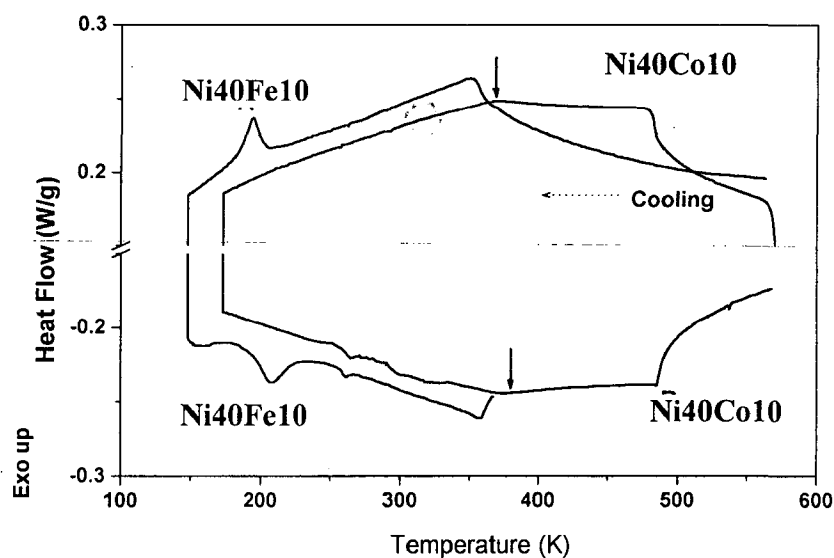


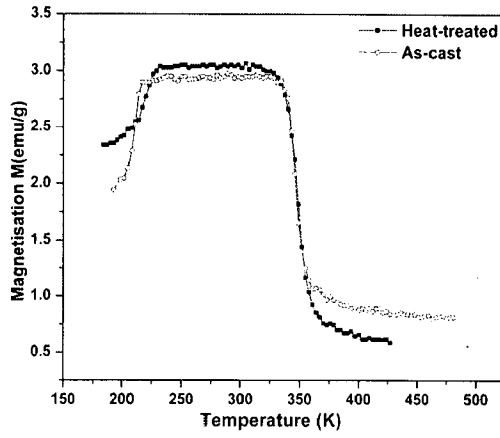
Fig 4.11: DSC thermograms for the heat treated alloys Ni40Fe10 and Ni40Co10

Table 4.5: Transformation temperatures through DSC for the alloys investigated

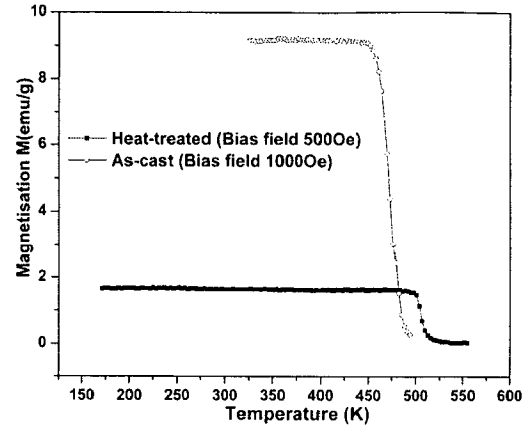
Alloy	Curie temperature (T_C) K	Martensite transformation temperature		Austenite transformation temperature		Enthalpy
		Start (T_{Ms}) K	Finish (T_{Mf}) K	Start (T_{As}) K	Finish (T_{Af}) K	$\Delta H_{M \rightarrow A}$ J/g
Ni40Fe10	355	206	183	191	224	0.91
Ni40Co10	481	361	-	364	-	*

* The enthalpy of transformation could not be determined in view of an unclear area under the curve

Fig 4.12 shows the magnetization of the alloys as a function of temperature at a biasing field of 500 Oe. The magnetization usually falls with increasing temperature due to thermal disorder of the magnetic domains. An anomalous rise of magnetization with increasing temperature prior to a fall due to paramagnetic (Curie) transitions was noticed for the alloy Ni40Fe10. The saturation magnetization of martensite phase is normally higher than the corresponding austenite phase, however these phases are more anisotropic than their cubic counterparts and the specific magnetization at low biasing field shows a rise with increasing temperature on the martensite to austenite transformation. The rise in magnetization therefore is attributable to an austenite to martensite transformation. Such measurements have been employed earlier also for estimating phase transformation temperatures (Khovailo et al 2004). The alloy Ni40Co10 did not show a rise in magnetization with temperature. In order to ensure the small differences in specific magnetization of the martensite and austenite phases are not masked in the low biasing fields, the magnetization curve for the heat-treated Ni40Co10 alloy was taken at a higher bias field of 1000 Oe. No austenite to martensite transformation was however visible for the alloy Ni40Co10.



(a)

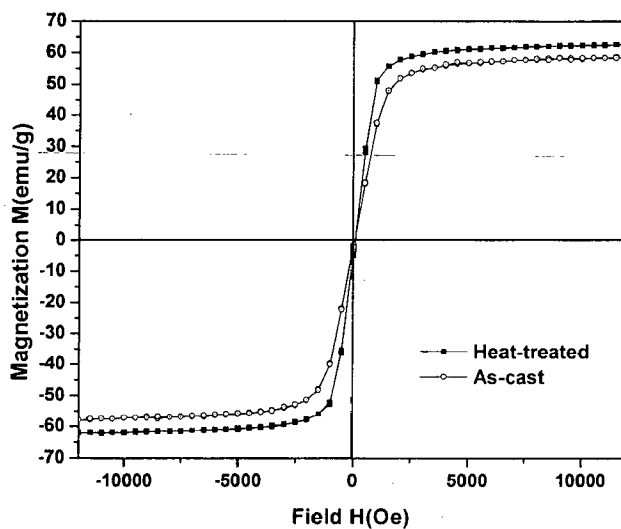


(b)

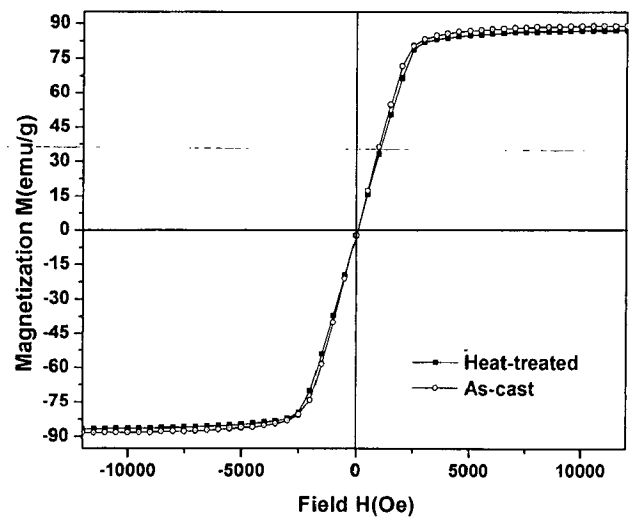
Fig 4.12: The magnetization- temperatures curves of a) alloys Ni40Fe10 and b) Ni40Co10 in as cast as well as heat treated conditions.

4.2.4 Room Temperature Magnetization Behavior

Fig 4.13 shows the magnetization of the alloys as a function of applied field at room temperature (M-H curves) in as cast and heat-treated conditions. Room temperature saturation magnetization values of 59.0 and 62.8 emu/g at a maximum magnetic field of 12 kOe are obtained for the alloy Ni40Fe10 in as cast and annealed conditions respectively. Saturation magnetization of 88 emu/g was obtained for the Ni40Co10 alloy in both as-cast and heat-treated conditions.



(a)



(b)

Fig 4.13: Room temperature magnetization curves of a) alloys Ni40Fe10 and b) Ni40Co10 in as cast and heat treated conditions.

4.3. RESULTS OF STUDIES WITH THE INTENTION TO REPLACE Mn by Fe in Ni₅₀Mn₃₀Ga₂₀

Alloys with intended composition Ni₅₀Fe_xMn_{30-x}Ga₂₀ (x=2.5, 5 and 15) substituting Fe for Mn have been planned. An alloy with lower Fe than composition Ni₄₀Fe₁₀ and Fe substituting for Ni viz. Ni₄₅Fe₅Mn₃₀Ga₂₀ has also been included for comparison and understanding the effect of low Fe additions. Alloys have been accordingly prepared by repeated arc melting. The as-cast alloys were cut, sealed in evacuated quartz ampoules and heat-treated at 1273 K for 72h and 1073K for 48h in a vacuum furnace and water quenched.

4.3.1 Chemical Composition

Table 4.6 shows the nominal composition of the alloys and the average chemical compositions obtained through ICP-OES, along with their designations of the alloys. Chemistry obtained through other techniques viz. EPMA and EDS, was comparable to these values and show the alloys to be close to their nominal compositions while ensuring macro-homogeneity.

Table 4.6: Nominal and analyzed compositions of the arc-melted Ni-Fe-Mn-Ga alloys

Alloy Designation	Nominal Composition				Analyzed bulk chemistry							
	Atom %				Wt%				Equivalent average atom%			
	Ni	Fe	Mn	Ga	Ni	Fe	Mn	Ga (Balance)	Ni	Fe	Mn	Ga
Mn27.5Fe2.5	50	2.5	27.5	20	50.0 ±0.60	2.78 ±0.10	28.20 ±0.20	19.02	50.47	2.95	30.42	16.16
Mn25Fe5	50	5	25	20	49.5 ±0.60	5.18 ±0.10	25.90 ±0.20	19.42	50.02	5.50	27.96	16.52
Mn15Fe15	50	15	15	20	49.0 ±0.60	13.9 ±0.25	18.0 ±0.20	19.1	49.54	14.77	19.44	16.26
Ni45Fe5	45	5	30	20	44.5 ±0.60	6.25 ±0.20	29.05 ±0.20	20.2	44.90	6.63	31.32	17.16.

4.3.2 Structural Characterization of the Alloys

(a) X-ray Crystallography

The X-ray diffractograms of the alloys obtained at a scan rate of $1^\circ(2\theta)/\text{min}$ are shown in Fig 4.14a. While the diffractograms for the alloys Mn₂₅Fe₅ and Ni₄₅Fe₅ could be indexed to tetragonal martensite phase similar to those obtained for Ni-Mn-Ga alloys and analyzed earlier, those for the alloys Mn_{27.5}Fe_{2.5} and Mn₁₅Fe₁₅ have shown additional lines. The additional reflections for the alloy Mn_{27.5}Fe_{2.5} (marked as • in fig 4.10a) disappear at higher Fe content.

The (222) reflection of martensite phase splits in 2 or 3 peaks for chemically modulated super-period martensite 5M or 7M structures respectively. Splitting of the peak is not noticed for the alloy Mn_{27.5}Fe_{2.5}. To ascertain the peak splitting, slower scans at $0.5^\circ(2\theta)/\text{min}$ around the (220) peak position were carried out and are presented in Fig 4.14b. An additional peak at 2θ value of $\sim 44.38^\circ$ can be seen for the alloy at slow scan. It may however be noted this peak position is matching with the peak at 44.39° for the alloy Mn₁₅Fe₁₅, which is attributed to a secondary phase. Moreover this peak is not well resolved. The reflection at 44.38° for the alloy Mn_{27.5}Fe_{2.5} could have been due to either a second phase or due to modulated structure causing peak splitting. However, in view of a single phase microstructure of the alloy Mn_{27.5}Fe_{2.5}, the alloy has been taken as single phase structure.

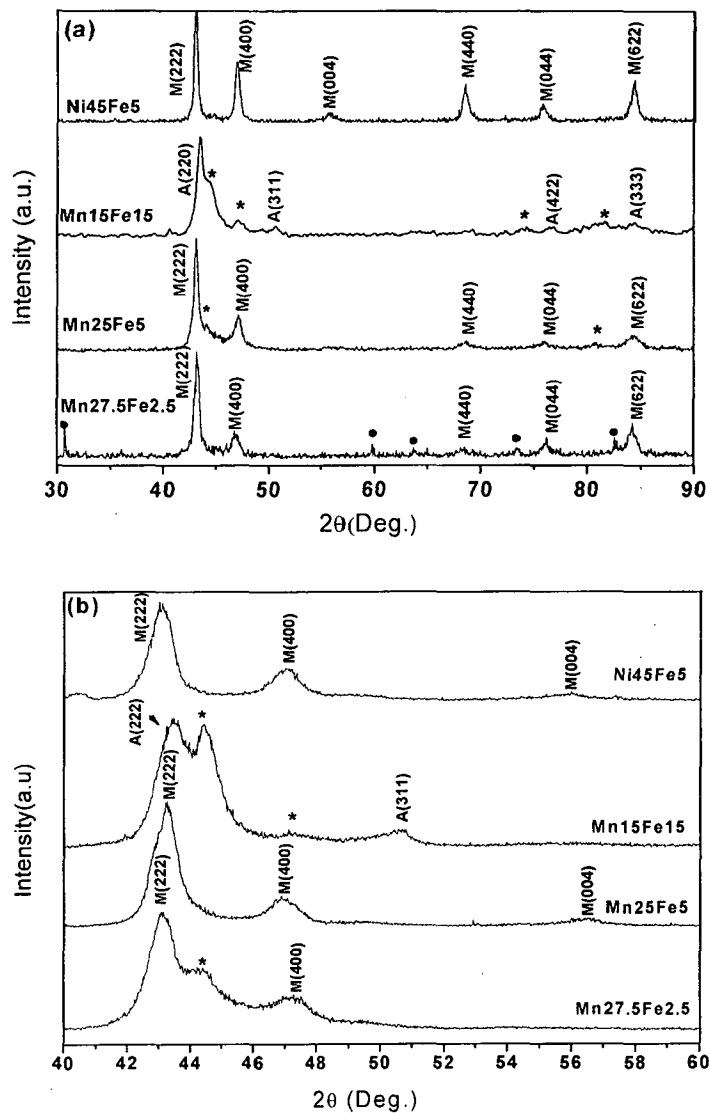


Fig 4.14: X-ray Diffractograms ($\text{Cu K}\alpha$) taken at (a) a scan rate of $1^\circ(2\theta)/\text{min}$ and (b) a scan rate of $0.5^\circ(2\theta)/\text{min}$ for the alloys Mn_{27.5}Fe_{2.5}, Mn₂₅Fe₅, Mn₁₅Fe₁₅ and Ni₄₅Fe₅. The phases identified (M-martensite and A-austenite) are marked with their reflections. The secondary phase in alloy Mn₁₅Fe₁₅ is marked with *. The • for alloy Mn_{27.5}Fe_{2.5} shows the reflections disappearing on random placement of Fe in other compositions in the series of alloys

Table 4.7: The assignment of the x-ray diffractogram peaks for heat-treated Mn_{27.5}Fe_{2.5}, Mn₂₅Fe₅, Mn₁₅Fe₁₅ and Ni₄₅Fe₅ alloys to various phases

Peak position								Assignment of the peak	
Mn _{27.5} Fe _{2.5}		Mn ₂₅ Fe ₅		Mn ₁₅ Fe ₁₅		Ni ₄₅ Fe ₅		Martensite 5M	Austenite Cubic L ₂₁
2θ (°)	d-spacing (Å)	2θ (°)	d-spacing (Å)	2θ (°)	d-spacing (Å)	2θ (°)	d-spacing (Å)	(hkl)	(hkl)
30.57	2.921								•
43.11	2.096	43.24	2.090			43.07	2.098	222	
				43.48	2.079				220
44.38		44.28	2.043	44.39					•*
46.86		46.84	1.937			47.14	1.926	400	
47.18				47.10	1.927				
				50.67	1.799				311
						55.89	1.643		
		56.40	1.629						
59.92									
63.85									
68.48		68.68	1.365			68.51	1.368	440	
				69.12	1.357				
73.34									
76.12	1.249	76.07	1.250					044	
				76.84	1.239	75.72			
				81.54	1.179				
		80.78	1.188						
84.28		84.39	1.146			84.28	1.148	622	

• The unindexed peaks disappearing on higher Fe content

* The peaks matching with second phase peaks in the Ga₁₅Fe₁₅ alloy

(b) *Microstructure and Phase Constituents*

Fig 4.15 shows the back-scattered electron images of the heat-treated alloys. Alloys Mn27.5Fe2.5, Mn25Fe5 and Ni45Fe5 have single-phase structures whereas a two-phase structure was noticed for alloy Mn15Fe15. In view of long heat-treatments, the cast structure should have broken down and the alloy shows an equilibrium phase structure. The average composition of the two phases in alloys Mn15Fe15 analyzed using EPMA was found to be $\text{Ni}_{49.09}\text{Fe}_{10.32}\text{Mn}_{19.74}\text{Ga}_{20.85}$ and $\text{Ni}_{43.45}\text{Fe}_{33.37}\text{Mn}_{13.40}\text{Ga}_{9.78}$ for the matrix and the embedded phase respectively.

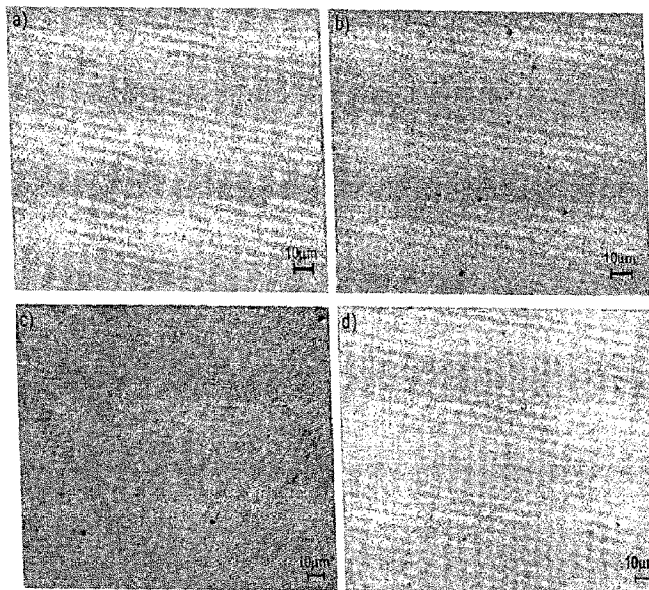


Fig 4.15: Back Scattered Electron Image a) of alloy Mn27.5Fe2.5, b) of alloy Mn25Fe5, c) of alloy Mn15Fe15 and d) of alloy Ni45Fe5.

(c) *Mössbauer Studies*

The room temperature Mössbauer spectra of the heat-treated alloys are presented in Fig 4.16. The spectra could be de-convoluted to a sub-spectrum of a doublet and a sextet in case of alloys Mn_{27.5}Fe_{2.5} and Mn₂₅Fe₅, and into a doublet and two sextets in case of alloys Mn₁₅Fe₁₅ and Ni₄₅Fe₅. The calculated fitting curves are shown in the Fig.4.16 along with the observed absorptions. The Mössbauer parameters derived from the observations and fitting parameters are compiled in table 4.8.

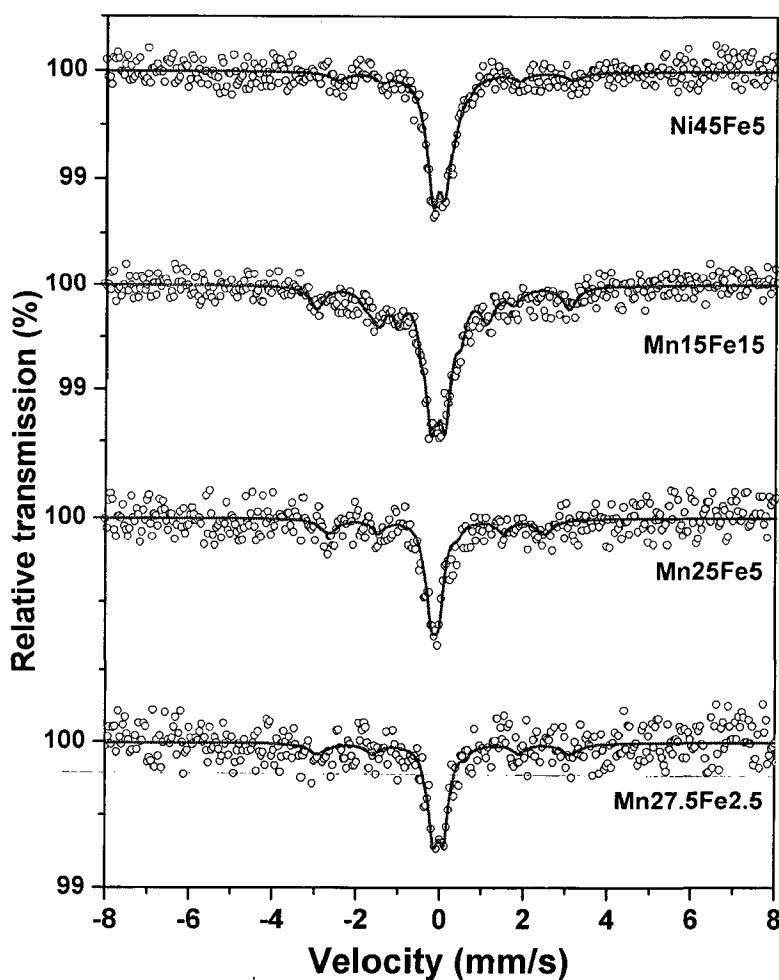


Fig 4.16: Mössbauer Spectrum of the alloys Mn_{27.5}Fe_{2.5}, Mn₂₅Fe₅, Mn₁₅Fe₁₅ and Ni₄₅Fe₅ taken at room temperature. The solid line indicates the fitting curve with parameters shown in table 4.8.

Table 4.8: Mössbauer parameters Hyperfine magnetic field (H_{hf}), quadrupole splitting (Q.S.), Isomer shift (I.S) and relative intensities for the ^{57}Fe Mössbauer spectra in Ni-Fe-Mn-Ga alloys.

Alloy Designation	Hyperfine Parameters				
	Sub-spectrum	H_{hf} T(μ_B) $\pm 0.2T$	Q.S. mm/s $\pm 0.05\text{mm/s}$	I.S. mm/s $\pm 0.002\text{mm/s}$	Intensity %
Mn27.5Fe2.5	Sextet	18.5(1.23)	0.05	0.110	18
	Doublet	--	0.26	-0.028	82
Mn25Fe5	Sextet	17.0(1.13)	0.10	-0.047	46
	Doublet	--	0.18	-0.033	54
Mn15Fe15	Sextet	8.2(0.55)	0.13	-0.237	13
	Sextet	19.0(1.26)	0.07	-0.016	38
	Doublet	--	0.35	-0.077	50
Ni45Fe5	Sextet	9.5(0.63)	0.12	0.140	13
	Sextet	17.5(1.16)	0.11	-0.008	17
	Doublet	--	0.26	-0.050	70

4.3.3 Transformation Characteristics

The DSC thermo-grams obtained for the alloys investigated shows the exotherms during cooling and endotherms during heating cycles (Fig 4.17). These events are attributed to structural martensite transformation and reverse transformation to austenite, respectively. The observed transformation temperatures (martensite start T_{Ms} & finish T_{Mf} and austenite start T_{As} & finish T_{Af} temperatures) as well as the transformation enthalpies from the thermograms are compiled in Table 4.8. The martensite transformation temperatures increase from alloy Mn27.5Fe2.5 to alloy Mn25Fe5. These values are lower for alloy Mn15Fe15. The alloy Mn15Fe15 also showed a transformation enthalpy value 2.67 J/g much lower than the other alloys. In view of the two-phase structure of the alloy (Fig 4.15c), this value appears to be lowered due to contributions of transformation enthalpy from only one of the two phases. Extended thermal scans up to the instrument limits (673K) were carried out and did not however reveal the transformation peaks for the second phase in case of alloy Mn15Fe15.

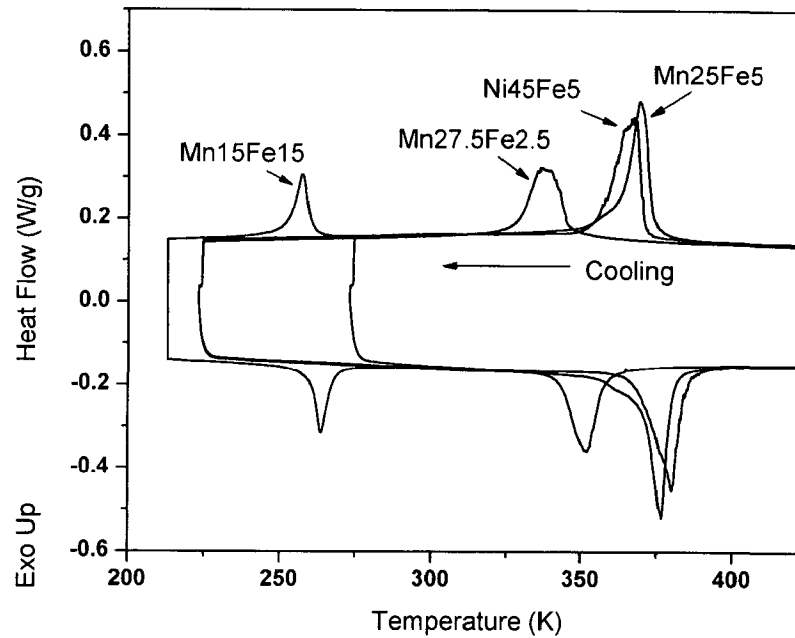


Fig 4.17: DSC thermograms for the alloys Mn27.5Fe2.5, Mn25Fe5, Mn15Fe15 and Ni45Fe5

The thermo-magnetic M-T measurements for the alloys are shown in Fig 4.18. The alloys Mn27.5Fe2.5 and Ni45Fe5 showed a fall in magnetization to zero i.e. to a paramagnetic state. Alloy Mn25Fe5 showed a rise in magnetization with increasing temperature prior to a fall due to paramagnetic (Curie) transitions. As discussed earlier, the saturation magnetization of martensite phase is normally higher than that of the corresponding austenite phase, however these phases are more anisotropic than their cubic counterparts and the rise in specific magnetization at low biasing field with increasing temperature is attributed to the martensite to austenite transformation. The alloy Mn15Fe15 showed three transitions; a rise in magnetization around 250-275K, an intermediate fall in magnetization around 275-325K and final transition to a paramagnetic state 375-440K. In view of the two phase structure these stages show two martensite-to-austenite transformations, Curie transition of the austenite phase and the Curie transformation of the second phase respectively. The martensite transformation temperatures obtained in our thermo-magnetic measurements for the alloys Mn25Fe5 and Mn15Fe15 are comparable to those observed through DSC. The Curie transitions T_c obtained from these measurements are also tabulated in Table 4.9 along with the martensite transformation temperatures from DSC measurements. For the two-phase

alloy Mn15Fe15, a value of 439K is taken where the alloy goes to a completely paramagnetic state. This Curie transition therefore corresponds to the higher of the transition temperatures of the two phases. Such high values are more not commonly reported for Heusler alloys and are expected to be the result of the second phase.

Table 4.9: Transformation temperatures and enthalpies of transformation for the alloys Mn27.5Fe2.5, Mn25Fe5, Mn15Fe15 and Ni45Fe5.

Alloy Designation	e/a ratio #	Curie Temp Tc (K)	Martensite transformation			Austenite transformation temperature		
			Transformation temperature		Enthalpy	Transformation temperature		Enthalpy
			Start (T _{ms}) K	Finish (T _{Mf}) K	ΔH _{A→M} J/g	Start (T _{as}) K	Finish (T _{af}) K	ΔH _{M→A} J/g
Mn27.5Fe2.5	7.897	351	345	328	6.24	342	358	5.99
Mn25Fe5	7.894	382	374	360	8.69	364	382	8.80
Mn15Fe15	7.984	439	261	252	2.57	259	269	2.67
Ni45Fe5	7.726	323	371	356	8.77	367	385	8.46

$$\# (10*\text{at}\% \text{Ni} + 8*\text{at}\% \text{Fe} + 7*\text{at}\% \text{Mn} + 3*\text{at}\% \text{Ga}) / 100$$

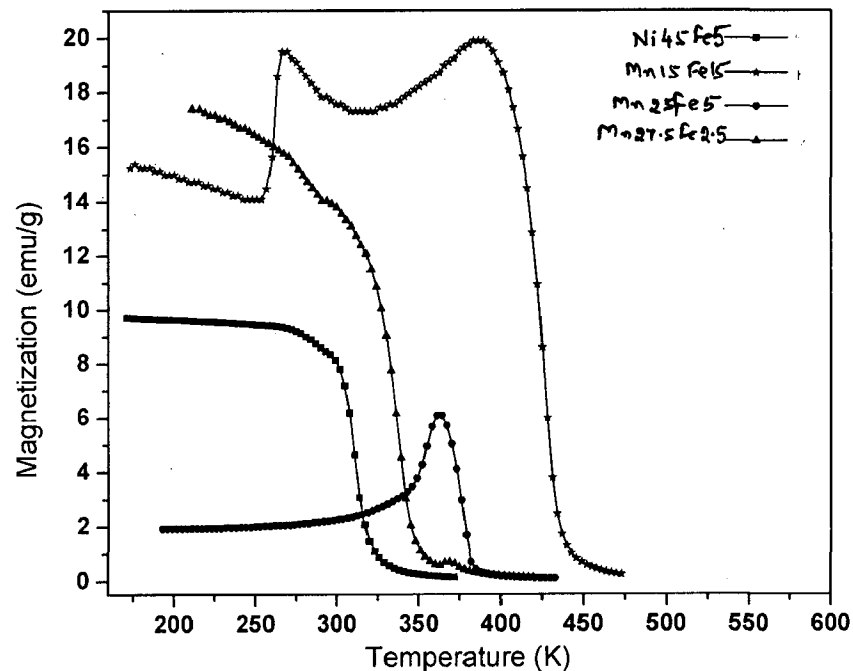


Fig 4.18: Thermo-magnetic measurements for the alloys Mn27.5Fe2.5, Mn25Fe5, Mn15Fe15 and Ni45Fe5.

4.3.4 Room Temperature Magnetization Behavior

Fig 4.19a shows the room temperature magnetization (M-H) curves of the alloys. The alloy Mn25Fe5 shows a two stage behavior in the middle segments in both first and third quadrant of the curve. The alloy Mn15Fe15 with a two phase microstructure showed a little hysteresis, but magnetization behavior is not seen distinctly in the hysteresis curves. The saturation magnetization (M_s) values obtained are 30.66, 33.83, 53.68 and 22.93 emu/g for alloys Mn27.5Fe2.5, Mn25Fe5, Mn15Fe15 and Ni45Fe5, respectively. The room temperature measurements for our alloys are nearer to their Curie temperature. Considering the mixed phase structure and thermal disturbances around Curie temperatures, low temperature measurements below the martensite transformation temperatures were taken at 173K. The results of such measurements are presented in Fig 4.19b. All the curves at low temperatures showed a well defined hysteresis commensurate with the anisotropic martensite phase. The saturation magnetization values at 173K for alloys Mn27.5Fe2.5, Mn25Fe5, Mn15Fe15 and Ni45Fe5 are 47.76, 37.18, 63.92 and 39.29 emu/g respectively.

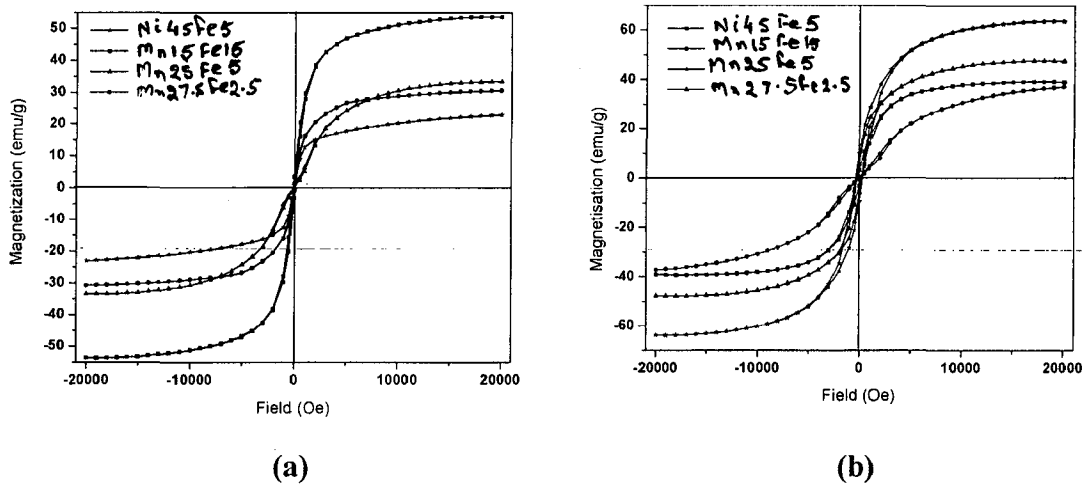


Fig 4.19: The magnetization curves of the alloys Mn27.5Fe2.5, Mn25Fe5, Mn15Fe15 and Ni45Fe5 at a) room temperature and b) at 173K.

4.4 DISCUSSION

The x-ray diffractograms (Fig.4.1, 4.6b and 4.14) with the phases indexed (Table 4.2, 4.4 and 4.7) reveal the room temperature phase structure of the heat-treated alloys investigated. The base composition NMG and the alloys Mn_{27.5}Fe_{2.5}, Mn₂₅Fe₅ and Ni₄₅Fe₅ show non-modulated tetragonal martensite structure. The diffraction pattern for the alloy Ni₄₀Fe₁₀ and Mn₁₅Fe₁₅ show patterns which can be indexed to a cubic structure. The alloy Ni₄₀Co₁₀ has shown a 5M martensite structure alloy. Excepting the alloy Mn₁₅Fe₁₅ with a large Fe replacement, our intended alloy compositions were expected to be in narrow composition range with electron to atom ratio (e/a ratio) between 7.5-7.7. The analyzed compositions with a consistently lower Ga of 17-18 have resulted in the e/a ration of our alloys shifting on a higher side. The various phase structures obtained at room temperature for different alloys shown in Fig 2.19 based on literature data (Soderberg et al 2004) shows modulated martensite in the range of e/a 7.5-7.7 and tetragonal martensite at higher values. The room temperature phase structure obtained for different alloys is therefore consistent and similar to those obtained earlier in literature with similar e/a ratios. It may be noted that though these martensite structures are functions of compositions, they are thermodynamically close and a conversion from one structure to the other may be performed under suitable thermo-mechanical treatments.

The splitting of (222) reflection of martensite phase signifying chemically modulated super-period martensite 5M or 7M structures is not seen for the alloy Mn_{27.5}Fe_{2.5}, though can be noticed on slower scans. The peak splitting is clear at slower scan though reflections did not resolve clearly to confirm the modulated structure. The additional peak position in slower scan matches with that of the secondary phase in case of two-phase alloy Mn₁₅Fe₁₅. Modulated martensite structure in Ni-Mn-Ga systems forms due to thermo-mechanical treatments in suitable compositions. Overlapping reflections in our diffractograms either indicate a transitional stage from a non-modulated to modulated structure or the formation of very fine secondary phase unresolved in microstructure. Chemical composition variations via spinodal reactions during B2' → L2₁ ordering has also been reported in the Ni-Mn-Ga alloys

(Overholser and Wuttig 1999) and may also cause the splitting of reflections. No sinusoidal compositional variations were however seen during compositional analysis of our alloys.

The microstructures of the alloys Ni₄₀Fe₁₀ show presence of a minor second phase but that of Ni₄₀Co₁₀ show single phase alloy (Fig 4.7 and 4.8) in as-cast as well as heat-treated conditions. The presence of an extra reflection in the x-ray diffractograms (Fig 4.6), however confirms the presence of second phase, which may have other peaks overlapping with the major phase. The microstructures for the alloy Ni₄₀Fe₁₀ (Fig 4.7a) have shown streaking marks suggesting erosion of secondary phase during polishing. The γ - Ni is the first crystallizing phase in ternary FMSM Ni-Mn-Ga alloys (Chen et al 2004 a). The secondary soft phase has been reported to be lost as an artifact of mechanical polishing techniques (Chen et al 2004 b). The reflection at 2θ value of 42.95° corresponding to d-spacing of 2.10 \AA not belonging to austenite phase is around the major reflection of γ - Ni phase. The isothermal section of the ternary phase diagram (Fig 2. 12) does not show well defined ternary liquidus lines; however shows shift of the β - phase field towards 2 or 3 phase regions with γ - phase present towards Ni rich side. The γ - liquidus projection line passes over the β - phase field and formation of γ -phase during solidification may be inescapable. In our alloy Ni₄₀Fe₁₀, Fe is substituting for Ni and in reference to the Fig 2.12, the presence of such a phase in our heat-treated alloy is indicative of the shift of the single β - phase field towards two phase field on addition of Fe. A sole reflection however does not permit indexing and is not enough to ascertain the structure of such a phase. The intensity of the extra reflection could be seen as reduced with heat-treatment showing the efficacy of heat-treatment. The series of alloys with Fe replacing Mn have not shown any extra reflection with the exception of alloy Mn₁₅Fe₁₅. The alloy Mn₁₅Fe₁₅ have shown a clear two-phase structure (Fig 4.10c) after heat-treatment with the composition of the matrix Heusler phase as Ni_{49.09}Fe_{10.32}Mn_{19.74}Ga_{20.85} indicating presence of 10.32%Fe in the matrix phase. As these alloys have been water quenched after the heat-treatment at 1073K, the Fe content in the alloy does not show the room temperature equilibrium value and Fe-content in this phase may have been retained from that of solubility around 1073K. It may be noted that ternary Ni-Mn-Ga alloys are reported with a spinodal type

solvus line in pseudo-binary $\text{Ni}_{50}\text{Mn}_{25+x}\text{Ga}_{25-x}$ system (Overholser and Wuttig 1999). The second phase in microstructure of our heat-treated alloy Mn15Fe15 does not appear with features of a nucleation and growth process, but as if through phase separation. The solvus line in the pseudo-binary phase diagram $\text{Ni}_{50}\text{Mn}_{25+x}\text{Ga}_{25-x}$ system in literature can be construed as a vertical cross-section of solvus surface for quaternary Ni-Fe-Mn-Ga phase diagram. This surface appears to be extending around the solvus line in the pseudo-binary diagram in literature and hence causing two-phase structure in our alloy Mn15Fe15. Our alloy compositions Mn27.5Fe2.5, Mn25Fe5 and Ni45Fe5 therefore are within single phase field region. The alloy Mn15Fe15 is a two phase alloy and the alloys Ni40Fe10 and Ni40Co10 appear to be on the boundary of single phase field.

The phase structure and the lattice parameters of the phases indexed in the light of the above discussion have been tabulated in Table 4.10. The obtained room temperature phase structures are commensurate with the martensite transformation temperatures estimated through the DSC and thermo-magnetic measurements.

Table 4.10: Room temperature phase structure, lattice parameters and the electron to atom ratios of heat treated alloys.

Alloy	Room Temperature Phase structure	Lattice parameters		Unit cell Volume (\AA^3)	Electron to atom ratio e/a for	
		a (\AA)	c (\AA)		intended compositions	analyzed compositions
NMG	Martensite T	7.73	6.59	393.86	7.70	7.845
Ni40Fe10	Cubic $L2_1$	5.83	5.83	198.15	7.5	7.74
Ni40Co10	5M Martensite	5.86	5.56	190.92	7.6	7.64
Mn27.5Fe2.5	Martensite T	7.75	6.55	393.40	7.725	7.897
Mn25Fe5	Martensite T	7.74	6.56	392.99	7.75	7.894
Mn15Fe15	Cubic	6.00	6.00	216.00	7.85	7.984
	Second phase	--	--	--		--
Ni45Fe5	Martensite T	7.74	6.60	395.39	7.6	7.726

The lattice parameters of stoichiometric Ni₂MnGa alloy with cubic structure are reported as 5.8636Å at 400K in paramagnetic state and 5.8229Å at 300 K in ferromagnetic state (Brown et al 2002) giving a unit cell volume of 201.60Å³ at room temperature. For ternary compositions near our base composition, the room temperature alloys are in normally martensite phase structure. A value of 197.19 Å³ for the unit cell volume is reported for a 5M martensite in a ternary Ni_{50.1}Mn_{29.1}Ga_{20.8} alloy (Richard et al 2006). The base alloy NMG has been indexed to a martensite structure with a cell volume of 393.86 Å³. The lattice parameter values for tetragonal obtained here are in the range obtained for ternary alloys in the literature (Jiang et al 2003)

The thermo-magnetic (M-T) measurements have been employed for identification of both structural martensite transformation as well as magnetic Curie transition. While rise of magnetization with increasing temperature indicate structural changes, the fall is attributable to paramagnetic (Curie) transitions. A small rise in the transformation temperature is noticed on heat treatment in case of alloy Ni₄₀Fe₁₀. The additional peak in x-ray diffraction patterns for these alloys indicated a possibility of trace phases lowering down with heat-treatment. The small change in transformation temperatures is can be attributed to homogenization and compositional change coupled with lowered second phase quantity. The fall in magnetization on Curie transition is almost identical in as cast and heat-treated alloys. The observation is consistent with reports (Chu et al 2001) that martensite transformation is more sensitive to the thermal processing than Curie temperatures. It may be pointed out that the other magnetic property viz. saturation magnetization for these alloys improved after heat-treatment. This increase is attributed to a reduction in the relative quantity of the secondary paramagnetic phase (fig 4.6) as well as compositional changes during heat-treatment. The Ni₄₀Co₁₀ alloy did not show any rise due to martensite transformation thermo magnetic M-T measurements as seen in case of Fe containing alloys. Some measurements have therefore been carried out at a higher biasing field of 1000 Oe to enlarge the magnetic response. The M-T measurements did not show changes due to structural transformations in either case. The room temperature structure of a martensite suggests a martensite transformation higher than room temperature. If the austenite and the martensite have a comparable magnetization at the biasing fields, a lower

difference in magnetization may not show any signature of the transition in the thermo-magnetic curves. It may be noted that the Co containing alloy did not show any clear peak area in DSC measurements also but two slope changes or kinks. The kink at 481 K in DSC plots corresponds to the curie transition and matches well with the observed curie transition in M-T measurements for the alloy. The transition at 361 K in heating and 364 K in cooling cycle appears to be due to the martensite transformation. The absence of clear demarcated area may be due to absence of a finish point or a low enthalpy. Low enthalpy changes in DSC can appear as change in slope. The magnetic transition temperature is reported to rise with addition of Co whereas the martensite temperature falls (Khovailo 2003 a). The observed transition temperatures are in line with the reported trends.

The DSC thermo-grams showing the exotherms during cooling and endotherms during heating cycles (Fig 4.10) are attributed to structural martensite transformation and reverse transformation to austenite, respectively. The martensite transformation temperatures increase from alloy Mn_{27.5}Fe_{2.5} to alloy Mn₂₅Fe₅ i.e. from 2.5 % Fe to 5 % Fe in line with increasing e/a ratio. These values are lower for alloy Mn₁₅Fe₁₅. In addition, alloy Mn₁₅Fe₁₅ showed a transformation enthalpy value 2.67 J/g much lower than the other alloys. In view of the two-phase structure of the alloy, this value appears to be lowered due to contributions of transformation enthalpy from only one of the two phases. Extended thermal scans up to the instrument limits (673K) were carried out and did not however reveal the transformation peaks for the second phase.

The martensite transformation in NiMnGa Heusler alloys occurs at an average valence electron concentration of approximately 7.3 (Schlagel et al 2000). The martensite transformation occurs when the Fermi surface touches the Brillouin zone boundary, the change in number of valence electron and alteration in Brillouin zone boundary affect the martensite transformation temperature (Entel et al 2006). Considering the outermost electrons of the constituent elements, the average number of valence electron per atom or electron to atom ratios can be given as (Chernenko 1999),

$$e/a = \frac{10 \times (\text{Ni at}\%) + 8 \times (\text{Fe at}\%) + 9 \times (\text{Co at}\%) + 7 \times (\text{Mn at}\%) + 3 \times (\text{Ga at}\%)}{100} \quad (4.1)$$

In view of the importance of e/a ratio, the transformations in ternary as well as quaternary Ni-Mn-Ga alloys are often analyzed in terms of the e/a ratio. For example, Fig 2.21 in chapter 2 presents the information in terms of e/a ratio for Ni-Mn-Ga alloys with small addition of Fe, Co. In our study, only one composition has been made with Co and for one to one comparison, the crystal structure data excluding Ni₄₀Co₁₀ alloy from Table 4.9 is presented in Fig 4.20a as a function of e/a ratio. In view of the two-phase structure of the alloy Mn₁₅Fe₁₅ the Fe content of the matrix phase has been taken into account instead of the average composition. Our alloys have shown different structures at different compositions. All the data points however have been plotted together for the sake of comparison. While the data points in lower portion of the graph with lattice parameters around 5Å show a cubic or the modulated structure, upper portion of the graph pertains to the tetragonal martensite phase. With 10, 8 and 7 electrons per atom for Ni, Fe and Mn, the e/a ratio has perceptible change only when Fe replaces Ni in intended composition. For Fe replacing Mn, a small change in e/a ratio for our alloys has got compensated to a large extent in the compositional variation and our alloys with Fe substituting for Mn (Mn_xFe_y alloys) have e/a ratios falling in very narrow range. The small variation in e/a ratios has however resulted in large variations in the crystallographic parameter and is seen as a random scatter in Fig 4.20a. The same information is therefore re-plotted in Fig 4.20b with respect to atom % Fe and shows clear trends in the experimental data. The tetragonal martensite phase is formed at lower Fe content up to about 6 atom % and a cubic structure is favored at higher Fe-additions. The cell volume of the cubic phase falls with the increasing Fe content. For the cubic structure, more compact cell with Fe addition is suggestive of the Fe placement at the sites occupied by larger atoms. It may be pointed out here that the atomic sizes of constituent atoms in Ni-Mn-Ga alloys decrease from Ga to Mn to Ni (1.81, 1.79 and 1.62Å for atomic radii and 1.17, 1.17 and 1.15 Å for covalent radii respectively).

The martensite transformations usually are athermal transformations and should occur thermodynamically at a temperature T_0 where the parent and martensite phase have equal free energies. The transformation in case of austenite to martensite transformation however requires nucleation of the martensite phase. Such nucleations in turn include a surface energy and elastic strain energy terms for free energy expression. The composition dependent chemical free energy term therefore require correction for these aspects and the thermodynamic equilibrium temperature T_0 is therefore taken as the mean of T_{MS} and T_{Af} thus annulling the effect of other free energy terms (Otsuka and Wayman 1998). The T_0 plots with e/a and Fe content are presented in Fig 4.21. As noticed with the variations for the lattice parameters, T_0 and T_C are comparable for up to ~ 6 Fe% additions. The Ni-Mn-Ga alloys with 50:30:20 alloys show such coupled transformation desirable for the FMSM phenomenon (Singh et al 2008). It may be noted that the Curie transition has been measured through M-T plots and at higher Fe additions the values shown are for phase with higher T_c and no definitive comments can be made for variation of the T_c for the matrix phase with cubic structures.

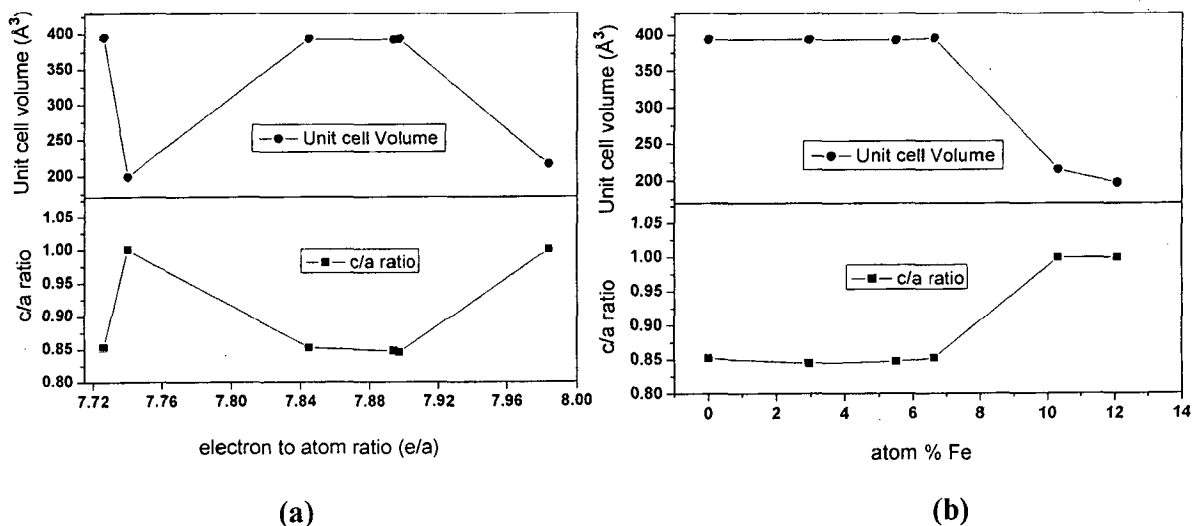


Fig 4.20: Variation of lattice parameters of Fe containing alloys (a) with respect to electron to atom ratio and (b) with respect to atom %Fe

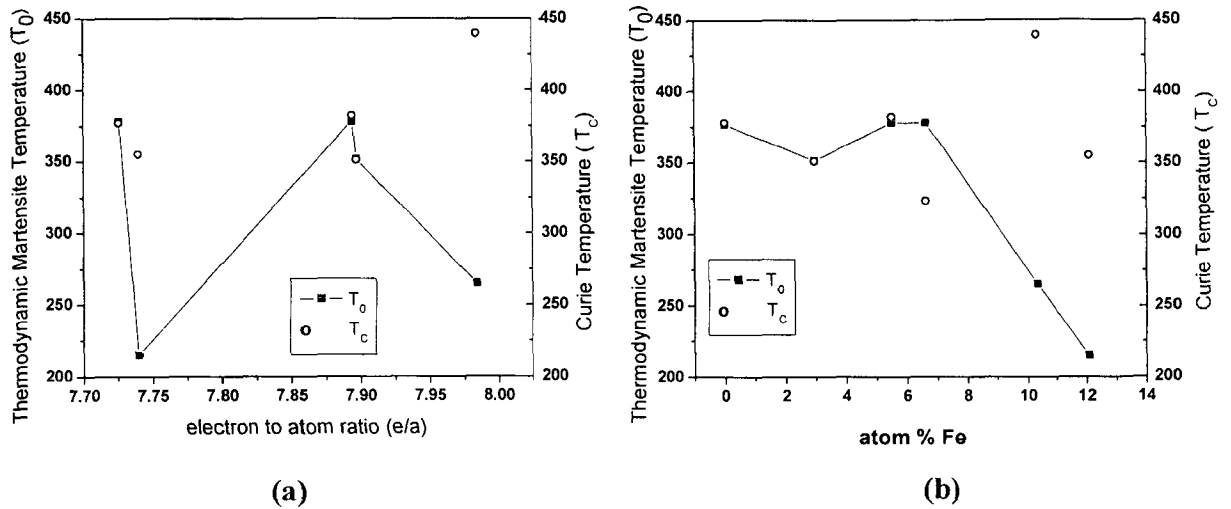


Fig 4.21: Variation of transformation temperatures T_0 and T_c for Fe containing alloys (a) with respect to electron to atom ratio and (b) with respect to atom %Fe. The T_c values at higher Fe-levels are for two-phase alloys and indicate higher of the two T_c 's

The recent studies on the ternary Ni-Mn-Ga alloys have shown that martensite transformation temperatures are dependent also on the ordering of the constituent atoms, which in turn depends on the heat-treatment temperatures (Segui et al 2007, Sanchez-Alarcos et al 2008). Lower heat-treatment temperatures favor the ordering and thus the improved martensite transformation temperatures. The heat treatment schedule for the former two alloys i.e Ni40Fe10 and Ni40Co10 in the table 4.9 have been high temperature homogenization, whereas the latter alloys viz. Mn27.5Fe2.5, Mn25Fe5, Mn15Fe15 and Ni45Fe5 have been imparted a different treatment to include an ordering treatment at 1073K/ 48h. This also could have been a cause for the lower martensite transformation temperature for the alloy Ni40Fe10. In absence of actual density of state measurements for our alloys, lower martensite transformation temperature in spite of a reasonably higher e/a ratios for the alloy Ni40Fe10 need to be explored further in detail.

Different techniques have been applied in literature to understand the site occupancy of atoms in Ni-Mn-Ga alloys. The stoichiometric alloys Ni₂MnGa has L2₁ structure (Fm $\bar{3}$ m) at higher temperature with unit cell showing four formulae unit with 8 Ni-atoms at centers of the quartets and Mn & Ga-atoms arranged alternating at the edges. Martensite structures have

been derived from the $L2_1$ structure in tetragonal or orthorhombic systems for various modulated/ non modulated martensite structures (Brown et al 2002). X-ray diffraction patterns for Mn-rich $Ni_{1.95}Mn_{1.19}Ga_{0.86}$ super-period 5M martensite phase have been fitted using Rietveld refinement (Righi et al 2007). The similar atomic scattering factors for Ni and Mn atoms did not allow the distinction between Ni and Mn atoms and fitting was reported using $Ni_2Mn_{1.15}Ga_{0.85}$ composition on monoclinic I2/m basis fitted in the near orthorhombic cell with Ni- atoms at 4h, Mn-atoms at 2a and Ga-atoms at 2d sites and excess Mn-atoms at 2d Ga-sites. This report thus indicated the presence of excess Mn atoms at Ga sites in Mn-rich off-stoichiometric $Ni_{50}Mn_{30}Ga_{20}$ alloys.

In view of our alloys with Fe additions we have employed Mössbauer technique for identification of Fe – sites through the Fe-spectrum. The Mössbauer spectrum of elemental ferromagnetic Fe shows a hyperfine field 33.0 T ($2.2 \mu_B$ per Fe atom) (Hanna et al 1960). Ternary Ni_2MnGa alloys show a magnetization of $4.13 \mu_B$ per Mn atom with only $0.30 \mu_B$ contribution per Ni atom (Kudryavtsev et al 2002). Ni_2MnGa structure with 2atom% ^{57}Fe added for Ni, Mn and Ga in the formulae reported values of ^{57}Fe hyperfine field for at the sites at room temperature as 8.6, 14.6 and 14.5 T respectively (Mitros et al 1987), thus suggesting the ferromagnetic environment for Fe atoms at Ni-, Mn- and Ga- sites. It may be noted that there was no additional confirmation if the Fe- atoms were indeed placed at intended substitution site. The study nevertheless suggested ferromagnetic sextets of two different ranges 8.4 and ~ 14.5 T. The ferromagnetic spectra in our present study shown in Fig 4.10 and 4.16 also show two types of the sextets with the set of smaller values 8.2 and 9.5 T. A value of 17-19 T for Mn_xFe_y alloys and 29.3 T for $Ni_{40}Fe_{10}$ alloys are obtained. With the Heusler alloys formulae X_2YZ , the atomic sites are indicated as X, Y or Z sites for the Ni, Mn or Ga sites respectively. The hyperfine fields of the sextets fall in two broad categories: the higher values in the range 17-19T in the alloys investigated including the single phase ones showing one sextet and the lower values of 8.2 and 9.5 T are observed for the second sextet in alloys $Mn_{15}Fe_{15}$ and $Ni_{45}Fe_5$ respectively. The higher set of values (17-19T) compared to 33.0 T ($2.2 \mu_B$ per Fe atom) for pure Fe (Hanna et al 1960) signifies the presence of Fe at atomic sites in predominantly ferromagnetic environment. The paramagnetic sub-spectrum (Fe intensity ratio) for $Mn_{27.5}Fe_{2.5}$, $Mn_{25}Fe_5$ and $Mn_{15}Fe_{15}$ showed 82%, 54%

and 50% paramagnetic contributions. These values were 70% and 8% for Ni₄₅Fe₅ and Ni₄₀Fe₁₀ alloys. It may be noted that if an Fe atom is placed at any of the X, Y and Z-site, the atom is surrounded by a reasonable number of ferromagnetic atoms, the highest ferromagnetic neighbors being for the Z-site. Presence of Fe atoms in both ferro and paramagnetic environments have been reported earlier in case of Heusler alloys and have been explained as paramagnetic clusters in the solid solutions not visible to diffraction (Block et al 2003) or due to a spread in relaxation times of Fe atoms in chemically single phased alloys (Lakshmi et al 2002). As discussed earlier, the Y site atom is the major contributor to the magnetization of the Heusler alloys with X and Z site contributing negligibly to the magnetization. A large hyperfine field value of 17-19T is definitely indicating the presence of Fe atoms in sites contributing ferromagnetically and in our context mean Y or Mn site. With 5% Mn-atoms placed at Y as well as Z sites in case of Ni₅₀Mn₃₀Ga₂₀ alloy (Righi et al 2007), the Fe additions also could have gone to both the sites. If the Fe atoms are placed Ga site as well as neighboring Mn sites, such a cluster of Fe can result in the paramagnetic contribution from Fe atoms. The Ga atom being the largest atom, the initial Fe-atoms are placed at Ga sites as can be noticed by smaller lattice volume of alloy Mn_{27.5}Fe_{2.5} over the alloy NMG. Further Fe additions of are placed at ferromagnetic Mn sites and the paramagnetic contributions accordingly reduce. In addition, a paramagnetic state for the Fe-atoms at room temperature shows exchange interaction of the nature which reduces the Curie temperatures. Increased gallium additions are reported to lower Curie temperature in ternary Ni-Mn-Ga alloys (Singh et al 2008) and hence support the conjecture that Fe is placed at Ga-sites. .

The Ni₄₀Fe₁₀ alloy showed ferromagnetic spectrum with hyperfine field of 29.3 T (1.95 μ_B). The manganese being the primary contributor to magnetic moment in Ni₂MnGa alloys and with high hyperfine field values of Fe in our alloy, the Fe added may have gone to manganese site contrary to the intended objective of nickel substitution in L2₁ phase. For the Fe additions substituting for Mn, our Ni₅₀Fe_xMn_{30-x}Ga₂₀ alloys for $x \leq 5$ should place themselves at Mn- or Ga-sites by analogy with reports for ternary Ni₅₀Mn₃₀Ga₂₀ alloy (Righi et al 2007). Alloy Mn_{27.5}Fe_{2.5} and Mn₂₅Fe₅ have shown single phase structures and the x-ray diffractograms for these alloys are indexed to tetragonal martensite structure. The extra reflections in diffractogram for the alloy Mn_{27.5}Fe_{2.5} with 2.5 % Fe however are not

reported in case of studies on ternary $\text{Ni}_{50}\text{Mn}_{30}\text{Ga}_{20}$ alloys. Their presence and subsequent annulment at 5% Fe suggest a more random presence of Fe atoms at different atomic sites at higher Fe concentrations. The Mössbauer spectra for these alloys have shown two sub-spectra for presence of Fe in ferromagnetic as well as paramagnetic environment indicating the two co-existing magnetically different environment for iron in the single phase of the $\text{Mn}_{27.5}\text{Fe}_{2.5}$ and $\text{Mn}_{25}\text{Fe}_5$ alloys. But in alloy $\text{Mn}_{15}\text{Fe}_{15}$, there are three different sub-spectra of Fe, two sextets and one doublet, corresponding to three different environments. Two sextets could come from the two different phases and the doublet may come from positions where Fe could occur as distant magnetic clusters separated from each other so that there is no exchange interaction between them resulting either in long range or short range. Chemical ordering in Heusler Ni-Mn-Ga alloys is reported causing spinodal type compositional variations (Overholser and Wuttig 1999) and could have resulted phase separations in our alloy $\text{Mn}_{15}\text{Fe}_{15}$. The presence of two ferromagnetic spectra in case of single phase alloy $\text{Ni}_{45}\text{Fe}_5$ however shows that a small placement of the Fe atoms at the third site viz. X or Ni sites. The hyperfine field of 9.5 T for the alloy is comparable to the reported value of 8.6 T for $\text{Ni}_{48}^{57}\text{Fe}_2\text{Mn}_{25}\text{Ga}_{25}$ alloys (Mitros et al 1987) and shows a small presence of Fe atoms at Ni site also. It appears that with addition of Fe, it primarily goes to substitute Mn in original Ga sites of L_{21} structure. On further increase of Fe, it goes to substitute Mn from the original Mn sites of L_{21} structure.

Saturation magnetization of our alloys has been measured at room temperature and for some alloys at lower temperatures for comparison in similar crystal structure. The experimental values obtained are plotted as a function of atom % Fe in Fig 4.22. Room temperature saturation magnetization values obtained at a maximum magnetic field of 12 kOe for as-cast and annealed $\text{Ni}_{40}\text{Fe}_{10}$ alloys in L_{21} structures 59.0 and 62.8 emu/g respectively are obtained. The alloy $\text{Ni}_{40}\text{Co}_{10}$, in martensitic state at room temperature, has shown a saturation magnetization of 88 emu/g for both as-cast and heat-treated conditions. The room temperature magnetization value in the Co containing alloy is higher than that for cubic Fe containing alloy. The saturation magnetization is normally higher for the martensite phase and a one to one comparison between the alloys is not possible. A large increase of 26emu/g i.e. from 62.8 emu/g for $\text{Ni}_{40}\text{Fe}_{10}$ alloy to 88 emu/g for $\text{Ni}_{40}\text{Co}_{10}$ alloy needs to be looked beyond

structural changes into from the individual atomic contributions. The saturation magnetization of the ferromagnetic shape memory Heusler alloys falls on the known Bethe-Slater plot only if all outer electrons are counted, i.e. $\langle s + p + d \rangle \approx 10$ (Wuttig et al 2000, Wuttig et al 2001). With a magnetization of $4.13 \mu_B$ per Mn atom with only $0.30 \mu_B$ contribution per Ni atom in ternary Ni_2MnGa (Kudryavtsev et al 2002), it is reasonable to assume that large increase in magnetization results from the increased contributions from added Co as well as from increased contributions from Mn. Such improved magnetic exchanges are reflected in improved Curie temperatures of the alloys.

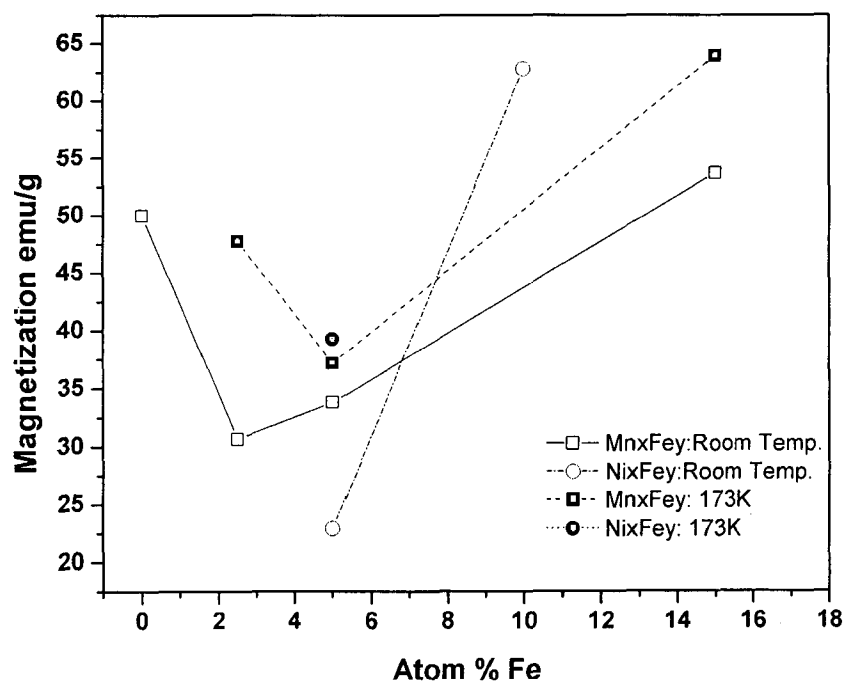


Fig 4.22: The saturation magnetization of Fe containing alloy at RT and 173K

The reported magnetization value for stoichiometric Ni_2MnGa alloy with $L2_1$ structure is 64 emu/g (Jin et al 2002). In ternary $Ni_{50}Mn_{30}Ga_{20}$ alloy, Mn is pushed to Ga sites in $L2_1$ structure (Righi et al 2007) and there is a lowering of magnetization to $\sim 50 \text{ emu/g}$ (Murray et al 1988) compared to that in stoichiometric alloy. Thus, there is a lowering of magnetic moment when Mn is pushed to Ga-site. It may be noted that the magnetic

contribution from Ga is reported to be $-0.05 \mu_B$ (Kudryavtsev et al 2002). Even though Ga atom does not possess unpaired electrons, assignment of a negative value to Ga atom shows the anti-ferromagnetic coupling between the Mn-Ga sites in the stoichiometric Ni_2MnGa alloy. Lower magnetization may result from either modification of the inter-atomic distances or such negative contributions. Initial addition of Fe in our study shows a reduction in magnetization values and on subsequent addition of Fe the magnetization increases again. As discussed earlier, the magnetization in Heusler alloys is reported to be due to localized moments of Mn atom, with negligible contributions from other atoms. Pure iron possesses a magnetization of $2.2\mu_B$ per Fe atom and a contribution $\sim 1.95 \mu_B$ per Fe atom measured through Mössbauer spectrum (Fig 4.10) suggests a lower contribution from Fe atom at Mn site. Even though iron contribution is lower, increased saturation magnetization of the alloy $Ni_{40}Fe_{10}$ with Fe addition suggests an improved exchange interaction at Mn sites or the modified inter-atomic spacing at Mn site. Co addition is known to improve the magnetic transition temperature in many permanent magnet alloy systems by improving the exchange interactions (Strnat 1988). Higher magnetization for Co containing alloys is indicative of improved exchange interaction between manganese atoms and is consistent with higher Curie temperatures obtained in these alloys. The room temperature saturation magnetization (M_s) values obtained for alloys Mn_xFe_y alloys are lower than that obtained for the alloys $Ni_{40}Fe_{10}$ and $Ni_{40}Co_{10}$. It may however be noted that the room temperature measurements for these alloys are nearer to their Curie temperature. Considering the mixed phase structure in case of alloy $Mn_{15}Fe_{15}$ and thermal disturbances around Curie temperatures, low temperature measurements below the martensite transformation temperatures were taken at 173K. The saturation magnetization values at 173K for alloys $Mn_{27.5}Fe_{2.5}$, $Mn_{25}Fe_5$, $Mn_{15}Fe_{15}$ and $Ni_{45}Fe_5$ are 47.76, 37.18, 63.92 and 39.29 emu/g respectively. The alloys $Mn_{25}Fe_5$ and $Ni_{45}Fe_5$ both containing 5 at% Fe have shown comparable magnetization, with alloy $Mn_{25}Fe_5$ showing a slower magnetization rate and thus higher anisotropy. The magnetization value for the alloy $Mn_{15}Fe_{15}$ is for a two phase structure and these results therefore indicate a fall in magnetization when Fe is increased from 2.5 % to 5%. As discussed earlier, an increase in room temperatures magnetization has been noticed in our

alloys with Fe/Co substitution for Ni. A fall in magnetization here is indicative of placement of the additive elements at a different site in the structure. Dependence of the magnetization in a ternary $\text{Ni}_{49.5}\text{Mn}_{28.5}\text{Ga}_{22}$ with ordering levels at the Mn-sub lattice has been recently reported (Sanchez-Alarcos et al 2008)

Our studies, therefore, show that while addition of Co increases the Curie transition and also results in formation of a modulated martensite structure at room temperature, both thermal or thermo-magnetic measurements have not revealed any significant change in enthalpy or magnetization between austenite and martensite phases. It is therefore not possible to make any definitive conclusions about the beneficial role of Co addition in the context of FMSM behaviour. The improvement in Curie temperatures may however be exploited with Co-additions in conjunction with other elements. The magnetization values obtained for the alloys containing Co are higher than ternary Ni-Mn-Ga alloys signifying improved magnetic exchange interaction between the Mn and Co atoms.

For compositions aimed to replace either Ni or Mn by Fe, the magnetization improves with increased Fe additions, though Fe atoms appear to substitute an extent of Ga sites as well. The structural and magnetic transformations remain coupled i.e. $T_c \sim T_M$ up to about 6%Fe. The transformation temperatures, however, are modified according to the occupation of Fe at different sites. While initial placement of Fe at Ga sites lowered these temperatures, at higher levels placement at Mn sites improved these temperatures again. Fe additions beyond ~6% results in decoupling of the two transformations and also, results in second phase formations. Such decoupling may limit the exploitation of the alloys as FMSM alloys. However, addition of both Fe and Co may offer a better alloy from the standpoint of FMSM applications.

RESULTS AND DISCUSSION: ALLOYS WITH ADDITIONS INTENDED FOR Ga

This chapter describes preparation and characterization of the quaternary alloys with elemental additions intending to partially replace Ga in $\text{Ni}_{50}\text{Mn}_{30}\text{Ga}_{20}$ (NMG) base composition. Two types of replacements were made; one of trivalent elements Al and B on valency parity with Ga and the other of large rare earth elements intending to replace Ga as the largest atom in the ternary alloys. The results obtained for the ternary base composition NMG have already been presented in section 4.1. The results obtained for alloys with of Al/ B substitutions for Ga are presented here first. Rapid quenching technique has been employed as an alternate processing technique for these alloys to stabilize alternate metastable martensite phases. The results of rare earth Sm/Dy additions for Ga are presented next. The results obtained are analyzed in terms of the chemistry as well as processing technique for the alloys.

5.1 RESULTS OF STUDIES FOR $\text{Ni}_{50}\text{Mn}_{30}\text{Ga}_{15}\text{Al}_{5-x}\text{B}_x$ ALLOYS WITH INTENDED REPLACEMENT FOR Ga BY Al/B

5.1.1 Chemical Composition of Alloys

Alloy compositions $\text{Ni}_{50}\text{Mn}_{30}\text{Ga}_{15}\text{Al}_{5-x}\text{B}_x$ ($x=0, 1$ and 4) were prepared with the aim to replace 5% Ga with Al and boron in the base composition $\text{Ni}_{50}\text{Mn}_{30}\text{Ga}_{20}$ (Alloy NMG: section 4.1). The alloys are designated as Ga15Al5, Ga15Al4B1 and Ga15Al1B4 based on the scheme defined in section 3.1. The alloys were prepared by repeated arc melting. The as-cast alloy Ga15Al5 was cut and heat-treated with heat-treatment1 (1273 K for 3 hrs in a vacuum furnace and gas quenched). Alloys Ga15Al4B1 and Ga15Al1B4 were heat-treated in sealed evacuated quartz ampoules with heat-treatment2 (1273 K for 72h and 1073K for 48h in a vacuum furnace and water quenched). The nominal composition and analyzed compositions of the heat-treated alloys are shown in table 5.1.

Table 5.1: Nominal and analyzed compositions of the heat-treated Ni-Mn-Ga-Al-B alloys

Alloy Designation	Nominal Composition					Analyzed Composition									
	Atom %					Wt%					Equivalent Atom %				
	Ni	Mn	Ga	Al	B	Ni	Mn	Ga	Al	B	Ni	Mn	Ga	Al	B
Ga15Al5	50	30	15	5	0	49.91 ±0.19	29.80 ±0.16	17.65 ±0.22	2.64 ±0.09	-	48.76	31.11	14.52	5.61	0
Ga15Al4B1	50	30	15	4	1	50.14 ±0.29	29.54 ±0.43	18.8 3±0.26	1.44 ±0.03	0.145 ±0.001	49.41	31.11	15.62	3.09	0.77
Ga15Al1B4	50	30	15	1	4	51.21 ±0.71	29.79 ±0.26	19.61 ±0.16	0.11 ±0.002	0.361 ±0.01	50.33	31.29	16.22	0.24	1.92

5.1.2 Structural Characterization of the Alloys

Fig 5.1 (a) and (b) shows the BSE images of the as cast and heat-treated Ga15Al5 alloy. The cast dendritic structure in as cast condition is broken down to a homogeneous structure by heat treatment. The homogeneity of the structure was ascertained through EPMA of the heat-treated alloy (Fig 5.1(c)). The x ray diffractograms under the two conditions (Fig 5.2) show the crystal structure to be modulated 5M martensite structure as observed in Fe/ Co containing alloys (Table 4.4 and 4.7) under both the conditions, but there is an un-indexed reflection (marked with * in Fig 5.2) showing the presence of secondary phase in cast structure. In addition to EPMA results, the absence of the extra reflection in heat-treated alloy indicates the homogeneity obtained in the alloy by heat treatment.

The BSE images for the heat-treated Ga15Al4B1 and Ga15Al1B4 alloys are shown in Fig 5.3. In addition to the matrix phase, these alloys show presence of secondary phases. The microstructures show a darker phase and a grayish phase distributed in the matrix. However, it is not clear whether the darker phase has resulted from ploughing out of the grayish phase during polishing. Considering the nature of contrast in BSE images as the atomic number contrast, the low atomic number elements *viz.* Al/B in the alloys may have gone to the matrix phase. However, the relative quantity of the secondary phases is relatively higher in alloy Ga15Al1B4 containing higher boron. Thus, the alloys containing boron are multi-phase alloys unlike the boron free alloy Ga15Al5.

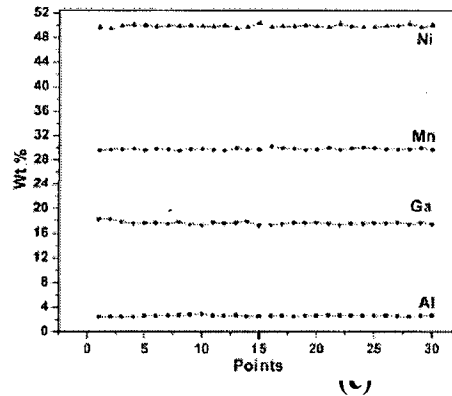
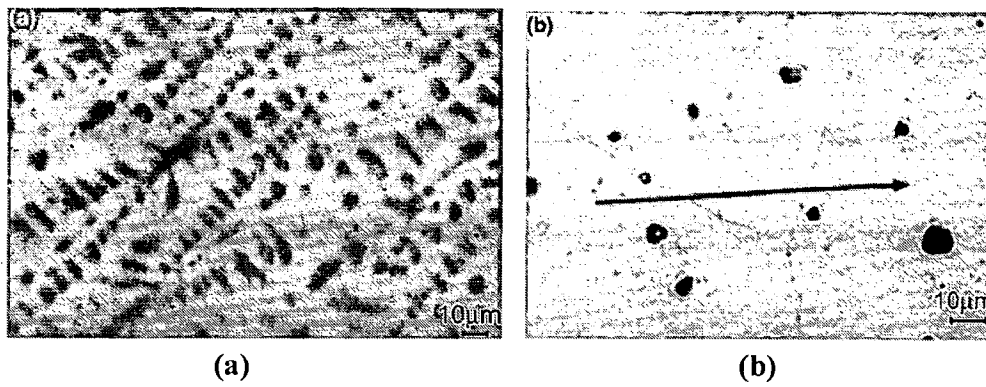


Fig 5.1: Backscattered electron image of (a) as-cast and (b) heat-treated Ga15Al5, along with EPMA analysis for constituent elements for heat-treated alloys (along the arrow), showing uniform distribution of elements.

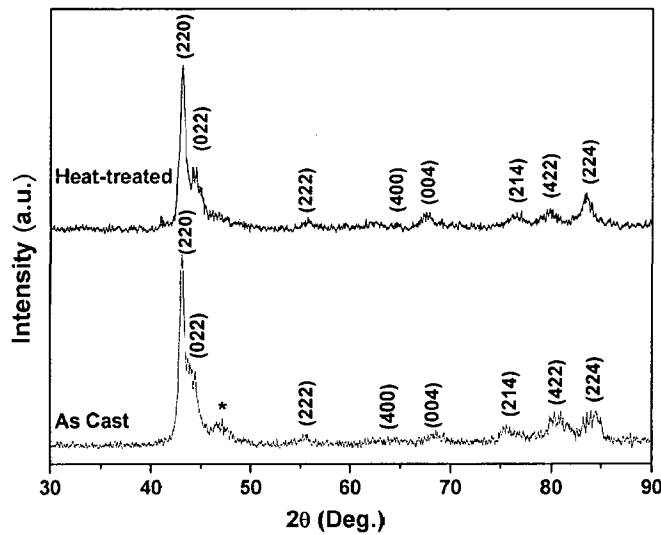


Fig 5.2: The x-ray diffractograms of the as cast and heat-treated Ga15Al5 alloy

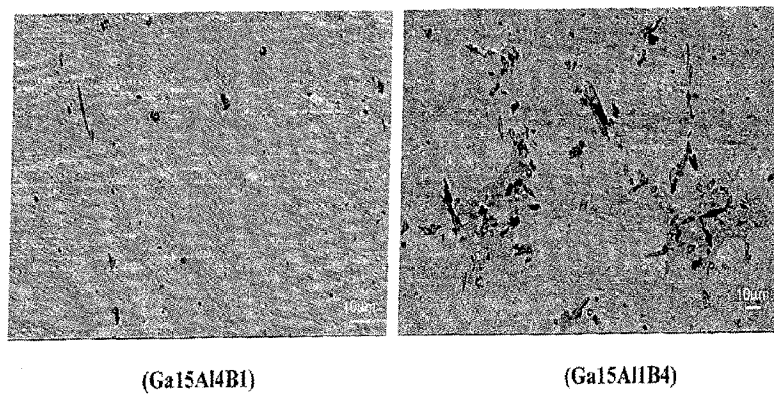


Fig 5.3 The BSE images for the alloys Ga15Al4B1 and Ga15Al1B4.

The x-ray diffraction patterns obtained from the heat treated alloys, Ga15Al4B1 and Ga15Al1B4, are shown in Fig 5.4. While both the Ga15Al4B1 and Ga15Al1B4 alloys have shown presence secondary phase but the diffraction pattern for these alloys could be indexed to a non-modulated tetragonal martensite structure. No un-indexed peaks could be observed possibly due to overlap of the stronger peaks of the secondary phase with those of the indexed tetragonal matrix phase. The peak positions and the peak assignment for these diffraction patterns to different martensite phases are provided in Table 5.2 and the corresponding values for boron free alloy Ga15Al5 with modulated martensite phase have been shown comparison with alloys containing boron. The peak broadening increases considerably for the higher boron alloy. The marked peak positions show the structure to be the similar to that with low boron alloy Ga15Al4B1 with a very small shift to higher angle side with increasing boron.

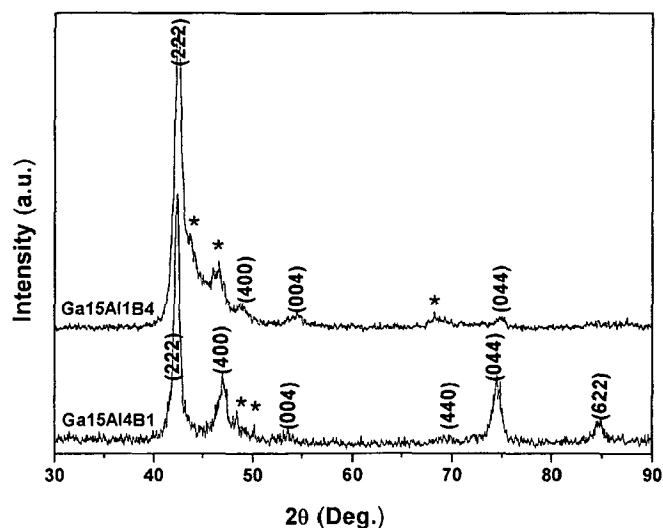


Fig 5.4: The X-ray diffractograms of the heat-treated Ga15Al4B1 and Ga15Al1B4 alloys

Table 5.2: The assignment of the x-ray diffractogram peaks for heat-treated Ga15Al5, Ga15Al4B1 and Ga15Al1B4 alloys to various phases

Peak Position						Reflecting plane	
Ga15Al5		Ga15Al4B1		Ga15Al1B4		5M martenite	Tetragonal Martensite
2θ (deg)	d-spacing (Å)	2θ (deg)	d-spacing (Å)	2θ (deg)	d-spacing (Å)	(hkl)	(hkl)
		42.22	2.138	42.38	2.130		222
43.03	2.099					220	
44.29	2.043					022	
		46.85	1.937	46.56	1.948		400
		53.39	1.714	54.65	1.680		004
55.79	1.646					222	
64.76	1.438					400	
67.5	1.386					004	
		69.43	1.352	68.05	1.376		440
		74.59	1.271	74.85	1.267		044
79.92	1.199					422	
83.37	1.158					224	
		84.6	1.144				622

5.1.3 Transformation Characteristics of the Alloys

The DSC thermograms of the alloys are presented in Fig 5.5. The transformation temperatures observed from the thermograms are compiled in Table 5.3. The thermogram of alloy Ga15Al5 show two exotherms during cooling cycle and two endotherms during heating cycle. Only one transformation has been noticed for the alloys Ga15Al4B1 and Ga15Al1B4. The transformation temperatures have increased with the increased boron in the alloys. The alloy with high boron *viz.* Ga15Al1B4 showed a large thermal hysteresis of ~90K.

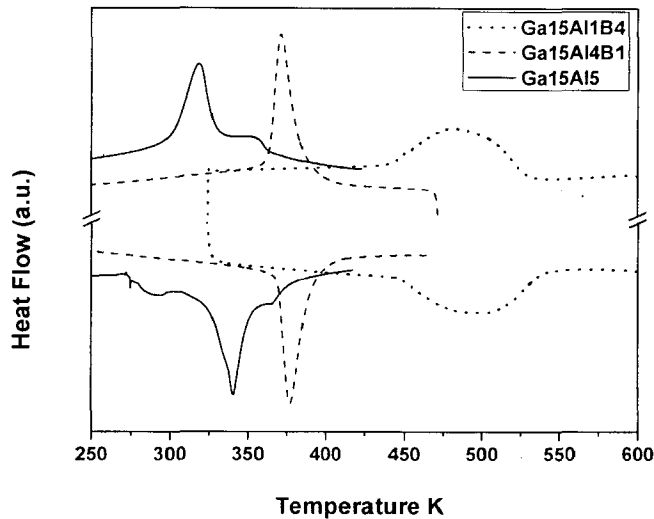


Fig 5.5: The DSC thermograms for the Ga15Al5, Ga15Al4B1 and Ga15Al1B4 alloys

Table 5.3: Transformation temperatures through DSC for the Ga15Al5, Ga15Al4B1 and Ga15Al1B4 alloys.

Alloy	Stage	Martensite transformation		Austenite transformation	
		temperature		temperature	
		Start (T_{Ms}) K	Finish (T_{Mf}) K	Start (T_{As}) K	Finish (T_{Af}) K
Ga15Al5	1	335	*	272	304**
	2	*	302	304 \$	350
Ga15Al4B1	1	390	361	368	393
Ga15Al1B4	1	527	440	450	540

* Unresolved overlapping transition

** end of the intermediate stage 1

\$ start of intermediate stage 2

Figure 5.6 shows the thermo-magnetic M-T plots for the cast and the heat-treated alloys under a biasing field of 500Oe. The alloy Ga15Al5 reveals three transitions a rise beyond 302K with a change of slope at 326K indicated by arrow 1 in Fig 5.6 prior to transition to paramagnetic state. The alloys containing boron also show change of slope with increasing temperatures; however the rate of change of slope does not show a rise but a different rate of fall. The point where there is a change in rate, is marked with arrow 2 in the figure and it is in conformity with T_{Ms} temperature noted through DSC measurements. As discussed in experimental methods, the martensite phase with higher saturation magnetization shows an increased magnetization because of anisotropy. It appears that the specific set of properties may cause either an increase or a decrease in magnetization with temperature rise and both deviations are signatures of the underlying transformation. The Curie temperatures noted through these measurements are 357 K for the alloy Ga15Al5 and 570K for the alloys Ga15Al1B4 as well as Ga15Al4B1.

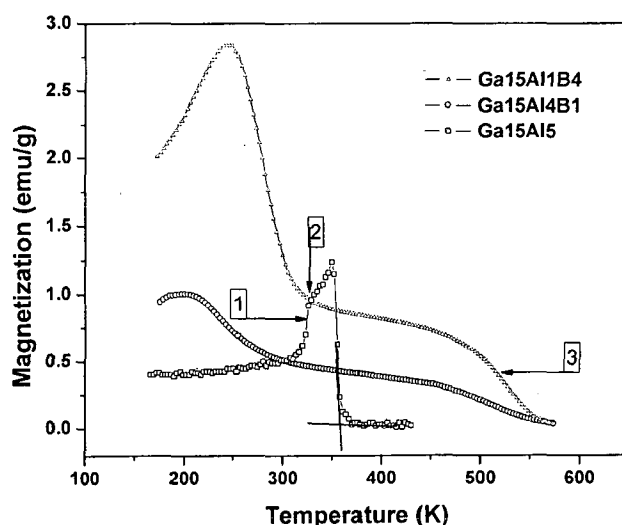


Fig 5.6: Thermo-magnetic M-T curves for Ga15Al5, Ga15Al4B1 and Ga15Al1B4 alloys

5.1.4 Room temperature Magnetization Behavior

The room temperature magnetization curves of the alloys are shown in Fig 5.7. The magnetization observed are of 47.0, 6.5 and 8.8 emu/g for the Ga15Al5, Ga15Al4B1 and Ga15Al1B4 alloys respectively for an applied field of 12kOe. It may be noted that the M-H curve has not reached saturation for the Ga15Al4B1 and Ga15Al1B4 alloys. While the curves retraced themselves for these alloys on removal of the magnetic field, Ga15Al5 alloy shows a hysteresis with coercivity value of 370 Oe.

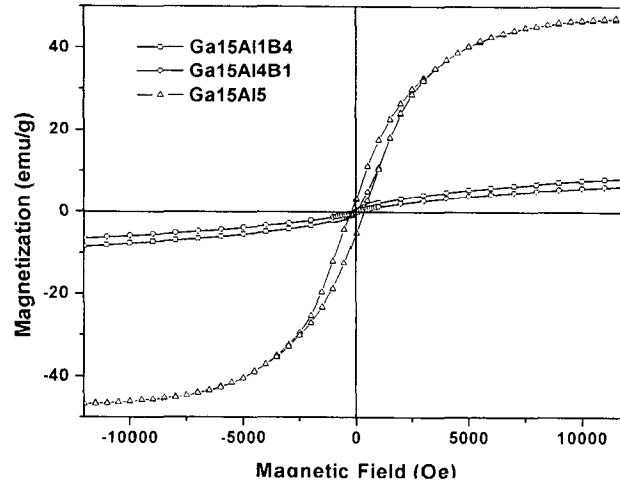


Fig 5.7: Room temperature magnetization curves for the Ga₁₅Al₅, Ga₁₅Al₄B₁ and Ga₁₅Al₁B₄ alloys

5.2 RESULTS OF STUDIES FOR METASTABLE Ni₅₀Mn₃₀Ga₁₅Al_{5-x}B_x ALLOYS

5.2.1 Structural Characterization of the Alloys

The x-ray diffraction patterns taken on the ribbons are shown in Fig 5.8. All the obtained reflections indicate 7-M martensite phase. The obtained patterns differ only in the relative intensities of the peaks but reflection positions are almost identical. Thus, the lattice parameters do not change significantly. The interplanar spacing and the indexing of the patterns to the 7M phase are indicated in Table 5.4.

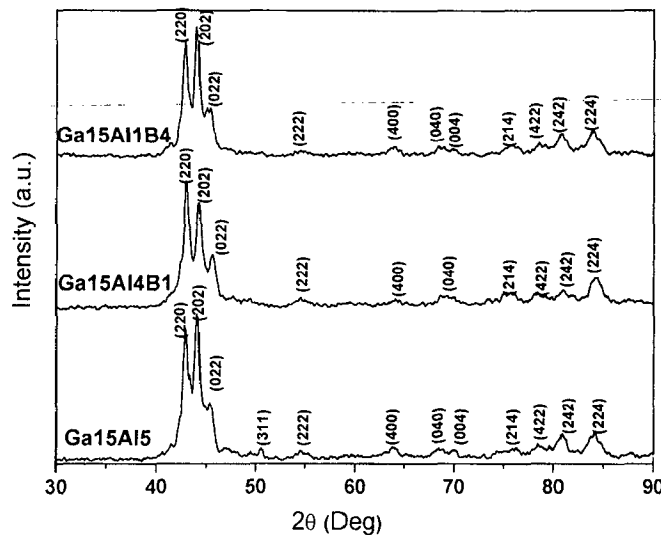


Fig 5.8: The x-ray diffractograms of the melt spun ribbons of Ga₁₅Al₅, Ga₁₅Al₄B₁ and Ga₁₅Al₁B₄ alloys

Table 5.4: The x-ray peak reflections and their assignments to various planes for the melt spun ribbons of Ga15Al5, Ga15Al4B1 and Ga15Al1B4 alloys.

Peak Positions in terms of Interplanar spacing (Å)			Reflecting Plane 7M martensite (hkl)
Ga15Al5	Ga15Al4B1	Ga15Al1B4	
2.109	2.109	2.109	220
2.043	2.043	2.043	202
1.985	1.985	1.985	022
1.804	-	-	311
1.681	1.681	1.681	222
1.457	1.457	1.457	400
1.371	-	1.371	040
1.343	1.343	1.343	004
1.251	1.251	1.251	214
1.217	1.217	1.217	422
1.185	1.185	1.185	242
1.149	1.149	1.149	224

The structural examination for the melt spun ribbons was carried out using the TEM. Figure 5.9(a) shows the TEM bright field image of the Ga15Al5 alloy ribbon. The image shows twinned martensite structure as well as areas free from twins, indicating the presence of untwinned martensite or another phase. The selected area diffraction pattern taken from untwinned portion (marked with circle in Fig 5.9(a)) is shown in Fig 5.9(b). The diffused ring pattern obtained clearly reveals the presence of an amorphous /nano-crystalline structure in the alloy.

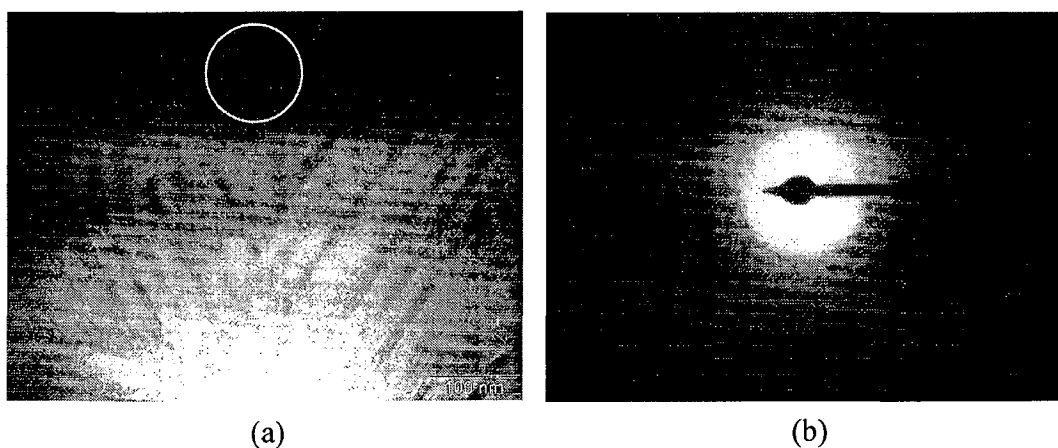


Fig 5.9: (a) The TEM picture of alloy Ga15Al5 showing martensite plates along with other phase and (b) SAD pattern from the area circled in (a) showing the diffused ring pattern of amorphous/nanocrystalline phase.

The structure of martensite phase in Ga15Al5 ribbons has been viewed at higher magnification and showed the plate width of 15-20 nm as shown in Fig 5.10 (a). Figure 5.10(b) shows the corresponding SAD pattern indexed with zone axis $[\bar{1}11]$. The noticeable features of the SAD pattern are streaking of the major spots in certain direction as well as satellite spots. The spots in $\langle 101 \rangle$ direction do not show any streaking and thus, $\langle 101 \rangle$ is the common direction between the twins or the twin plane. The streaks in spots in (202) and (022) could be related to the twinned structure and conformed to the orientation relationship seen for the twin orientation in Fig 5.9 (a). The satellite spots could be indexed to superlattice spots from modulated 7M martensite also referred as 14M in orthorhombic coordinates similar to those reported earlier in Ni-Mn-Ga alloys (Bennett et al 2004). The SAD pattern obtained, is consistent with the x-ray diffraction pattern obtained for this alloy (Fig 5.8.)

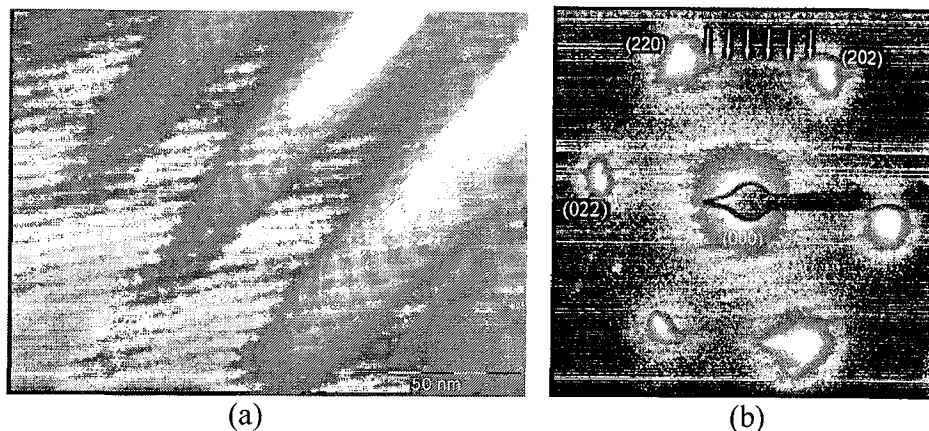


Fig 5.10: (a) The TEM BF image and (b) corresponding SADP for Ga15Al5 alloy showing the 7M martensite phase.

Figure 5.11 shows the internal structure of the twinned plates showing nano-twins of 3-5 nm within the primary plates. The internal structure within the twins is reported earlier (Bennett et al 2004). The twinning angle seen here is about 70° and it matches well with the angle of rotation of streaked spots noticed in SAD pattern in Fig 5.10(b). The internal nano-twins therefore had the same orientation relationship as the primary martensite plates in these alloys.



Fig5.11: The internal twinning within primary martensite plates in Ga15Al5 alloy

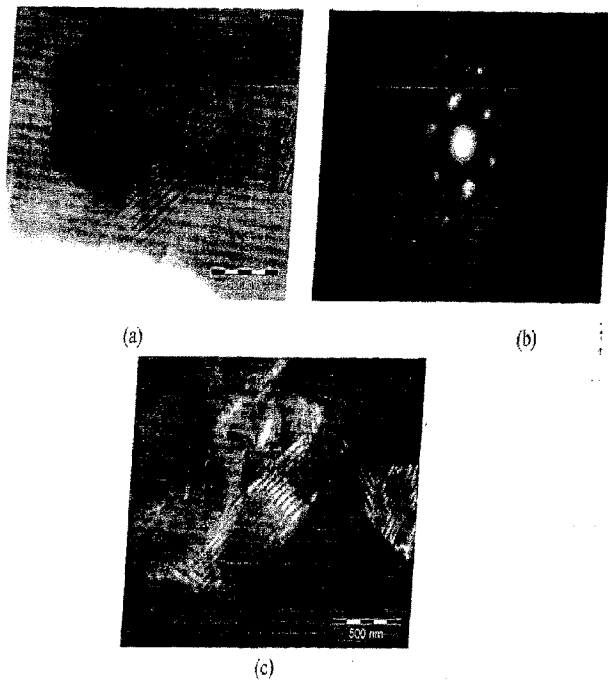


Fig 5.12: (a) The TEM micrograph of Ga15Al4B1 alloy, (b) the SADP for the structure and (c) dark field image from the (220) reflection

The Microstructure of the alloy Ga15Al4B1 along with its SAD pattern is shown in Fig 5.12 (a) and (b). The image shown in Fig 5.12 (a) reveals the martensite plate structure in few localized area. The diffraction pattern shows 7M modulated martensite structure. The dark field image obtained from the (220) spot of the diffraction is shown in Fig 5.12(c). The image shows that contribution to this diffraction is not limited to the areas visible in the structure as plates, but other areas as well. The martensite phase in these areas was either untwinned or did not have the twinning planes in the viewing direction.

Fig 5.13 shows the martensite plates and the diffraction pattern of the corresponding area, indicating the same crystallographic features as for the ribbons in alloy Ga15Al5.

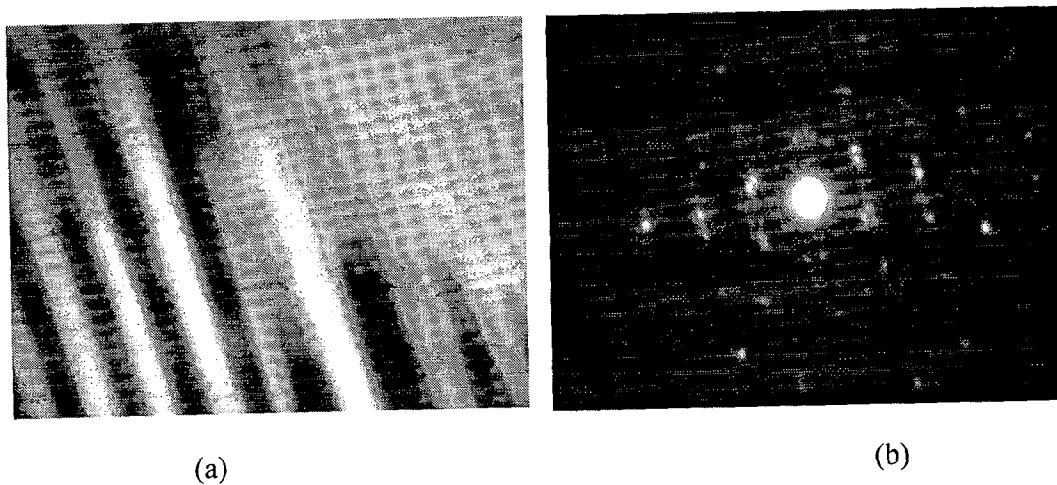


Fig 5.13: (a) The TEM microstructure of the twinned martensite in alloy Ga Al4B1 and (b) the corresponding SADP indexed with 7M martensite structure.

Alloy Ga15Al1B4 shows a similar crystallographic structure but with different microstructure. Instead of spheroid grain seen for other two alloy ribbons, cellular structure with signs of a phase removed during the thinning process (Fig 5.14). On further magnification, the cellular structures revealed martensite plates forming within prior austenite cells. The martensite structure is, however, similar to that obtained in other ribbons.

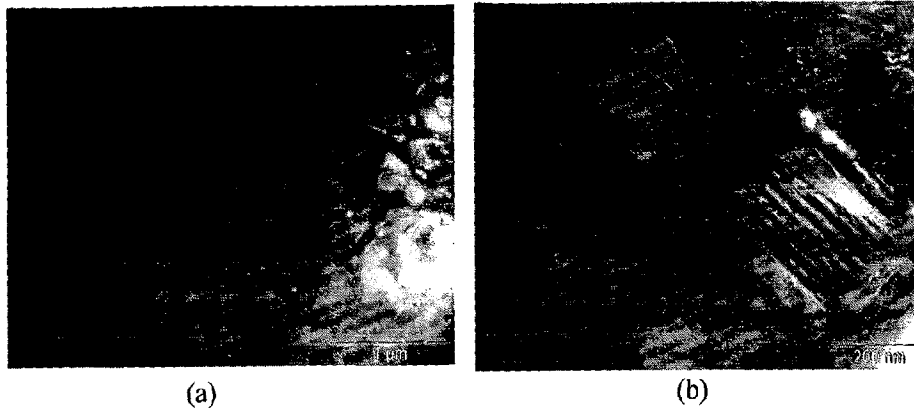


Fig 5.14: (a) TEM image of Ga15Al1B4 showing cellular structure with bright spots, indicative of fall of non- adherent particles.(b) enlarged cells from some area from (a) showing plates within the cell.

The primary martensite plates in Ga15Al1B4 alloy ribbons show the nano-twin as in Fig. 5.15(a), also observed in other alloy ribbons investigated. In some areas, more than two variants of the martensite also could be seen (Fig 5.15(b)).

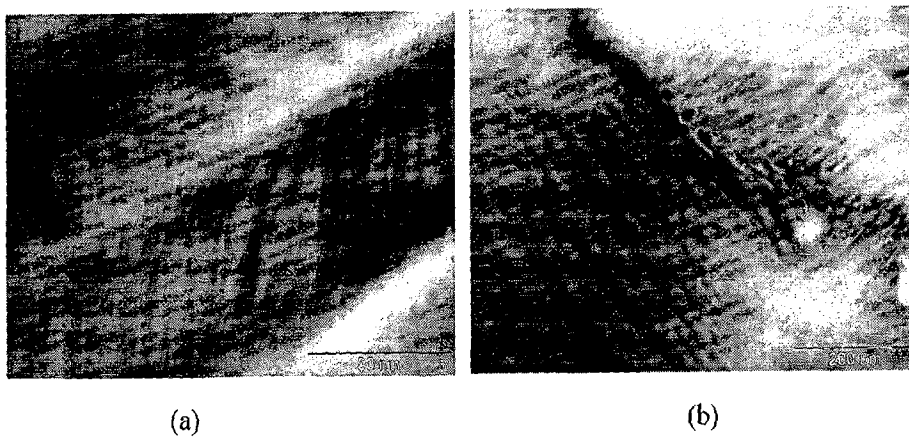


Fig 5.15: TEM image showing typical microstructural features of (a) the internal twin structure and (b) multiple twin variants noticed in Ga15Al1B4 alloy ribbons

5.2.2 Transformation Characteristics of the Alloys

Figure 5.20 shows the DSC thermograms of the ribbon specimens. The obtained martensite transformation temperatures are listed in Table 5.5. A sharp transformation peak is obtained for the alloy Ga15Al5, whereas the alloys Ga15Al4B1 and Ga15Al1B4 show diffuse transitions. The highly diffuse transition for the alloy Ga15Al4B1 does not allow clear demarcation of the peak start/ finish and the values indicated in the Table 5.5, determined by the tangent intersection method, are indicative only. Due to the shape of the diffuse peak, the peak area indicative of the transformation enthalpy could not be compared here.

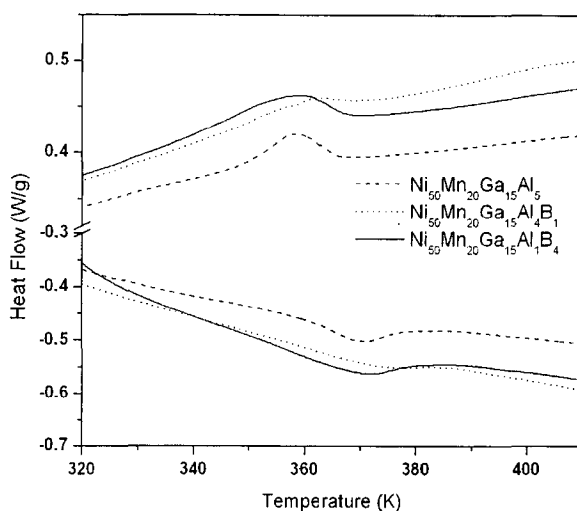


Fig 5.16: DSC thermograms of the melt spun Ga15Al5, Ga15Al4B1 and Ga15Al1B4 ribbons.

Table 5.5: Transformation temperatures through DSC for the Ga15Al5, Ga15Al4B1 and Ga15Al1B4 alloy ribbons

Alloy	Martensite transformation temperature		Austenite transformation temperature	
	Start (T_{Ms}) K	Finish (T_{Mf}) K	Start (T_{As}) K	Finish (T_{Af}) K
Ga15Al5	367	346	357	378
Ga15Al4B1	373	348	352	383
Ga15Al1B4	368	344	356	377

Figure 5.17 shows the transformation characteristics studied through thermo-magnetic measurements. The melt spun ribbons show a continuous fall in magnetization with increasing temperature. However, the magnetization did not fall to zero within the measurement range. A linear fall excepting an intermediate rise in the temperature range from 300 to 350 K, is noticed for the all the alloy ribbons. While the rise in magnetization with temperature may be attributed to martensite transformation in analogy with other alloys in the present study, the fall patterns do not match with the clear Curie transition noticed for the other alloys. This behavior, however, appears to be due to phase mixtures with different Curie temperatures. The Ga15Al5 alloy clearly shows a rapid fall after the martensite transition and then a slower fall showing the manifestation of two phase Curie temperatures. It may be noted here that like the DSC measurements, the sharpness of transition has decreased in the sequence Ga15Al5 to Ga15Al1B4 and then Ga15Al4B1. The transition temperature range noticed through these measurements is also in similar to those obtained from DSC measurements.

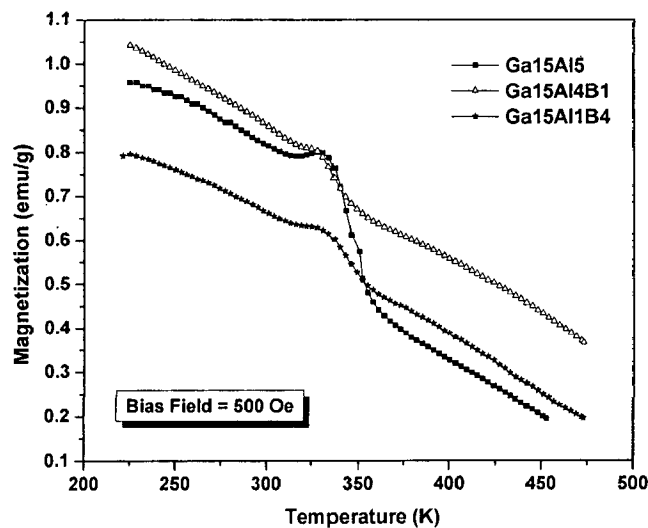


Fig 5.17: Thermo-magnetic M-T measurements for the melt spun alloys Ga15Al5, Ga15Al4B1 and Ga15Al1B4

5.2.3 Room Temperature Magnetization Behavior

The room temperature hysteresis loops of the ribbons are presented in Fig 5.18. The inset in the figure shows a blow-up of the plot around the origin. The Ga15Al5, Ga15Al4B1 and Ga15Al1B4 ribbons show magnetization values of 13.0, 7.8 and 6.3 emu/g at 20 kOe. All the alloys showed hysteresis during reverse magnetization and the coercivity values obtained (Fig 5.22 inset) were 183Oe for alloy Ga15Al5 and 280Oe for the boron containing alloys.

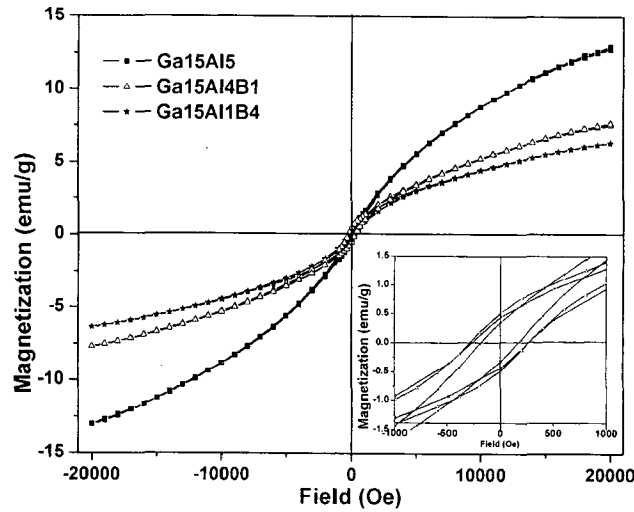


Fig 5.18: Room temperature M-H measurements of the melt spun ribbons. The inset shows an enlarged view around origin.

5.3 RESULTS FOR RARE EARTH SUBSTITUTION INTENDED FOR Ga IN $Ni_{50}Mn_{30}Ga_{20}$

Alloy compositions with rare earth element R substituting Ga in NMG as $Ni_{50}Mn_{30}Ga_{19}R_1$ have been prepared. Light rare earth Sm and heavy rare earth Dy have been selected for R in view of different magnetic exchange interaction between light and rare earths with transition metals. Alloys have been accordingly prepared by repeated arc melting. The cast alloys have been cut, sealed in evacuated quartz ampoules and heat-treated at 1273 K for 72h and at 1073K for 48h in a vacuum furnace and water quenched (heat-treatment₂). The alloys are designated and referred later as Ga19Sm1 and Ga19Dy1 as per the convention followed for designation in this study

5.3.1 Chemical Composition

Table 5.6 shows the aimed and analyzed compositions of the alloys. While the compositions were aimed for one atom percent of the rare earth substitutions, the analyzed compositions of the alloys processed similarly are found to be off from the intended levels.

Table 5.6: Nominal and analyzed compositions of the Ni40Fe10 and Ni40Co10 alloys

Alloy Designation	Nominal Composition				Analyzed Composition							
	at%				Wt%				Equivalent average at%			
	Ni	Mn	Ga	RE	Ni	Mn	Ga	RE	Ni	Mn	Ga	RE
Ga19Sm1	50	30	19	1Sm	46.38 ±0.66	29.93 ±0.32	19.4 ±0.18	4.17 ±0.09Sm	48.15	33.20	16.96	1.69Sm
Ga19Dy1	50	30	19	1Dy	48.78 ±1.102	30.43 ±0.367	19.82 ±0.283	1.18 ±0.014Dy	49.55	33.02	16.96	0.47Dy

5.3.2 Structural Characterization of the Alloy

The BSE image of the alloys after heat-treatment is shown in Fig 5.19. Both the alloys show two phase structure. The matrix phase is dark containing bright particles of second phase in linearly patterned array. The compositions of the matrix and second phases analyzed through EPMA are shown in Table 5.7. Both the alloys show that the rare earth element added has gone into the second phase with relatively lower Mn content. The matrix phase composition has accordingly changed from the intended composition due to the phase separation.

Table 5.7: Analyzed average compositions in atom % for the matrix and the second phase in Ga19Sm1 and Ga19Dy1 alloys

Chemical Composition	Ga19Sm1				Ga19Dy1			
	Ni	Mn	Ga	Sm	Ni	Mn	Ga	Dy
Matrix	48.60	33.20	18.20	0	48.48	33.23	18.29	0
Second	51.45	11.35	22.082	15.12	52.81	10.34	20.88	16.13

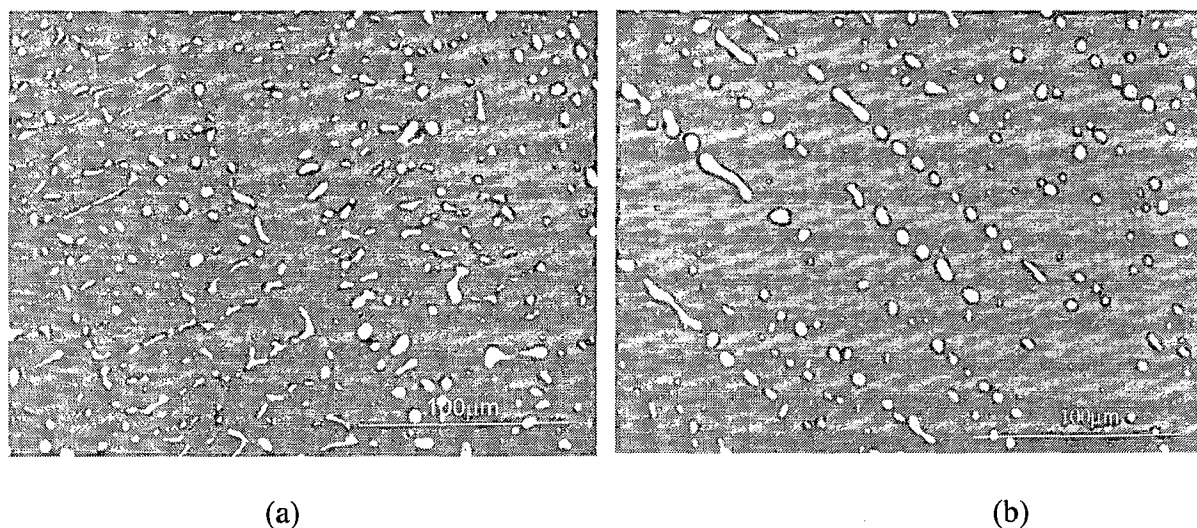


Fig 5.19: Back Scattered Electron images for a) Ga19Sm1 and b) Ga19Dy1 alloys

The x-ray diffractograms of the alloys are presented in Fig 5.20. The diffraction pattern for the base alloy NMG from section 4.1 is included here for comparison. The major diffraction peaks could be indexed to tetragonal non modulated martensite as seen for the base alloy and the additional un-indexed peaks could be attributed to the presence of second phase. Some of the peaks of the two phases may overlap and hence the indexing of the peaks attributable to second phase is difficult. Being the Table 5.8 shows the peak position obtained in the diffraction pattern, tabulated along with the diffracting planes of the martensite phase.

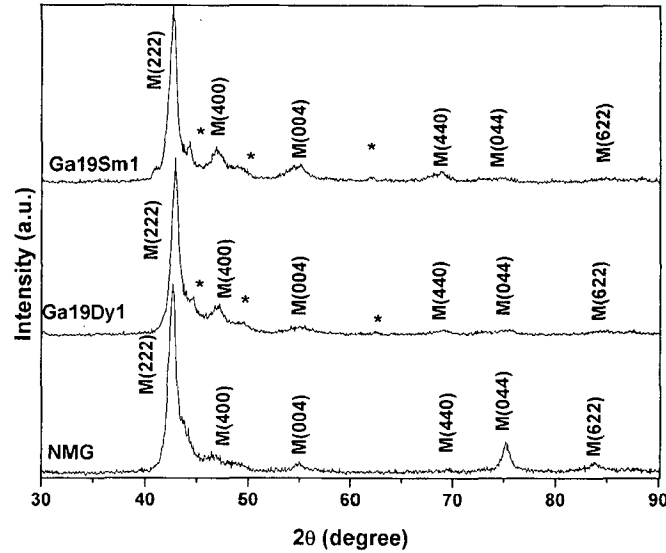


Fig 5.20: X ray diffractograms(Cu K_α) of $\text{Ni}_{50}\text{Mn}_{30}\text{Ga}_{20}$, $\text{Ni}_{50}\text{Mn}_{30}\text{Ga}_{19}\text{Sm}_1$ and $\text{Ni}_{50}\text{Mn}_{30}\text{Ga}_{19}\text{Dy}_1$

Table 5.8: The assignment of the x-ray diffractogram peaks for heat-treated $\text{Ga}_{19}\text{Sm}_1$ and $\text{Ga}_{19}\text{Dy}_1$ alloys. The values for NMG alloy is added for comparison

Ga19Sm1		Peak Position				Reflecting plane	
		Ga19Dy1		NMG		Tetragonal martenite	Second phase
2θ (deg)	d-spacing (Å)	2θ (deg)	d-spacing (Å)	2θ (deg)	d-spacing (Å)	(hkl)	
42.80	2.110	42.84	2.108	43.18	2.093	222	
44.38	2.039	44.64	2.028				*
46.96	1.933	47.09	1.928	47.129	1.926	400	
49.03	1.856	49.03	1.856				*
55.02	1.667	55.02	1.667	55.679	1.649	004	
62.14	1.492	62.55	1.483				*
68.90	1.361	68.90	1.361	68.68	1.365	440	
74.87	1.267	75.43	1.259	75.86	1.253	044	
84.88	1.141	84.64	1.143	84.32	1.147	622	

5.3.3 Transformation Characteristics

The DSC thermograms obtained for the alloys along with that of NMG are shown in Fig 5.21. Table 5.9 gives the transformation temperatures of the alloys obtained from the plots. An increase in martensite transformation temperatures is seen with rare earth addition. The extent of increase increases with increasing level of the rare earth elements present.

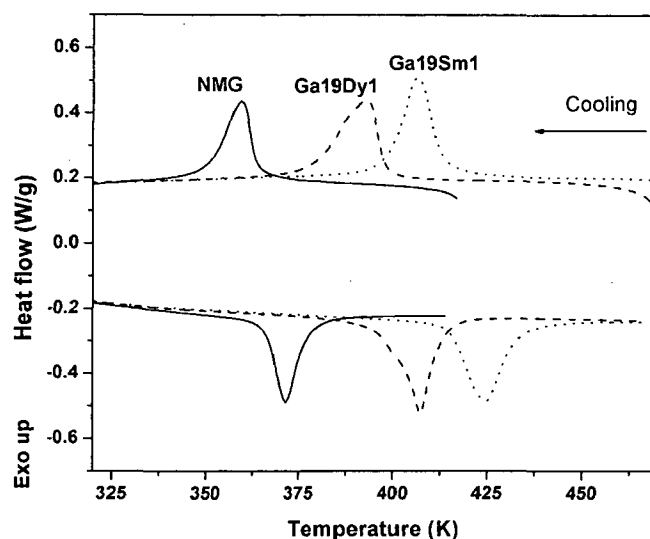


Fig 5.21: The DSC thermograms for the alloys Ga19Sm1, Ga19Dy1 and the alloy NMG

Table 5.9: Transformation temperatures for the alloys Ga19Sm1 and Ga19Dy1 through DSC.

Alloy	Martensite transformation temperature		Austenite transformation temperature	
	Start (T_{Ms}) K	Finish (T_{Mf}) K	Start (T_{As}) K	Finish (T_{Af}) K
Ga19Sm1	414	396	414	434
Ga19Dy1	398	376	394	414
NMG	364	351	366	379

Figure 5.22 shows the thermo-magnetic measurements of the alloys showing the transformations through change in magnetization. The plot for the base alloy, NMG, shows magnetization of 7.4 emu/g at low temperature under the applied bias field of 500 Oe. The magnetization starts rising from 317 K showing a peak value at 353 K and then falls to zero at 380 K; these temperatures are estimated by tangent intercept method. The alloys, Ga19Sm1 and Ga19Dy1, show that the magnetization is increasing slowly at low temperatures, start rising rapidly at 251K and 271 K for the two alloys respectively and their corresponding Curie temperatures are estimated as 333 and 353 K. An abrupt change in magnetization signifies structural changes within the material and has been attributed to martensite transformation. The martensite to austenite reverse transformation starts at temperatures T_{As} , which is 251, 271 and 317 K respectively for the alloys Ga19Sm1, Ga19Dy1 and NMG. These measurements, therefore, indicate a trend different from those observed in DSC measurements, showing increased martensite transformation temperature with rare earth addition. It may, however, be noted that rare earth containing alloys are not single phase alloys and magnetization changes could have been contributed by any or both of the phases. The difference in magnetization characteristics of the different phases of the alloys is reflected in the rate of fall in magnetization in the three alloys. While the alloy NMG shows a rapid fall of magnetization near T_c , the rate of fall is relatively slower with increased rare earth content.

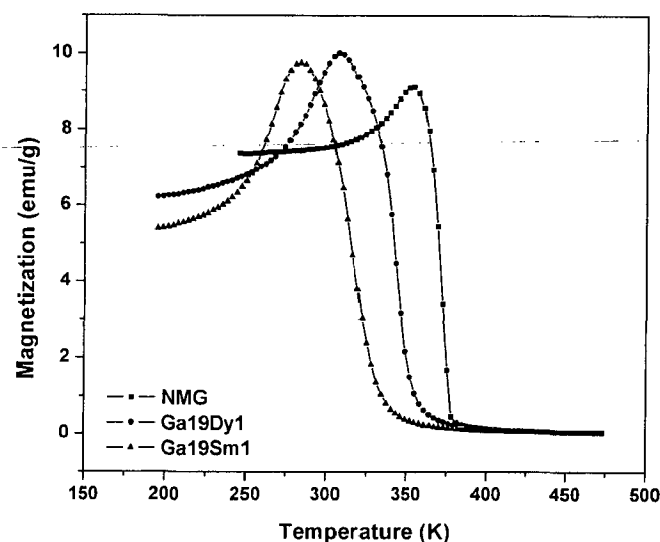


Fig 5.22: The thermo-magnetic M-T plots for the alloys Ga19Sm1, Ga19Dy1 and the alloy NMG.

5.3.4 Room Temperature Magnetization Behavior

Figure 5.23 shows the Room Temperature hysteresis curves for the alloys. Saturation magnetization values of the Sm containing, Dy containing and rare earth free base alloys are respectively 38.2, 43.2 and 51.2 emu/g. All these alloys show small coercivity values of about 180 Oe (Fig 5.26 inset).

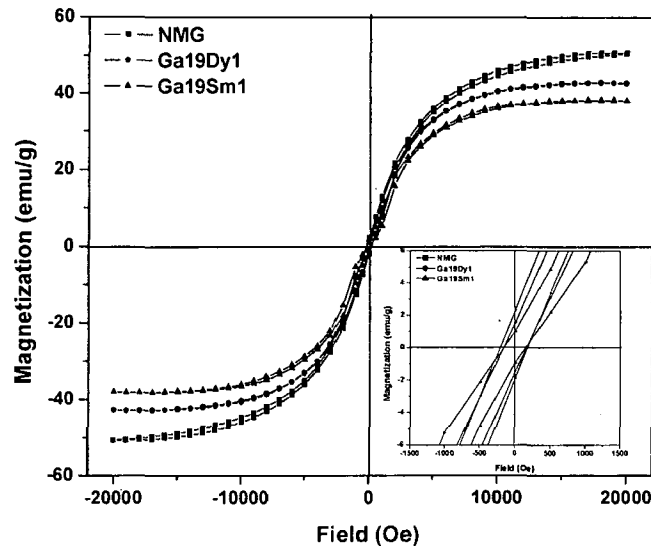


Fig 5.23: The Room Temperature hysteresis curves for the alloys Ga19Sm1, Ga19Dy1 and the alloy NMG. The inset shows the area around origin.

5.3.5 Room Temperature Mechanical Behavior

The heat-treated alloys have been tested in compression to know their room temperature mechanical behavior. Figure 5.24 shows the results obtained for the alloys containing rare earth elements along that of the base alloy, NMG. The characteristic mechanical properties are tabulated in Table 5.10.

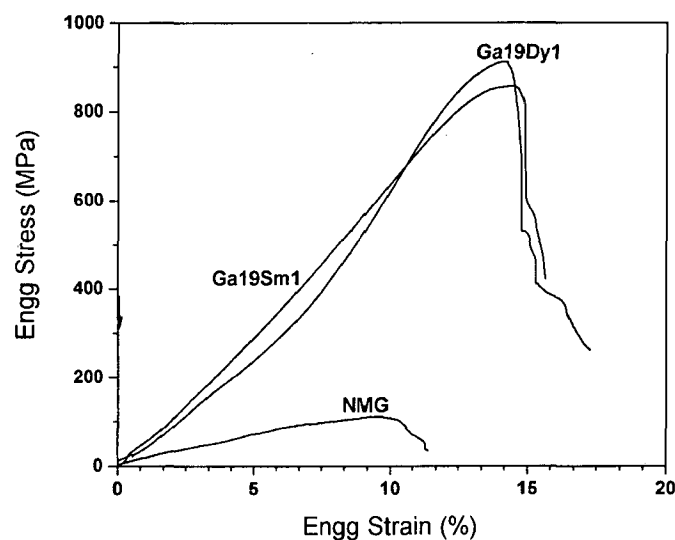


Fig 5.24: The Room Temperature compression test results for the alloys Ga19Sm1, Ga19Dy1 and the alloy NMG.

Table 5.10: Mechanical properties of the alloys Ga19Sm1, Ga19Dy1 and the alloy NMG

Alloy	Slope of the Initial portion of the curve (GPa)	Maximum value	
		Ultimate strength (MPa)	Max strain at failure (%)
Ga19Sm1	6.20	857	15.6
Ga19Dy1	5.00	909	17.2
NMG	1.12	110	11.3

The stress-strain behaviour reveals a considerable increase in the strain hardening and the UTS and strain to fracture in the heat treated alloys containing rare earth addition over those observed in NMG.

5.4 DISCUSSION

The alloys with trivalent elements Al/ B replacing Ga have shown different microstructures and crystal structures at different compositions and different processing conditions. While the alloy with 5 at% Al is single phase alloy, addition of boron results in multi-phase structures in the alloy even after heat treatment. The quantities of second phase are generally within detectable limits of x-ray diffraction and many of the diffraction peaks from this phase might have similar inter-planar spacings as the matrix phase. A few un-indexed peaks do not permit unambiguous identification of the phase observed in the alloys containing boron. In view of the presence of low atomic number element boron, present in these samples, a meaningful EPMA analysis is not possible. Darker contrast of the secondary phase than the matrix in BSE images of the alloys indicates enrichment of this phase by elements of higher atomic number. This observation also signifies relatively higher presence of low atomic number elements like B and Al in the matrix phase. It may be noted that the crystal structure of the alloy Ga15Al5 is that of modulated martensite which changes to a non modulated structure with addition of B in the alloy. Even though small size difference exists between the constituents of ternary Ni-Mn-Ga alloys, these elements are in close vicinity of

each other in the periodic table. The similarities permitting modulated long period arrangements are compromised by the addition of boron and hence the change to non modulated structure. Table 5.11 summarizes the crystal structure data obtained through x ray diffraction measurements for the matrix phase in our alloys.

The rapid solidification process has been employed for obtaining metastable phase structures in these alloys. The process normally does not permit separation of the phases because of faster cooling suppressing it and the x-ray diffractograms of melt spun ribbons could be indexed fully to a 7M martensite phase similar to those reported for the ternary Ni-Mn-Ga alloys without any un-indexed peaks to suggest presence of any secondary phase. The x-ray peak positions obtained for the different alloys are very close to permit any distinction in terms of the lattice parameters. The lattice parameters are normally a function of compositions and/ or lattice strains. With similar processing treatment, these x ray diffractograms without any perceptible variation in the peak position are indicative of similar composition of the phase indexed by X-ray diffraction pattern. It may be noted that TEM microstructures of the rapidly solidified ribbons show the presence of additional phases such as amorphous phases in case of alloy Ga₁₅Al₅ ribbons; or non-adherent chemically different phases falling out of the thinned TEM specimens in case of Ga₁₅Al₁₁B₄ ribbons. Boron is reported to be an element promoting glass formation in Fe based alloys with glassy phase crystallizing into the boride phases on heating (Mathur et al 1987). Such metastable phases may have appeared due to sluggish crystallization in rapidly solidified ribbons. The amount of amorphous phase is expected to increase with addition of boron. But, no amorphous phase could be located in different specimens of Ga₁₅Al₄B₁ ribbon samples. The Ga₁₅Al₁₁B₄ alloy ribbons indicate presence of non-adherent phase in TEM micrograph. With the chemical composition of the matrix phase being the same in this alloy ribbons as that of boron free Ga₁₅Al₅ ribbons, it is reasonable to assume that the second phase in these ribbons could have been a boron rich phase. The rapid quenching at still higher cooling rates to suppress phase separation is, however, not attempted as the aim has been to obtain metastable crystalline phases and not amorphous phases.

Table 5.11: Martensite phase and lattice parameters for the alloys Ga15Al5, Ga15Al4B1 and Ga15Al1B4 alloys after heat-treatment as well as on rapid solidification

Alloy	Heat-treated alloys					Rapidly solidified ribbons						
	Structure#	Lattice parameters		c/a	Cell vol. (\AA^3)	Structure#	Lattice parameters			c/a	b/a	Cell vol. (\AA^3)
		a (\AA)	c (\AA)				a (\AA)	b (\AA)	c (\AA)			
Ga15Al5	5M	5.87	5.57	0.95	191.92	7M	6.05	5.67	5.54	0.91	0.93	190.04
Ga15Al4B1	NM	7.67	6.83	0.89	401.80	7M	6.05	5.67	5.54	0.91	0.93	190.04
Ga15Al1B4	NM	7.78	6.69	0.86	404.93	7M	6.05	5.67	5.54	0.91	0.93	190.04
NMG	NM	7.73	6.59	0.86	393.77	Not prepared through rapid solidification						

NM indicates Non-modulated tetragonal and 5M & 7M indicate modulated martensite structures.

Though the crystalline matrix phase present in our melt-spun ribbons shows similar structure as well as the same unit cell size, the morphology of the pre-martensite is found to be different. Alloys Ga15Al5 and Ga15Al4B1 show spheroidal grains but faceted grains are observed in Ga15Al1B4 alloy. Faceted crystal formation shows that the interfacial energies at different faces of the crystals are different, which may have facilitated formation of polyhedral grain boundary in boron rich alloy. With isotropic nature of the amorphous phase, the spherical grain shape is expected as it has been observed in Ga15Al5 and Ga15Al4B1 alloys. The faceted grains of the alloy Ga15Al1B4 shows a change in interfacial energies because of the presence of boron, which may segregate to grain boundary and result in non-adherent boron rich phase coming out from the grain boundary area, as it has been observed.

The base alloy NMG after heat treatment shows non-modulated martensite structure. The lattice parameters for the phase are $a = 7.7306 \text{ \AA}$ and $c = 6.5906 \text{ \AA}$ with unit cell volume of 393.868 \AA^3 . But the alloy Ga15Al5 after heat treatment shows 5M martensite structure and one to one comparison of the lattice parameters is not possible. The unit cell volume of 191.92 \AA^3 for the 5M martensite structure in the alloy Ga15Al5 may however be compared

with alloys with similar structure reported in literature. The value compares well with the value of 197.2 \AA^3 obtained for a ternary $\text{Ni}_{50.1}\text{Mn}_{29.1}\text{Ga}_{20.8}$ alloy with 5M structure (Richard et al 2006). Modifications in properties on addition of trivalent Al in place of Ga are expected only through modification of inter-atomic distance without any change in average electron to atom ratio. Attempts have been made to modify inter-atomic distances significantly by addition of boron, trivalent element with smaller atomic sizes. Heat-treated alloys containing boron, however, have shown non modulated structure comparable to that observed in heat treated base alloy, NMG. The c/a ratio of the alloys fell with increasing boron from 1 at% to 4 at%. Unit cell volume is expected to decrease with increasing boron and decreasing Al; however, only a small rise in cell volume is noticed in going from alloy $\text{Ga}_{15}\text{Al}_{4}\text{B}_1$ to $\text{Ga}_{15}\text{Al}_{1}\text{B}_4$ ribbons. With BSE images suggesting boron to be present within the matrix phase, it is possible that boron may have gone to interstitial sites instead of substituting at the Ga site as envisaged. Thus, boron addition may result in only small cell volume change in alloys containing boron.

Lattice parameters obtained for 7M martensite phase in ribbons may be compared to those reported in literature for 14M orthorhombic cell obtained in ternary $\text{Ni}_{47.3}\text{Mn}_{33.1}\text{Ga}_{18.6}$ alloy containing lower Ga, showing lattice parameters of $a= 5.8466$, $b= 6.1432$ and $c= 5.5391 \text{ \AA}$ and a lattice volume of 198.49 \AA^3 . The lattice volume obtained in 7M martensite in the present study is smaller. It may be noted that 7M phase obtained is the same for different alloys, where it has been observed and the composition changes may have been accommodated by formation of secondary phase, not identified by x ray diffraction but observed in TEM images. The presence of minor amorphous or crystalline phases, variation in the lattice parameters from those reported in literature may be related to difference in composition of the alloys investigated in the present study. Addition of Al in the heat-treated alloys has resulted in comparable unit cell volume with that of NMG in 5M structure; whereas rapid quenching results in lower volume. This may be attributed to lower atomic ordering associated with the technique.

The transformation temperatures of the heat-treated alloys with Al/ B additions show two-stage martensite transformation. Martensite transformation are reported to go through a sequence of the intermediate martensite phase (Segui et al 2007) and it appears to be the case for the alloy Ga15Al5. Low temperature diffraction patterns are not available to decide the transformation sequence unambiguously. As discussed in the previous chapter, the temperature $T_0 = (T_{Ms}+T_{Af})/2$ is taken as the thermodynamic equilibrium temperature between the martensite and austenite phase and is considered dependent on the chemistry whereas the transformation temperature ranges depicting the nucleation of the phases may be structure dependent (Otsuka and Wayman 1998). The plot of transformation temperature with boron replacing Al is shown in Fig 5.25. Addition of B for Al has resulted in increasing the martensite transformation temperature almost linearly whereas T_c increases to saturate at higher boron. It has been presumed that the martensite transformation occurs when the Fermi surface reaches the Brillouin zone boundary with increasing number of valence electron and the alteration in the Brillouin zone boundary may affect the martensite transformation temperature (Entel et al 2007). The packed structures normally increase the transformation temperatures (Entel et al 2003, Zhiang et al 2003). The lattice volume of the alloys containing boron is comparable with different c/a ratios. The c/a ratio of the 4% boron alloy is 0.86 compared to 0.89 for the alloy with 1% boron. Though the exact density of states calculation is not available for these alloys, it appears that the compact structure along a-axis has resulted in increase of the martensite transformation temperature. The martensite transformation temperature range for the high boron alloy is $\sim 90K$.

The reversibility of the martensite transformation is related to the thermal hysteresis between the martensite transformation and reverse martensite to austenite transformations. Transformations occurring with large thermal hysteresis are not reversible and are accordingly referred as thermoplastic transformations in contrast to thermo-elastic or reversible transformation with smaller thermal hysteresis (Otsuka and Wayman 1998). The large thermal hysteresis i.e. thermo-plasticity indicate that re-nucleation of the austenite phase in the transformed martensite is difficult. Alloys with thermoplastic martensite transformation or with non-modulated martensite do not show reversible transformation and may not be suitable for technological applications.

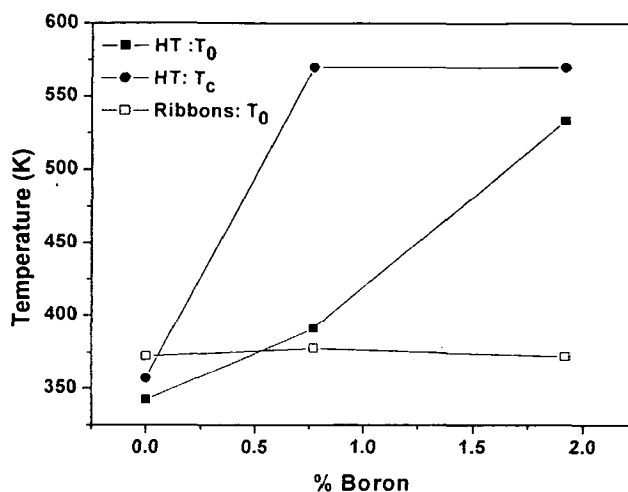


Fig 5.25: Variation of the structural and magnetic transformation temperatures with boron content in Al/B substituted heat treated alloys (HT) as well as melt spun ribbons (Ribbons).

The transformation temperatures for the melt spun ribbons are also shown in Fig 5.25 along with heat-treated alloys. The ribbons as stated earlier, show modulated martensite and their T_0 temperatures do not change significantly with compositional modifications. The T_c temperatures for the ribbons are not shown here as the alloys have not reached zero magnetization within the range experimental measurement in this study (Fig.5.17). Similar T_0 is consistent with the similar crystal structure parameters of the alloys indicating that the phase is no different in these alloys. It may be noted here that with long heat-treatments, the secondary phase may get depleted in lighter elements, but rapid quenching in melt spun ribbons may form secondary metastable phase relatively rich in lighter elements. The different trends in the structure of the alloy with heat-treatment² under equilibrium conditions, appear to be affected by such chemistry modification as well, apart from other process related changes.

The saturation magnetization of the alloys containing Al/B, both heat-treated alloys and the melt spun ribbons, is shown in Fig 5.26. While the magnetization for the heat treated and melt spun alloy Ga15Al4B1 is comparable, the rapid solidification for the other two alloys shows decrease in saturation magnetization values. Both the processing shows lowered magnetization with increasing boron content. Even though the crystal structure obtained is different in the two processing techniques, existence of similar structures obtained as for other ternary Ni-Mn-Ga alloys indicates that the inter-atomic distances between the constituent elements have not changed considerably. The saturation magnetization is affected

by the exchange interaction between the atomic magnetic moments and this interaction depends on the atomic distance between the constituent atoms as illustrated by classical Bethe –Slater curves. A large fall in magnetization for the melt spun ribbon where neither the composition nor the average inter-atomic distances have changed considerably could be attributed to disordered structure resulting on rapid quenching. For the higher boron alloys, the addition of boron may cause loss of ordering even in heat-treated alloys and its overwhelming effect makes the influence of processing technique immaterial.

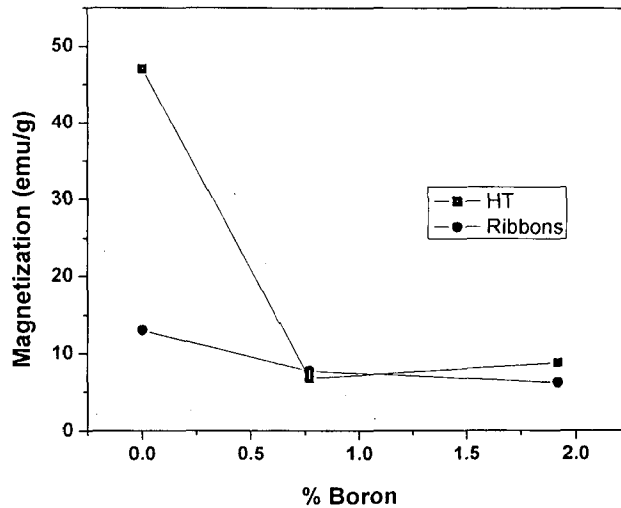


Fig 5.26: Magnetization changes with boron content in Al/B substituted heat treated alloys (HT) as well as melt spun ribbons (Ribbons).

The crystal structures of the heat-treated alloys containing rare earth elements, Ga19Sm1 and Ga19Dy1, are shown in Table 5.12. It may be noted here that both the alloys have shown ternary Ni-Mn-Ga matrix phase with ~33%Mn and 18%Ga. The rare earth additions have gone to a second phase, leaner in Mn and the quantity of the second phase is proportional to the amount of rare earth element added. The formation of second phase with addition of rare earth addition has also been noted earlier (Gao et al 2006, Gao et al 2008, Cai et al 2007) and these studies do not report any solubility of rare earths in the matrix phase. Matrix phase with 1.5 at% Dy has been reported for Ni₅₀Mn₂₉Ga₁₉Dy₂ alloys but there is rare earth free matrix phase at lower concentrations (Gao et al 2006). But the current study has not shown presence of any rare earth element even though rare earth level has gone up to 1.69

at% Sm. The phase composition and the crystal structure show similarity between the matrix phase for different types and different levels of rare earth additions.

Table 5.12: Martensite phase and lattice parameters for the alloys Ga19Sm1 and Ga19Dy1 alloys.

Alloy	Room Temperature Phase structure	Lattice parameters		Unit cell Volume (\AA^3)
		a (\AA)	c (\AA)	
Ga19Sm1	Non-Modulated Martensite T	7.70	6.70	397.24
Ga19Dy1	Non-Modulated Martensite T	7.70	6.66	391.31
NMG	Non-Modulated Martensite T	7.73	6.59	393.86

The transformation temperature determined through thermo-magnetic measurements reveals absence of signatures of well defined martensite transformation. The martensite transformation temperatures are given in Table 5.10. The values obtained show a rise in martensite temperatures with increasing rare earth content. This observation is consistent with those reported earlier (Gao et al 2006, Gao et al 2008, Cai et al 2007). If the thermodynamic equilibrium temperature is defined by $T_0 = (T_{Ms} + T_{Af})/2$, these values show an increase with increasing rare earth content. The T_0 temperatures define the temperatures at which martensite and austenite phases have equal free energies compensating for the other structural factors. This temperature is therefore chemistry dependent and is not expected to change if the chemistry of the two alloys is the same. This is indeed true as can be observed in case of the T_0 temperatures for the melt spun ribbons of alloys containing Al/B (Fig 5.25). The analyzed matrix phase compositions for the alloys Ga19Sm1 and Ga19Dy1 are not much different and indicate rare earth elements in matrix phase below the detection limits, if present. At these small levels, T_0 temperatures are not significantly affected. The results obtained, however, show increased martensite transformation temperatures with rare earth contents. These results are similar to those obtained earlier (Gao et al 2006, Gao et al 2008, Cai et al 2007). Changes in martensite transformation

temperatures when observed have been explained with the change in Mn/Ga ratio of the matrix phase at different rare earth levels. Careful examination of the earlier results indicates that such a scenario may not be explained by the Mn/Ga ratios of the matrix phase alone. For example, analyzed compositions of the matrix phases in $\text{Ni}_{50}\text{Mn}_{29}\text{Ga}_{19-x}\text{Dy}_x$ alloys at $x=0.1$ and 0.2 are $\text{Ni}_{50.04}\text{Mn}_{29.43}\text{Ga}_{20.53}$ and $\text{Ni}_{50.41}\text{Mn}_{29.34}\text{Ga}_{20.25}$ giving Mn/Ga ratios of 1.43 and 1.44 respectively, which resulted in 8-9 K increase in martensite transformation peak temperature (Gao et al 2006). The modified martensite transformations for similar compositions may have to be understood on a broader basis, beyond the limited ambit of such small variations in Mn/Ga ratio.

It may be noted here that the mechanical properties of the alloys with addition of the rare earth elements are significantly enhanced. Apart from increased ultimate strength and maximum strain at failure there is improvement in ductility as well. A large increase in the slope of the initial portion of the curve also indicates considerably increased work hardening of the majority phase with addition of rare earth elements to the alloy. The change in work hardening behaviour clearly indicates the modified chemical compositions. Alloying additions in trace amounts can cause a large change in work hardening behaviour. Both the mechanical properties and DSC results are definitely indicating modified chemistry of the matrix phase. Thus, it appears that rare earth elements may have very limited solubility in the matrix phase at levels below the detection limits of EPMA.

The thermoplastic martensite transformations in the alloys containing rare earth addition show large temperature hysteresis because the reverse martensite transformation requiring nucleation of the austenite phase is suppressed. For too low a nucleation rate, the reverse transformation may not be visualized and estimation of thermodynamic equilibrium temperature T_0 as average of the T_{Ms} and T_{Af} may not be reasonable. The ternary matrix Ni-Mn-Ga phases in general are brittle and can not accommodate large mechanical strains. The compression tests for the alloys containing rare earth elements (Fig 5.24) show that the presence of second phase improves the ductility of the alloys considerably mainly by accommodating the mechanical strains within them. Martensite transformations are nucleation and growth process wherein progressive transformations are eased by the strain

fields generated by the previous transformations. An increase in martensite transformation range in these alloys from 13 K for the alloy NMG to 20-22 K for the alloys containing rare earth elements, may thus indicate reduced thermo-elasticity during the transformations due to reduced driving force for martensite transformation because of soft phases.

Both the T_C and room temperature saturation magnetization fall with addition of rare earth elements as measured by M-T and M-H measurements on VSM. The alloys are clearly two-phase alloys and it is difficult to ascertain the phase responsible for the manifested T_C just prior to attaining complete paramagnetic state. T_C also is composition dependent and it appears the T_C estimated through M-T measurement is the T_C of the second phase with comparable composition but with different chemical species viz Sm and Dy. Dilution by small additions of 0.47 at% Dy or 1.67 at % Sm for the alloy investigated may not be solely responsible for the lower demagnetization values observed in this study. The second phase is Mn-depleted with similar Ga content and even though its crystal structure is not ascertained here, it is reasonable to assume that added rare earth atoms in these alloys may have gone to Mn sites. Such atoms would then be having anti-ferromagnetic coupling with neighbor and thereby reduce magnetization.

Our studies on substitution of trivalent Ga in NMG indicate that though e/a ratio is not modified with addition of trivalent elements Al or B, the properties of the alloys get considerably modified due to change in inter-atomic spacing and thereby, changed density of states as well. Al addition has resulted in stabilizing martensite as well as inter-martensite transformation. Addition of B along with Al in the base NMG alloy results in broadened diffraction peaks attributable to ability of B to refine the grain sizes. While under equilibrium, the secondary phases in alloys with Al and B both are enriched with relatively heavier elements, but under non equilibrium processing i.e. rapid solidification, the reverse is true.

The rare earth additions to NMG may allow small amounts rare earth elements in the matrix phase structure as inferred indirectly by the martensite transformation and mechanical behaviour but their presence is significant in secondary phase. In view of very low solubility, differential behaviour of the light and heavy rare earth elements in magnetic exchange coupling with transition elements could not be significantly influenced.

Quaternary additions have been made to base ternary alloy composition $\text{Ni}_{50}\text{Mn}_{30}\text{Ga}_{20}$ (NMG) with the aim to i) substitute transition elements Ni or Mn by Co or Fe ii) substitute Ga by Al and B based on electronic parity with trivalent elements and iii) substitute Ga by rare earth elements of Sm or Dy, based on the size compatibility. The results of the present study lead to the following conclusions:

1. Analysis of the prepared alloys show that compositions aimed at were largely achieved though with a little lower Ga of around 18 at% in all cases.
2. The Co addition of 10 at% to base NMG alloy show that this element is soluble in alloy subjected to homogenization alone, called heat treatment 1 in this study.
3. The room temperature structure obtained for the alloy containing Co is modulated 5M martensite, which is desirable for FMSM behaviour but the transformation temperatures for this composition could not be exactly estimated by the employed techniques of DSC and VSM measurements.
4. Addition of Co improves the saturation magnetization as well as the Curie temperature of the alloy presumably due to improved magnetic exchange coupling with the Mn atoms.
5. Substitution of Fe for Ni or Mn to the base composition of NMG shows that the solubility limit of Fe in NMG is about 10 at% beyond which second phase appeared in alloys subjected to homogenization and ordering heat treatment called heat treatment 2 in this study.
6. Although substitutions of Fe in NMG was aimed for both Ni or Mn sites, the initial additions of Fe led to their occupation of Ga sites, followed thereafter by occupation of Mn sites and lastly, occupation of a few Ni-sites. The nearby placements of Fe at Ga and Mn sites created clusters of Fe atoms causing paramagnetic Mössbauer sub-

spectrum in a ferromagnetic material. The remaining placements at Mn and Ni-sites have shown ferromagnetic contributions through two Mössbauer sub-spectra for the alloys containing Fe.

7. Initial Fe placement at Ga site reduces the structural and magnetic transition temperatures, whereas with later placement of Fe at Mn sites these transition temperatures increases again. The structural and magnetic transformations remain coupled i.e. $T_c \sim T_M$ up to about 6%Fe.
8. Increasing Fe contents leads to decrease in the martensite temperatures and increase in the Curie temperatures, while resulting in two phase structure beyond the solubility limit.
9. For the alloys containing Fe, the stability of martensite as indicated by variation in martensite transformation temperature, do not show dependence on an average electron to atom ratio but appears to depend on site selection by Fe atoms. The temperature falls with Fe occupying Ga and/or Ni site, but improves with Fe at Mn site.
10. The saturation magnetization in the alloys containing Fe, falls initially with Fe substitutions and then increases again with increasing Fe. These results are consistent with occupation of different atomic sites of Ni, Mn or Ga by Fe. Substitution of Fe for either Ni or Mn increases the magnetization whereas its occupation of Ga sites lowers magnetizations.
11. The Al addition of 5 at% replacing Ga in base NMG alloy show that the element is soluble in alloy subjected to homogenization treatment alone, called heat treatment1 and it promoted the room temperature structure of 5M martensite in place of non-modulated martensite observed in NMG.
12. Though average electron to atom ratio does not change with Al substituting Ga due to valency parity, both the martensite transformation behavior and the transformation temperature are affected by Al addition, as indicated by lower martensite transformation temperature and two stage transformation, which are indicative of electronic structure modifications due to change in inter-atomic spacing.
13. Addition of B along with Al intended to substitute Ga in NMG, results in formation of a two-phase structure and martensite structure changed to non-modulated tetragonal

- martensite in place of 5M modulated martensite obtained with Al addition alone, possibly because of the small sized boron atoms destroying modulation by its ability to occupy interstitial sites randomly.
14. The range of temperature over which martensite transformation occurs, increases with increased B content in alloys containing both Al and B. A wider martensite transformation temperature range of ~90K for high B alloy shows that in spite of improved martensite stability, the reversibility of transformation is adversely affected by B addition.
 15. The saturation magnetization decreases with B addition significantly more than the dilution effects and possibly, it shows that magnetic exchange for the transition elements is adversely affected.
 16. The rapid solidification of the alloys containing both Al and B resulted in a modulated 7M martensite structure in place of 5M structure observed in the alloy containing Al subjected to heat treatment¹ and the tetragonal martensite structure observed in alloys containing both Al and B subjected to heat treatment². Thus, rapid solidification processing has significant potential to get the desired modulated martensite structure for FMSM behaviour.
 17. For rapidly solidified ribbons of the alloys containing Al or Al and B, the lattice parameters of the martensite phase do not change appreciably with composition indicating a small/no change in composition of the majority phase. The differences in compositions are apparently adjusted in the amorphous/ nano-crystalline phase present in the ribbons.
 18. Martensite transformation temperatures of rapidly solidified ribbons of the alloys containing Al or Al and B, do not change significantly and it may be due to similar compositions of the majority phases in the ribbons.
 19. The magnetization in rapidly solidified ribbons of the alloys containing Al or Al and B, are very low even although there is presence of a modulated martensite structure and it can be attributed a lower or different ordering in the melt spun ribbons as a result of rapid solidification.

20. The rapidly solidified ribbons of the alloys containing Al or Al and B, show a fine martensite plate width of 10-15 μm . These plates have internal twin structure with finer martensite of 3-5 μm width. The orientation relationship within the internal twins and primary twin plates is the same.
21. The rapidly solidified ribbons of high B content show faceted grain morphology instead of spherical grains at lower or zero B content. The changed morphology can be attributed to different composition of the grain boundary area leading to different interfacial energies at higher B levels.
22. Substitution of Sm or Dy for Ga in NMG results in formation of second phase with the retention of rare earth element primarily into the second phase. The amount of second phase increases with increasing rare earth content. The EPMA analysis does not show the presence of the rare earth in matrix phase implying that if present, it is below the detection limit EPMA.
23. The martensite transformation temperatures obtained in alloys containing rare earth elements, increases and the mechanical properties like rate of work hardening, UTS and strain to fracture increases over those observed in NMG, signifying different chemistry of the major phases. It appears that some amount of rare earth below detectable limits of EPMA is present in the matrix phase and responsible for these changes.
24. The range of temperature over which martensite transformation occurs, increases with rare earth additions.
25. The saturation magnetizations are lowered with rare earth additions but the extent of lowering is more than that expected due to atomic dilution and it could be because of a lower magnetization of the second phase.

In context of alloy development for FMSM applications, the requirement is reversible de-twinning of martensite variants at operating temperature induced by magnetic field. Easier de-twinning is normally possible in martensites with modulated structures. Higher Curie temperature and martensite transformation temperature above room temperature and a large magnetization and large strain induced by martensite transformation through the presence of

modulated martensite variants is therefore necessary to get sizable FMSM effect. Our studies indicate that the properties of the alloys can be modified both with quaternary additions and the non equilibrium processing. An addition of Fe alone improves the magnetization with martensite transformation but Curie temperatures decreases or increases at different levels of substitutions. The addition of Co alone increases the Curie temperature while forming the modulated martensite structure. Therefore, an optimal combination of these two elements of Co and Fe together may help in developing a better FMSM alloy. The addition of trivalent Al permits obtaining the modulated martensite structure through inter-martensite transformation and controlled additions of Al would help in controlling the desired structure at different temperatures. The addition of B in equilibrium alloys is detrimental due to break down of super period modulated structure and it should be avoided. However, rapid solidification may restore modulated martensite but the magnetization is very low. Rare earth additions are not resulting in modulated reversible martensite and so, it does not show much potential in the context of FMSM alloy development although these additions improve mechanical properties. While the role of individual additions have been identified during this study in the context of quaternary addition to ternary NMG, a combination of optimal quantities of these elements to more complex alloys may lead to the development improved FMSM alloys for applications.

13. Brown P J, Crangle J, Kanomata T, Matsumoto M., Neumann K-U, Ouladdiaf B and Ziebeck KRA (2002), **The crystal structure and phase transitions of the magnetic shape memory compound Ni₂MnGa**, J. Phys.: Condens. Matter **14**, 10159
14. Buchelnikov VD , Taskaev SV, Zagrebina MA, Zayak AT and Entel P (2008), **The phase diagram of Ni–Mn–Ga alloys with account of crystal lattice modulation and external magnetic field**, Mater Sc and Eng A **481-482**, 218
15. Buehler WJ, Gilfrich JW and Wiley RC (1963), **Effect of Low-Temperature Phase Changes on the Mechanical Properties of Alloys near Composition TiNi**, J Appl Phys **34**, 1475
16. Cai W, Gao L, Liu AL, Sui JH and Gao ZY (2007), **Martensitic transformation and mechanical properties of Ni-Mn-Ga-Y ferromagnetic shape memory alloys**, Scripta Mater, **57**, 659.
17. Cesari E., Font J, Muntasell M., Ochin P., Pons J and Santamarta R (2008), **Thermal stability of high-temperature Ni-Mn-Ga alloys**, Scripta Mater, **58**, 259
18. Chang LC and Read TA (1951), **Plastic deformation and diffusion-less phase changes metals: The gold-cadmium beta phase**, Trans AIME **189**, 47
19. Chen J, Gharghoury MA and Hyatt C V (2004 a)., **The influence of composition and thermomechanical treatments on the magnetic shape memory effect of Ni-Mn-Ga single crystals**, Proceedings SPIE, **5387**, 549
20. Chen J, Gharghoury MA and Hyatt C V (2004 b)., Proceedings SPIE, **5053**, 181
21. Chernenko VA (1999), Scripta Mater **40**, 523
22. Chernenko VA (2007), Presentation at Intl Conf on FMSM alloys, Kolkata, Nov 2007.
23. Chu SY, Gallagher R, D Graef M and McHenry ME (2001), IEEE Mag, **37**, 2666
24. Cong DY, Zhang YD, Wang YD, Humbert M, Zhao X, Watanabe T, Zuo L and Esling C (2007), **Experiment and theoretical prediction of martensitic transformation crystallography in a Ni–Mn–Ga ferromagnetic shape memory alloy**, Acta Mater, **55** 4731
25. Cullity BD (1972), **Introduction to magnetic materials**, Addison-wesley, USA
26. Cullity BD (1978), **Elements of x-ray diffraction**, Addison-wesley, USA
27. Entel P, Bucholnikov VD, Khovailo VV, Zayak AT, Adeagbo WA, Gruner ME, Harper HC, and Wasserman EF (2006), **Modelling the phase diagram of magnetic shape memory Heusler alloys**, J. Phys. D: Appl. Phys., **39**, 865.

28. Eyercioglu O, Kanca E , Pala M and Ozbay E (2008), **Prediction of martensite and austenite start temperatures of the Fe-based shape memory alloys by artificial neural networks**, J Mater Proc Tech ,**200**, 146
29. Foner S, (1956), **Vibrating sample magnetometer**, Rev. Sci. Instr., **27**, 548
30. Foner S, (1959), **Versatile and sensitive vibrating sample magnetometer**, Rev. Sci. Instr., **30**, 548
31. Gao L, Gao ZY, Cai W and Zhao LC (2007), **Effect of rare earth Dy addition on microstructure and martensitic transformation of polycrystalline Ni₅₀Mn₂₉Ga_{21-x}Dy_x ferromagnetic shape memory alloys** Mater Sc & Engg A, **438-440**, 1077
32. Gao L., Sui JH and Cai W (2008) , **Influence of rare earth Gd addition on the structural and magnetic transitions of Ni-Mn-Ga alloys**, J Mag Mag Mater, **320**, 63.
33. Girard C, Bechu S, Caillault N, Carbone L, Ortega L and Fruchart D (2008), **Bulk and thin films of magnetic shape memory Ni–Mn–Ga alloys deposited by multi-dipolar plasma-assisted sputtering**, J Alloys & Compounds, in press, doi:10.1016/j.jallcom.2007.11.087
34. Glavatskyy I, Glavatska N., Soderberg O., Hannula S.-P and Hoffmann J.-U. (2006), , **Transformation temperatures and magnetoplasticity of Ni-Mn-Ga alloyed with Si, In, Co or Fe** , Scripta Mater, **54**, 1891
35. Goldstein JA and Yakowitz H (1975), **Practical scanning electron microscopy**, Plenum publications.
36. Greer AL (1982), Acta Metall, **30**, 171
37. Gupta P, Robi PS, Sinha PP, and Srinivasan A (2004), **Preparation and characterization of Ferro-magnetic Shape Memory Alloys**, J. Mater. Proc. Tech. **153-154** , 965
38. Gutierrez J., Lazpita P, Barandiaran JM, Fdez-Gubieda, J. Chaboy and Kawamura N, (2007) **Annealing influence on the atomic ordering and magnetic moment in a Ni–Mn–Ga alloy**, J Mag Mag Mater **316** , 610
39. Gutiérrez J., Barandiarán JM, Lázpita P, Seguí C and. Cesari E (2006), **Magnetic properties of a rapidly quenched Ni–Mn–Ga shape memory alloy**, Sensors & Actuators A, **29**, 163

40. Gutierrez P, Lazpita J, Barandiaran JM, Garitaonandia JS, Plazaola F, Legarra E, Chernenko VA and Kanamoto T, **Mossbauer study of the martensitic transformation in a Ni-Fe-Ga shape memory alloy**, *Hyperfine Interactions* **168**, 1207 (2006).
41. Heczko O, Prokes K, S-P Hannula(2007), Neutron diffraction studies of magnetic-shape memory Ni–Mn–Ga single crystal , *J Mag Mag Mater*, 316, 3869
42. Heidenreich (1964), **Fundamentals of Transmission Electron Microscopy**, Interscience , New York
43. Jiang C, Muhammad, Deng L, Wu W and Xu H (2004), **52**, 2779
44. Jiles D (1998), **Introduction to magnetism and magnetic materials**, CRC Press
45. Jin X, Marioni M, Bono D, Allen SM and O' Handley R C (2002), **Empirical mapping of Ni–Mn–Ga properties with composition and valence electron concentration**, *J. App Phys*, **91**,8222
46. Kainuma R, Imano Y, Ito W, Morito H, Okamoto S, Kitakami O, Oikawa K, Fujita A, Kanomata T and Ishida K (2006) , **Magnetic-field-induced shape recovery by reverse phase transformation**, *Nature* **439**, 23 Feb 06, 937-960
47. Kakeshita T and Ullako K, (2002), **Giant magnetostriction in ferromagnetic shape-memory alloys** , *MRS Bulletin*, Feb 2002, 105-109
48. Karaca HE , Karaman I , Basaran B , Lagoudas DC, Chumlyakov YI and Maier HJ (2007), **On the stress-assisted magnetic-field-induced phase transformation in Ni₂MnGa ferromagnetic shape memory alloys**, *Acta Mater*, **55**, 4253
49. Khovailo VV, Abe T, Koledov VV, Matsumoto M, Nakamura H, Note R., Ohtsuka M., Shavrov VG, and Takagi T (2003 a), **Influence of Fe and Co on phase transformations in Ni-Mn-Ga alloys**, *Mater. Trans., JIM*, **44**, 2509.
50. Khovailo VV, Oikawa K, Abe T and Tagaki T (2003 b), **Entropy change at the martensitic transformation in ferromagnetic shape memory alloys Ni_{2+x}Mn_{1-x}Ga**, *J. Appl. Phys.*, **93**, 8483
51. Khovailo VV, Oikawa K, Wedel C, Tagaki T, Abe T and Sugiyama K (2004), *J Phys: Condensed Matter* , **83**, 7297
52. Kohl M, Agarwal A, Chernenko Va, Ohtsuka M and Seemann K (2006), **Shape memory effect and magnetostriction in polycrystalline Ni–Mn–Ga thin film microactuators** ,*Mater Sc & Engg A* **438-440**,940
53. Kudryavtsev YV, Lee YP and Rhea JY (2002), **Structural and temperature dependence of the optical and magneto-optical properties of the Heusler Ni₂MnGa alloy**, *Phy Rev B* **66**, 115114

54. Lacheisserie ET, Gignoux D and Schlenker M (2003), **Magnetism:: Fundamentals**, Springer.
55. Lakshmi N, Venugopalan K and Varma J (2002), **Mössbauer studies of hyperfine fields in Fe₂CrAl**, *Pramana-J Phys*, **59**, 531
56. Lanska N, Soöderberg O., Sozinov A, Ge Y, Ullakko K, and Lindroos VK(2004), **Composition and temperature dependence of the crystal structure of Ni-Mn-Ga alloys**, *J. Appl. Phys.*, **95**,8074.
57. Leonowicz M, Wroblewski R, Kaszuwara W, Zengqi Z.and Liping J (2006), **Modification of the properties of Ni-Mn-Ga magnetic shape memory alloys by minor addition of terbium**, *Proceedings of SPIE - The International Society for Optical Engineering*, **6170**, 61702C
58. Li Y, Jiang C, Liang T, Ma Y, and. Xu H (2003), **Martensitic transformation and magnetization of Ni-Fe-Ga ferromagnetic shape memory alloys**, *Scripta Mater*, **48**, 1255
59. Li Y, Xin Y and Jiang C (2004), **Shape memory effect of grain refined Ni₅₄Mn₂₅Ga₂₁ alloy with high transformation temperature**, *Scripta Mater*, **51**,849
60. Liang T, Jiang Cand Xua H (2005), *Mater Sc Eng A*, **402**,5
61. Liebermann H.H.,. Graham Jr C.D., (1977), **Plastic and magnetoplastic deformation of Dy single crystals** , *Acta Metall.* **25**, 715
62. Liu Z.H. , Z.Y. Zhu, S.Y. Yu, H.Z. Luo, J.L. Chen, G.H. Wu(2007), **Anisotropy of the magnetoresistance in ferromagnetic shape memory alloy Ni₅₂Mn_{16.4}Fe₈Ga_{23.6} single crystal**, *J Mag and Mag Mater* **319**, 69
63. Liu C, Gao ZY, An X, Wang HB, Gao LX and Cai W (2008), **Surface characteristics and nanoindentation study of Ni–Mn–Ga ferromagnetic shape memory sputtered thin films** ,*Appl Surface Sc*, **254**,2861
64. Liu G, Chen J, Cui Y, Liu Z, Zhang M, Wu G, Bruck E, de Boer FR, Meng F, Li Y and Qu J (2004), **Characterization of preferential orientation of martensitic variants in a single crystal of NiMnGa**, *Solid State Comm* **130**, 687
65. Majumdar S, Sharma VK, Manekar M, Kaul R , Sokhey KJS, Roy SB and Chaddah P (2005), **Magnetic and martensitic transitions in Ni-Fe-Ga alloy** *Solid State Commun.*, **136**, 85
66. Manosa L ,Planes A, Zarestky J., Lograsso T., Schlagel D. L, and Stassis C (2001), **Phonon softening in Ni-Mn-Ga alloys** , *Phy Rev B*,**64**, 024305

67. Manosa L, Planes A, Acet M, Duman E and Wassermann EF(2004), **Magnetic shape memory in Ni–Mn–Ga and Ni–Mn–Al**, J Mag Mag Mater 272–276, 2090
68. Martynov VV and Kokorin VV, (1992) **The crystal structure of thermally- and stress-induced Martensites in Ni₂MnGa single crystals** , J. Phys. III France 2, 739.
69. Mathur RP, Murthy VN, Akhtar D, Subramanyam P and Jagannathan R (1987), **Crystallization processes in amorphous Fe₇₄Co_{10-x}Cr_xB₁₆ alloys**, J Mater Sc Lett, 6,1019.
70. Matumoto M, , Ebisuya M, Kanomata T, Note R, Yoshida H and Kaneko T (2002), **Magnetic properties of Heusler type Ni_{2+x}Mn_{1-x}Ga**, J Mag and Magc Mater, 239, 521
71. McCormack R and de Fontaine D (1996), **.First-principles study of multiple order-disorder transitions in Cd₂AgAu Heusler alloy**, Phys. Rev. B. 54, 9746
72. Mehaddene T, Neuhaus J, Petry W, Hradil K, Bourges P and Hiess A (2008), **Phonon dispersions of Ni–Mn–Al shape memory alloy**, Mater Sc and Engg A, 481-482, 197
73. Mitros C. Yehia S, Kumar S, Jha S., DeMarco M., Mitchell D.,. Julian G.M, and Dunlap R.A (1987), **Hyperfine magnetic field measurements in Heusler alloys Ni₂MnGa, Pd₂MnSn, and Ru₂FeSn**, Hyperfine Interact.34, 419
74. Moya X., Mañosa LI , Planes A, Krenke T, Acet M, Wassermann EF, Morin M, Garlea VO, Lograsso TA and Zarestky JL (2008), **Lattice dynamics of Ni–Mn–Al Heusler alloys**, Mater Sc and EnggA481-482, 227
75. Murakami Y, Shindo D, Kobayashi K, Oikawa K, Kainuma R and Ishida K (2006), **TEM studies of crystallographic and magnetic microstructures in Ni-based ferromagnetic shape memory alloys**, Mater Sc and Engg:—A 438-440, 1050
76. Murr LE (1970), **Electron optical applications in materials science**, Mc Graw Hill, USA
77. Murray SJ, Farinelli M, Kantner C, Huang JK, Allen SM, and O’Handley RC, J Appl Phys, 1988, vol.83, p.7297-7299
78. Mössbauer RL (1958), Z Naturforsch, 14a,211
79. Mössbauer RL (1958), Z Physik, 151,124
80. O’Handley RC (1998), **Model for strain and magnetization in magnetic shape memory alloys**, J. Appl. Phys., 83, 3263

81. Oikawa K, Wulff L, Izima T, Gejima F, Ohmori T, Fujita A, Fukamichi K, Kainuma R, and. Ishida K (2001), **Promising ferromagnetic Ni-Co-Al shape memory alloys**, Appl. Phys. Lett.,**79**, 3290.
82. Otsuka K and Ren X (2005),**Physical metallurgy of Ti-Ni based shape memory alloys**, Progress in Mat Sc,**50**,511
83. Otsuka K and. Wayman CM (1998), *Shape memory materials*, Cambridge University Press, UK,
84. Overholser RW and Wuttig M (1999), **Chemical ordering in Ni-Mn-Ga Heusler alloys**, Scripta Mater **40**,1095
85. Pace technologies, USA, **Metallographic etchants**, (www.metallographic.com)
86. Panda A.K., Kumar A, Ghosh M and Mitra A (2008), Development of NiMnGa based ferromagnetic shape memory alloy by rapid solidification route, J Mag Mag Mater, doi:10.1016/j.jmmm.2008.04.029
87. Pons J , Cesari E, Seguí C, Masdeu F and Santamarta R (2008), **Ferromagnetic shape memory alloys: Alternatives to Ni–Mn–Ga**, Mater Sc and Eng: A **481-482**, 57.
88. Pons J, Santamarta R, Chernenko VA and Cesari E (2006), **Structure of the layered martensitic phases of Ni-Mn-Ga alloys**, Mater. Sci. Eng., A, **438–440**, 931.
89. Potschke M, Gaitzsch U, Roth S, Rellinghaus B and Schultz L(2007) , **Preparation of melt textured Ni-Mn-Ga** J Mag Mag Mater, **316**, 383
90. Ranjan R, Banik S, Barman SR, Kumar U, Mukhopadhyay PK and Pandey D (2006), **Powder x-ray diffraction study of the thermoelastic martensitic transition in Ni₂Mn_{1.05}Ga_{0.95}**, Phys. Rev. B **74**, 224443
91. Rhyne J.J., Foner S., McNiff E.J, and Doclo R (1968), **Rare Earth Metal Single Crystals. I. High-Field Properties of Dy, Er, Ho, Tb, and Gd**, J. Appl. Phys, **39**, 892.
92. Richard M, Feuchtwanger J, Schlagel D, Lograsso T, Allen SM, O'Handley RC (2006), **Crystal structure and transformation behavior of Ni-Mn-Ga martensites**, Scripta Mater, **54**, 1797
93. Richard M.L, Feuchtwanger J, Allen SM, O'handley RC, Lazpita P and Barandiaran JM (2007), **Martensite transformation in Ni-Mn-Ga ferromagnetic shape-memory alloys**, Met & Mater Trans A, **38**,777.

94. Richard ML, Feuchtwanger J, Allen SM., O'Handley RC, Lazpita P, Barandiaran JM, Gutierrez J., Ouladdiaf B , Mondelli C, Lograsso T, and Schlagel D (2007) , **Chemical order in off-stoichiometric Ni-Mn-Ga ferromagnetic shape-memory alloys studied with neutron diffraction**, Phil Mag, **87**, 3437
95. Righi L, Albertini F.,Pareti L, Paoluzi A. and Calestani G(2007), **Commensurate and incommensurate "5M" modulated crystal structures in Ni-Mn-Ga martensitic phases**, Acta Mater, **55**, 5237
96. Sanchez-Alarcos V, Recarte V, Perez-Landazabal JI and Cuello GJ (2007), **Correlation between atomic order and the characteristics of the structural and magnetic transformations in Ni-Mn-Ga shape memory alloys**, Acta Mater, **55**, 3883.
97. Sanchez-Alarcos V,. Perez-Landazabal JI, . Gomez-Polo C and Recarte V(2008), Influence of the atomic order on the magnetic characteristics of a Ni–Mn–Ga ferromagnetic shape memory alloy, J Mag Mag Mater **320**, e160
98. Schlagel DL, Wu YL, Zhang W, and Lograsso TA(2000)., J. Alloys Compd. **312**, 77.
99. Segui C, Pons J and and Cesari E(2007), **Effect of atomic ordering on the phase transformations in Ni-Mn-Ga shape memory alloys**, Acta Mater **55**, 1649
100. Singh RK, Shamsuddin M, Gopalan R, Mathur RP and Chanrasekaran V, Mater Sc & Eng A, **476**, 195
101. Small KB, Englehart DA and Christman TA (2008), **A guide to etching specialty alloys for microstructural evaluation**, Carpenter, USA (www.carttech.com)
102. Soderberg O (2004), **Novel Ni-Mn-Ga alloys and their magnetic shape memory behaviour**, PhD Thesis, TKK-ME-DT-2, Helsinki University of Technology, Espoo,Finland.
103. Soderberg O, Aaltio A , Ge Y, Heczko O and Hannula S-P(2008), **Ni–Mn–Ga multifunctional compounds**, Mater Sc & Engg A, **481-482**, 80
104. Soderberg O., Ge Y., Sozinov A., Hannula S-P and Lindroos V. K,(2005) , **Recent breakthrough development of the magnetic shape memory effect in Ni–Mn–Ga alloys**, Smart Mater. Struct. **14**, S223
105. Sokhey KJS, Manekar M, Chattopadhyay MK, Kaul R, Roy SB and Chaddah P (2003), **Magnetic and transport properties of ($\beta + \gamma$) $Ni_{35}Co_{35}Al_{30}$ ferromagnetic shape memory alloy across the martensitic transition**, J. Phys. D: Appl. Phys, **36**, 1366.

106. Srivastava VK, Chatterjee R, Nigam AK, and O'Handley RC (2005), **Electric and magnetic signatures of martensitic and intermartensitic transformations in Ni-Mn-Ga crystal**, Solid State Commun **136**, 297
107. Srivastava VK, R Chatterjee and O'Handley RC (2006), **Effect of twin boundaries on electrical transport in a Ni-Mn-Ga single crystal**, Appl Phys Letts, **89**,
108. Stmat K.J., (1988) In Ferromagnetic Materials, vol. 4, E.P. Wohlfarth and K.H.J. Buschow, eds., North Holland, 131.
109. Strnat KJ(1988), In; **Ferromagnetic Materials** , Wohlfarth EP and Buschow KHJ (Eds), , Vol 4 North Holland
110. Tan H. and M.H. Elahinia (2008) , **A nonlinear model for ferromagnetic shape memory alloy actuators**, Communications in Nonlinear Sc and Numerical Simulation **13**, 1917
111. Thomas G (1962), **Transmission Electron Microscopy of Metals**, Wiley, New York
112. Thomas R (1999), **Choosing the right trace element technique**, Today's Chemist at work, **8**,42.
113. Tickle R and James RD (1999), **Magnetic and magnetomechanical properties of Ni₂MnGa**, J Mag Mag Mater **195**, 627
114. Tschiya K, Tsutsumi A, Ohtsuka H and Umemoto M (2004), **Modification of Ni-Mn-Ga ferromagnetic shape memory alloy by addition of rare earth elements**, Mater. Sci. Eng. A **378**, 370
115. Ullakko K., Huang J. K., Kantner C., O'Handley R C and Kokorin V V (1996), **Large magnetic field induced strains in Ni₂MnGa single crystals**, Appl. Phys. Lett. **69**,1966
116. Ullako K, Huang JK, Kokorin VV and O'Handley RC (1997), **Magnetically controlled shape memory effect in Ni₂MnGa intermetallics**, Scripta Met, **36**, 1133
117. Valiullin A.I., Kositsin SV, Kositsina II, Kataeva NV and Zavalishin VA (2006), **Study of ferromagnetic Co-Ni-Al alloys with thermoelastic L1₀ martensite** Mater Sc and Engg A, **438-440**, 1041
118. Wang T (2005),**Inductively coupled plasma optical emission spectroscopy**, : In "Ewings analytical instrumentation handbook", Eds J Cazes and GW Ewing, CRC press.

119. Wang WH, Liu ZH, Zhang J, Cheu JL, Wu GH, Zhan WS, Chin TS, Wen GH and Zhang XX (2002), **Thermoelastic intermartensitic transformation and its internal stress dependency in Ni₅₂Mn₂₄Ga₂₄ single crystals**, Phys Rev B, **66**,052411
120. Webster PJ, Ziebeck KRA, Town SL and Peak MS (1984), Magnetic order and phase transformation in Ni₂MnGa, Phil Mag B, **49**, 295
121. Wertheim GK, (1978), : **Mössbauer Effect : principles and Applications**, Fourth printing, Academic Press
122. Wilson SA, Jourdain RPJ, Zhang Q, Dorey RA, Bowen CR, Willander M, Wahab QU, Willander M, Al-hilli SM, Nur O, Quandt E, Johansson C, Pagounis E, Kohl M, Matovic J, Samel B, Wijngaart W, Jager EWH, Carlsson D, Djinovic Z, Wegener M, Moldovan C, Iosub R, Abad E, Wendlandt M, Rusu C, Persson K (2007),**New Materials for micro-scale sensors and actuators: An engineering review**, Mater Sc & Engg, **R 56**,1
123. Wuttig M, Liu L, Tsichiya K and James RD(2000), **Occurance of ferromagnetic shape memory alloys** , J Applied Physics 87 4707
124. Wuttig M, Li J and Craciunescu C (2001), **A new ferromagnetic shape memory alloy system**, Scr Mater, **44**,2393
125. Xin Y, Li Y, Jiang C and Xu H(2005), **Martensitic Transformations of Ni₅₄Mn₂₅Ga_{21-x}Al_x Shape Memory alloys**, Mater Sc Forum, **475-479** ,1991
126. Xiong F and Liu Y(2007), **Effect of stress-induced martensitic transformation on the crack tip stress-intensity factor in Ni–Mn–Ga shape memory alloy**, Acta Mater, **55**, 5621
127. Xu HB , Li Y, and Jiang CB(2006),**Ni-Mn-Ga high-temperature shape memory alloys** , Mater. Sci. Eng., A, 438–440,1065.
128. Xu HB, Li Y and Jiang CB, Mater Sc & Eng **438-440**, 1065
129. Zayak AT and Entel P (2006), **Role of shuffles and atomic disorder in Ni–Mn–Ga**, Mat Sc & Engg A,**378**,419
130. Zayak AT, Buchelnikov VD and Entel P (2002), **A Ginzburg-Landau theory for Ni-Mn-Ga** , Phase Trans., **75**, 243
131. Zhang PN and Liu J, **Microstructure and mechanical properties in Co–Ni–Ga–Al shape memory alloys with two-phase structure**, J Alloys & Cmpd, in press,